INVESTIGATION ON MULTIPHYSICS CHARACTERISTICS OF SUPERCONDUCTING MAGNETIC ENERGY STORAGE DEVICE

A

Thesis

Submitted to

For the award of

DOCTOR OF PHILOSOPHY (Ph.D)

in

Mechanical Engineering

By

Gaurav Vyas

(41800965)

Supervised By

Dr. Raja Sekhar Dondapati (17715)

LOVELY FACULTY OF TECHNOLOGY AND SCIENCES

LOVELY PROFESSIONAL UNIVERSITY

PUNJAB

2022

DECLERATION

I declare that the thesis entitled **"Investigation on Multiphysics Characteristics of Superconducting Magnetic Energy Storage Device"** has been prepared by me under the guidance of **Dr. Raja Sekhar Dondapati,** Professor, School of Mechanical Engineering, Lovely Professional University, Phagwara, Punjab. No part of this thesis has formed the basis for the award of any degree or fellowship previously.

Gaurav Vyas

Registration No. 41800965

School of Mechanical Engineering

Lovely Professional University

Phagwara, Punjab

Date: 16 June 2022

CERTIFICATE

I certify that **Gaurav Vyas** bearing Registration no. **41800965** has prepared his thesis entitled **"Investigation on Multiphysics Characteristics of Superconducting Magnetic Energy Storage Device"** for the award of PhD degree of Lovely Professional University, under my guidance. He has carried out the work at the School of Mechanical Engineering, Lovely Professional University.

Dr. Raja Sekhar Dondapati (17715)
Professor, School of Mechanical Engineering
Lovely Professional University
Phagwara, Punjab
India

Date: 16 June 2022

ABSTRACT

The present work focuses at investigating the AC Losses in HTS tapes used in the Superconducting Magnetic Energy Storage (SMES) Devices. Further, experimental investigation on structure of SMES is done. Furthermore, thermohydraulic performance of SMES is investigated with different coolants. Computational Fluid Dynamics (CFD) is used to analyze the pressure drop and heat transfer rate for different flow rates to estimate the friction factor, pumping power and cooling capacity with LN_2 flow in SMES. A 3D computational geometry is developed and simulated the flow domain of Supercritical Nitrogen (SCN), Liquid Oxygen (LOX), Liquid Hydrogen (LH2), Liquid Nitrogen (LN_2) in commercial ANSYS. K-epsilon turbulent scheme is used to signify the validity of turbulence model to practical experimental conditions. The simulated results are validated with the results available in literature.

Chapter 1 introduces the high temperature superconductivity, critical parameters of Superconductor, characteristics of Superconductor, various configurations of Superconducting Magnetic Energy Storage (SMES). Further, various types of superconducting tapes used for SMES is also discussed in this chapter.

Chapter 2 begins with the exhaustive survey of available literature on the development of HTS SMES devices and losses encountered by the SMES during normal operation. The implemented cooling strategies to compensate the heat loads due to the losses and the thermohydraulic characteristics in SMES are presented. Further, from the literature, research gaps were identified and research objectives are framed.

Chapter 3 illustrates the computational formulation for solving the AC Losses in SMES employing the governing equations such as Ampere's Law, Faraday's Law and Gauss Law that are required for solving the closure problem. Further, Computational Electro Dynamics (CED) is used for the estimation of AC losses in superconducting tapes used for SMES devices.

Chapter 4 presents the experimental results on different mandrel materials used for SMES devices. Experiments have been performed on different materials with tensile and flexural loading. Stresses generated in the materials at cryogenic temperature were presented when these materials are treated in LN2 for different time intervals.

Chapter 5 describes the thermohydraulic studies in Superconducting Magnetic Energy Storage (SMES) devices. The feasibility of various coolants for the use in SMES devices is investigated. It is found that the cryocoolants along with the addition of nano particles have higher cooling capacity as compared to the any other cryocoolant. Further, the pumping power to circulate the nanoparticle added cryocoolant is found to be higher. Computational Fluid Dynamics (CFD) using Finite Volume method is implemented to investigate the thermohydraulic issues in SMES devices. The results of the investigation are compared with the existing experimental works and found that the results are in agreement with the experimental work.

Chapter 6 deals with the summary and conclusion of present research work along with future scope of the work.

ACKNOWLEDGEMENTS

I express his immense sense of gratitude to **Dr. Raja Sekhar Dondapati**, Professor and Research Coordinator, School of Mechanical Engineering, Lovely Professional University, Phagwara , for his valuable guidance and continuous efforts throughout the tenure of the work . His inspiring support during the course of work, literature review stage, experimental work and publication stage was worth mentioning. His timely help, construction criticism and painstaking efforts made me capable to compile the thesis in its present form.

I extend my gratitude to authorities of Lovely Professional University, Phagwara, for permitting to pursue research work and providing necessary facilities during the experimental and analysis work. I also express my sincere thanks to **Dr. Vijay Kumar Singh**, Head, School of Mechanical Engineering Lovely Professional University, Phagwara, for their cooperation and support. Further, I would like to thank **Dr. Ankur Bahl,** for the continuous appreciation for the publications which I published.

I would like to thank my panel members who provided valuable suggestions during the course and all the staff members of School of Mechanical engineering who have been very patient and co-operative.

I would also like to acknowledge my Co-Scholars **Dr. Mohit Kalisa, Dr. Rajesh Kumar Gadekula, Mr. Rahul Agarwal** and **Mr. Venkata Ramana Uppada**, for providing conducive environment for the research work in the laboratory.

I would like to thank **Lovely Professional University** for giving me opportunity to use their resource and work in such a challenging environment. I am grateful to the individuals whom contributed their valuable time towards my thesis.

It is a matter of great privilege and pride for me to express my sincere thanks, immense gratitude and love to my wife **Mrs. Jyothi Vyas**, who has supported me throughout my thesis with her patience, knowledge, valuable advice, uninterrupted encouragement throughout the tenure of this work along with my twin daughters **Varnika Vyas** and **Vamika Vyas**

I humbly dedicate this work to my father **Mr. Brij Mohan Vyas**, my mother **Mrs. Ranjana Vyas**, who are the source of inspiration and encouragement behind this research work by sacrificing their comforts and always supported me throughout my studies at university. I sincerely acknowledge the help extended by **Vidhi Vyas**, during the tenure of this PhD work and encouragement and best wishes.

Nevertheless, I am highly indebted to almighty God who blessed me with spiritual support and courage at each and every stage of life.

GAURAV VYAS

NOMENCLATURE

$\overline{e}_{ij}$	Steady mean rate of deformation
e'_{ij}	Fluctuation component of rate of deformation
$\overline{T}$	Time averaged temperature (K)
$\overline{u}$, $\overline{v}$, $\overline{w}$	Time averaged components of velocity in x , y , z directions (m/s)
u , v , w	Components of velocity in x , y , z directions (m/s)
u'	Fluctuation in velocity (m/s)
ψ'	Fluctuation in flow property
Φ	Time averaged component of mean flow property
T_{ref}	Reference temperature (K)
k	Thermal Conductivity of LN_2 (W/m-K)
h_c	Convective heat transfer coefficient (W/m^2K)
$\overline{p}$	Average pressure of LN_2 (Pa)

Greek Symbols

ρ	Density of LN_2 (kg/m^3)
κ	Turbulent kinetic energy (m^2/s^2), $\kappa = \overline{u'^2}/2$
ε	Dissipation rate per unit mass (m^2/s^3), $\varepsilon = 2v\overline{e'_{ij}.e'_{ij}}$
μ	viscosity of LN_2 (Pa-s)
φ	Viscous dissipation rate function
σ_k	Turbulent Kinetic Energy (TKE) Prandtl number
σ_ε	Turbulence Dissipation Rate (TDR) Prandtl number
μ_t	Turbulent viscosity (Pa-s), $\mu_t = \rho C_\mu \left(\kappa^2/\varepsilon\right)$

ABBREVATIONS

HTS	High Temperature Superconductor
Tc	Critical Temperature
I_c	Critical Current
J_c	Critical Current Density
H_c	Critical Magnetic Field
LTS	Low Temperature Superconductors
MTS	Medium Temperature Superconductors
PPLP	Poly Propylene Laminated Paper
XLPE	Cross Linked Polyethylene Paper
PVC	Poly Vinyl Chloride
P_C	Critical Pressure
LN_2	Liquid Nitrogen
CSP	Corrugated Steel Pipe
h_c	Convective Heat Transfer Coefficient
CFD	Computational Fluid Dynamics
SMES	Superconducting Magnetic Energy Storage
SFCL	Superconducting Fault Current Limiters
YBCO	Yttrium Barium Copper Oxide
BSCCO	Bismuth Strontium Calcium Copper Oxide
Be	Bejan Number (-)
EGR	Entropy Generation Rate (W/m^3K)
EGV	Entropy Generation Rate due to Velocity Gradients (W/m^3K)
EGT	Entropy Generation Rate due to Thermal Gradients (W/m^3K)
RANS	Reynolds Averaged Navier-Stokes
FVM	Finite Volume Method
TKE	Turbulence kinetic energy
TDR	Turbulence dissipation rate

TABLE OF CONTENTS

LIST OF FIGURES

LIST OF TABLES

Nomenclature

T_C	Critical temperature (K)	h_c	Convective heat transfer coefficient (W/m^2K)
$\bar{e}_{ij}$	Steady mean rate of deformation	$\bar{P}$	Average pressure of LN_2 (Pa)
e'_{ij}	Fluctuation component of rate of deformation	**Greek Symbols**	
$\bar{T}$	Time averaged temperature (K)	ρ	Density of SCN (kg/m^3)
$\bar{u}$, $\bar{v}$, $\bar{w}$	Time averaged components of velocity in x , y , z directions (m/s)	κ	Turbulent kinetic energy (m^2/s^2), $\kappa = \overline{u'^2}/2$
u , v , w	Components of velocity in x , y , z directions (m/s)	ε	Dissipation rate per unit mass (m^2/s^3), $\varepsilon = 2\nu\overline{e'_{ij}.e'_{ij}}$
u'	Fluctuation in velocity (m/s)	μ	Dynamic viscosity of SCN (Pa-s)
ψ'	Fluctuation in flow property	ν	Kinematic viscosity of SCN (m^2/s)
Φ	Time averaged component of mean flow property	φ	Viscous dissipation rate function
T_{ref}	Reference temperature (K)	σ_k	Turbulent Kinetic Energy (TKE) Prandtl number
k	Thermal Conductivity of LN_2 (W/m-K)	σ_ε	Turbulence Dissipation Rate (TDR) Prandtl number
		μ_t	Turbulent viscosity (Pa-s), $\mu_t = \rho C_\mu \left(\kappa^2/\varepsilon\right)$

1 Introduction

In direct electrical energy storage systems, the technology for development of Superconducting magnetic energy storage (SMES) system has attracted the researchers due to its high power density, ultra fast response and high efficiency in energy conversion. Hence, SMES is potentially suitable for short discharge time and high power applications. In the present chapter, a detailed description on construction and working of SMES is presented. Further, different configurations of SMES are addressed depend on the challenges faced during grid integration, comparison with other storage technologies and worldwide projects on SMES are also mentioned. Moreover, the superconducting wires and tapes used for the construction of superconducting magnets are described. In addition, the future application of the SMES in the electrical power grid is explained in detail.

1.1 Introduction to Superconductivity

Superconductivity is the phenomenon where the material/conductor starts expelling the magnetic field. In other words, it is also defined as state of almost zero electrical resistance of the material. This phenomenon can be observed when the material is maintained at extremely low temperature, also called as Cryogenic temperature, by coolants or cryogenic fluids.

Superconductivity is associated with three basic characteristic properties which are critical temperature, critical current and critical magnetic field. Critical Temperature is the temperature till the material exhibits state of superconductivity. Critical current is the maximum current carried by the material maintaining superconductivity.

Materials exhibiting superconductivity expel the magnetic lines of forces. However, when the value of magnetic field is increased beyond a certain limit, the magnetic field starts to penetrate inside the material. This phenomenon is called as pinning and the maximum value of magnetic field expelled by the superconductor is the critical magnetic field.

Superconductors possess an excellent property of handling larger transport current and hence can be useful in electrical industries as larger currents can be transferred with decrease in overall size of the conductor. Several machines have been developed on this physical phenomenon such as Superconducting Motor, Superconducting Transformer, Superconducting cables and Superconducting Magnetic Energy Storage Devices.

1.2 Introduction to Superconducting Magnetic Energy Storage (SMES)

The energy storage market is growing rapidly with the emerging technologies driven by smart grids, utilization of renewable energy, aim to meet carbon emission and electrical driven vehicles. The necessity of conventional power system integration with smart grids are increasing drastically with increase in power demand. However, these smart grids are interconnected with the renewable power generation systems which produces discontinuous power output. Hence, there is a necessity of the system which charges when the excess power is produced and discharges when the power demand increases. Superconducting magnetic energy storage (SMES) is one system, that stores direct electrical energy with high specific power density, infinite discharge and charge cycles and discharges the electrical power within milli seconds with energy conversion efficiency of above 95%. The SMES utilizes three fundamental principles such as zero resistivity of the superconductor corresponds to zero resistive losses, diamagnetism corresponds to magnetic field repulsion and direct energy storage in a magnetic field. These principles provide the potential merits for using the superconducting coil to store the electrical energy efficiently.

The operation of SMES is completely different from the conventional storage technologies because the continuous flow of electrical current in the superconducting coil generates the stored energy. Further, SMES utilizes the direct current (DC). Hence, only one conversion process of alternating current (AC) to DC is required, thereby, the thermodynamic losses in the conversion process are inherent. Initially, the research was carried to develop the large storage SMES for load leveling application in integration with pumped hydroelectric storage. Further, the researchers identified a potential merit of rapid discharge of electrical power. Due to this capability, the technology of SMES is employed in electrical power systems for system stability and pulsate power during voltage sags, power outage, load sensitivity etc. The economic viability is higher for the SMES system in terms of bulk energy storage for smaller systems due to high energy storage and rapid discharge potential. SMES is termed as impulsive source of current than an electrical energy storage system. Hence, it is an alternative for the uninterrupted power supply Flexible AC Transmission Systems (FACTS) and power transmission and distribution systems in electrical power networks as shown in Figure 1-1.

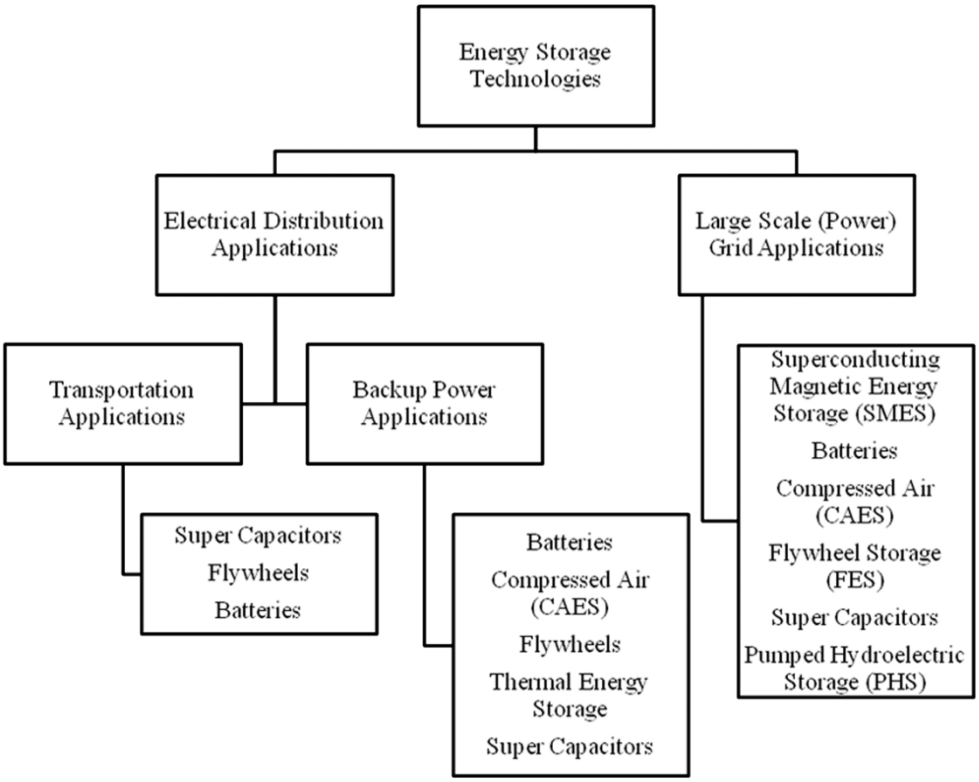

Figure 1-1: Energy storage technologies for distribution and large scale grid applications

1.3 Working of SMES

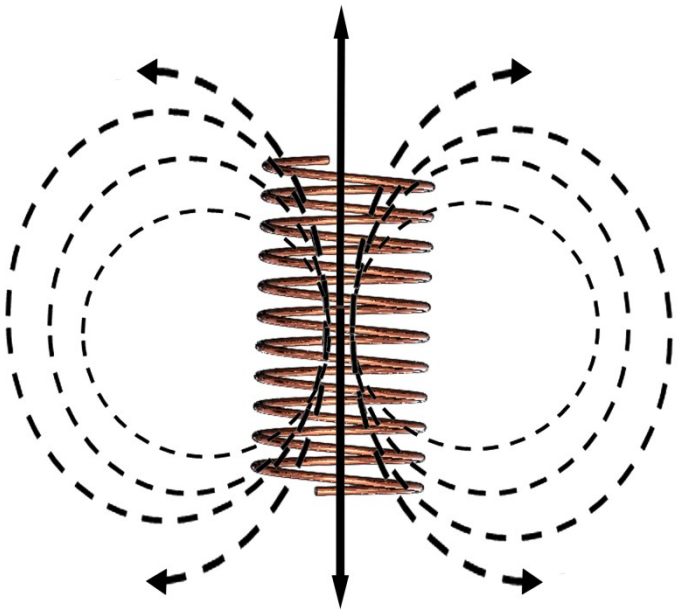

Figure 1-2 : Concept of SMES (short circuited superconducting coil)

A short circuited superconducting coil of SMES system stores the magnetic field due to DC electrical current as shown in Figure 1-2. These system works efficiently, when the temperature of the superconductor used in superconducting coil of SMES is maintained below to the critical temperature (T_c) at the high magnetic fields.

Hence, cryogenic coolants such as Helium and Nitrogen are employed in the operation of SMES to retain the superconductivity of the superconductor. At cryogenic temperatures (approximately 4.5 K), Ohmic losses are not existing in the coil because the electrical resistance offered by the coil is 0Ω (except at joints). Hence, higher efficiency (>95%) can be achieved.

There are four major components in SMES

- **Superconducting coil** made by superconductors such as YBCO, BSCCO, MgB_2 etc. These coils are placed in the vacuum sealed thermally insulated cryogenic environment using a cryostat. It is rested over a mechanical support consists of low thermal conductance. Current leads are used to provide the electrical connections between superconducting coil and room temperature circuit.
- **Cryogenic system** to maintain the temperature of the superconductor below to its critical temperature. These systems are equipped with cryostat, cryocooler, compressors, vacuum pumps etc.
- **Power conditioning system (PCS)** consists of power electronic devices such as capacitors, transistors and inductors, that provide the interface between the superconducting coil (direct current) and the external grid or load (alternating current). The rated power of the SMES is determined by the power capacity of PCS.
- **Control System** continuously monitors the magnetic protection, cryogenics, power electronics etc. with crucial parameters such as cryogenic coolant operation, coil strain, temperature, pressure. It is vital in the SMES because, it establishes a link between the rated power demands from the external load or grid as well as power flow from and to the superconducting coil. The information regarding status of the superconducting coil and dispatch feedback signal from the power grid are received and stored. The response of the SMES depends on the integration between the dispatch feedback and charge level. It provides data to the operator about the SMES system status and maintains the safety. Advanced SMES are integrated with the Internet to access the control and remote observations.

1.4 Technical aspects of SMES

Technical aspects that are to be considered while designing the SMES are

i. Power capacity of SMES

The application in which the SMES is to be installed determines the power capacity of SMES. For instance, applications such as load leveling, stability in the power system and power quality requires different power capacities that depends on either power rating of power conditioning system (PCS) or the maximum power that coil can withstand ($P_{\max} = I_{peak} V_{\max}$).

ii. Physical dimensions of SMES

The volume of the SMES depends on type of the superconducting coil used, type of cryogenic refrigeration system employed for cooling the superconducting coil and the subsystems used in the PCS. The superconducting coil mounted in the vacuum sealed cryostat is smaller in volume compared to refrigeration system and PCS.

iii. Energy storage rating

The energy storage ratings of the SMES depends on the integration of the application and location at which it is installed. It is the product of the discharge time of electrical current to the load and power capacity of the superconducting coil.

iv. Efficiency of SMES

In large scale power applications, the overall efficiency of the SMES is as high as 95%. However, for the small scale application the efficiency is comparatively less than other energy storage systems. In SMES, the electrical energy is stored in the superconducting coils which exhibits absolutely zero losses during the operation. However, other subcomponents are not efficient than superconducting coil due to the losses such as eddy current, hysteresis, conduction, radiation etc. The efficiency of the SMES depends on the energy stored in the superconducting coil. In PCS, few losses are encountered in the electronic subsystem during charging and discharging of the electric current, thereby change in the magnetic field can be noticed. Further, efficiency depends on the overall performance of the cryogenic refrigeration system.

1.5 **Cryogenically cooled superconductor Magnet**

The magnet basic material is its superconductor tape, wound over a mandrel in the form of a coil for solenoid configuration is shown in Figure 1-2 wound over a bobbin structure and lay around a circle for toroidal configuration. There are many types of superconducting wires which are used commercially as shown in Table 1-1. The most common feature of these wires are these can be formed in the size of thin tapes so that the cross section area is

reduced and consequently critical current density of wires can be increased. Various wires/tapes are discussed as follows

1.5.1 *BSCCO-2212 Wires*

BSCC0-2212 has critical temperature (T_c) of around 90K and possesses good qualities between the range 4.2 and 20K. However, this material has low current carrying capacity at 77K (critical temperature of liquid nitrogen) in magnetic field. This was the first material used for High Temperature superconducting wires and can be transformed into round wire, flat plate, rod and even blocks very easily.

1.5.2 *BSCCO-2223*

BSCC0-2223 Wires have their critical temperature almost 20K above BSCC0-2212 i.e. almost equal to 110K. These wires are made from a special technique called as OPIT Method (Oxide Powder in tube) and can be manufactured in multi filamentary composites conductor. The highest average critical current for these wires are 150 A in their self field at 77 K. This is achievable with 4 mm wide tapes. OPIT manufacturing technique is universally accepted in industries and this technique has continuously led to the improvement of tape quality.

1.5.3 *YBCO Wires*

These wires are basically called as second generation wires (2G wires). Manufacturers started producing these wires from thin films of Yittrium Barium Copper Oxide ($YBa_2Cu_3O_7$). The major idea behind development of these wires was that the BSCCO-2223 wires had the maximum critical temperature of 40K while operating in magnetic field above 2T. Hence for development to HTS technology, wires were needed that could sustain higher magnetic fields and maintain higher critical temperatures.

1.5.4 *MgB_2*

In 2001, Akimitsu group of Japan discovered that long ago synthesized Magnesium Diboride (MgB2) possesses superconductivity. After that, Hyper Tech Research USA has been working on the compound to make it high performance commercial superconductor wire. It is made by PIT (powder in tube) technology and many groups have commercially produced it using either MgB2 powder or mixture of Mg and B in powder form. Above 25K there is no current density nor have upper magnetic fields.

Table 1-1: Superconducting materials used in different applications for storing energy in SMES

Superconducting Material	Storage capacity (MJ)	Application	Country	Year	Organization
NbTi	0.27	power system stability	Japan	2008	Tokyo Institute of Technology
	1	UPS		2006	National Nuclear Science Institute
	2.9	power system stability		2006	Kyushu Electric Power Company
	7.34	Voltage drop compensation		2003	Chubu Electrical Power Company
	20	Voltage drop compensation		2004	Chubu Electrical Power Company
	0.2	Power quality	Italy	2008	Bologna University
	2.6	Load sensitivity		2009	Ansaldo Ricerche Spa
	0.3	Voltage drop compensation	China	2007	Tsinghua University
	2	Impulse Power source		2010	Institute Of Electrical Engineering, CAS
	1-5	Commercial application	USA	----	American Superconductor
	30	Low frequency damping		1980	Los Alamos Laboratory
	100	Low frequency damping		2003	University of Florida
	3	UPS	Korea	2006	Korean Electric Research Institute (KERI)
Bi 2212	1	Voltage stability	Japan	2004	Chubu
	0.8	Impulse power source	France	2005	DGA/CNRS
NbTi, Bi 2212 (Hybrid SMES)	6.5	Experimental study	Japan	2006-2007	Toshiba Company
Bi 2223	0.01	smart micro power grid (synchronization control)	China	2009	University of Electronic Science and Technology of China & Innopower Corporation
	0.03	Experimental study		2008	Institute Of Electrical Engineering, CAS
	0.035	Hubei province (Hydropower station)		2007	Huazhong University of Science and Technology
	1	Power quality		2007	CAS
	0.1	Voltage drop compensation	Korea	2006	Changwon National University
	0.6	Voltage and Power stability		2007	KERI
	2.5	Power stability		2010	KERI
	0.15	UPS	Germany	2003	ACCEL Instruments

					Gmbh
	0.0348	UPS	Poland	2009-2010	Superconducting Technology Laboratory
	0.0248	Voltage drop compensation	Australia	2004	Wollongong University
YBCO	2.5	Power quality	Korea	2011	KERI
		DG Networks	USA	2011-2013	Superpower, ABB, BNL, TcSUH
	2400	Load fluctuation compensation	Japan	2010	Chubu and Waseda University

1.6 Superconducting Coils

The superconducting coil is the heart of SMES, design of such coil is crucial because it stores the maximum possible magnetic field that required. For designing the coil efficiently, the factors need to be taken care are minimizing the volume of the superconductor for a desired energy storage considering the mechanical stability and thermal stability with proper cryogenic cooling to ensure the protection from quenching due to electromagnetic forces. Quenching of superconducting coil may degrade the magnetic strength of the superconducting coil. Various applications of SMES are shown in Figure 1-3.

Figure 1-3: Applications of Superconducting Magnetic Energy Storage (SMES) Devices

1.6.1 *Superconducting materials*

The development of superconductors in large scale made a revolutionary changes in superconducting power applications such as Superconducting cables, SMES, superconducting motors, superconducting generators, superconducting transformer and superconducting fault current limiters. The superconductors are premium than normal

conductors because they exhibit zero resistivity and handles higher current density at lower volumes. In SMES, multiple windings of superconductors are in superconducting coil. The superconductors are manufactured either in wire or tape using different superconducting materials. The superconducting wires are manufactured using a thin superconducting material enclosed within Aluminum, Copper, Silver alloy matrix to enhance the strength and to protect the wire from quench. The parameters such as critical magnetic field (B_C), critical current density (J_C) and critical temperature (T_C) characterize the superconducting material.

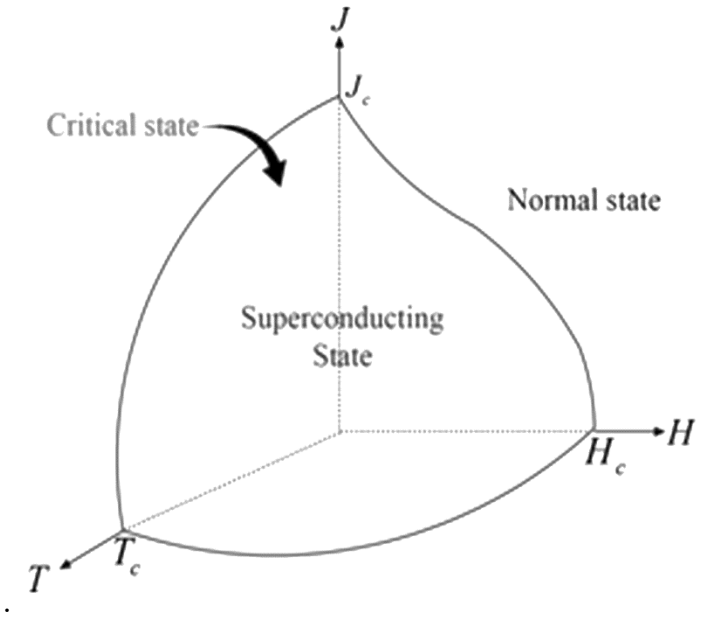

Figure 1-4: J-H-T curve of a superconductor

At cryogenic temperatures, there is a direct dependency within these three parameters to achieve higher magnetic field and higher current densities as shown in Figure 1-4. For instance, for SMES higher magnetic fields are required to achieve higher storage capacities, consequently the critical current density and the critical temperature are changed accordingly. The SMES are operated at the temperature of 4.5 K, even the critical temperatures of different superconductors are higher than 20 K (See Table 1-2). Similarly in HTS cable applications, higher current densities are required. Consequently, the critical magnetic field and the critical temperature are changed accordingly. The HTS SMES are operated at operating range of 65-77K depends on the type of superconducting material used. The cryogenic coolants to be used for cooling the superconductors made up of different materials with respect to critical temperature range are given in Table 1-2.

Table 1-2: Classification of superconductors depends on critical temperatures [1]

Superconducting material	Superconductors (Critical temperature (K))	Cryogenic coolant (Boiling temperature (K) @ 1 atm)	Critical temperature of coolant (K)	Critical Pressure of coolant (K)	Latent heat of vaporization (kJ/kg)
LTS	NbTi (9.8) Nb_3Al (18) Nb_3Sn (18.1)	Helium (4.2)	5.2	2.3	21
		Hydrogen (20.3)	32.9	12.8	445
MTS	MgB_2 (39)	Hydrogen (20.3)	32.9	12.8	445
		Neon (27.1)	44.4	26.5	86
HTS	BSCCO-2212 (85) BSCCO-2223 (110) YBCO (93)	Nitrogen (77.3)	126.3	34	199
		Argon (87.302)	150.69	48.630	163
		Oxygen (90.2)	154.6	50.4	213

Table 1-3: Superconducting materials used at different temperature in SMES projects [2]

Superconducting Materials	Temperature (K)	Energy (MJ)	Country	Organization	Year
NbTi	4.2	0.0188	Germany	Forschungszentrum Karlsruhe	1995
		1	USA	Superconductivity Inc.	1988
		30	USA	Bonneville Power Authority	1982
BSCCO, NbTi	4.2	6.5	Japan	Toshiba	2007
BSCCO	4.2	1	China	Chinese Academy of Science	2008
	20	0.015	Germany	ACCEL Instruments	2003
		0.06	Korea	Seoul National University	2005
		0.0814	France	CNRS	2008
	25	0.005	USA	American Superconductor	1997
	64-77	0.0012	Israel	Bar-Ilan University	2003
BSCCO, YBCO	65-77	0.006	China	China Electric Power Research Institute	2010
YBCO	77	0.002	UK	University of Bath	2014

The superconductors are classified into two categories depends on the behavior of superconductor in the magnetic field at critical temperature and the critical temperature of the superconducting material. Based on the magnetic field, superconductors are either Type I or Type II. In Type I, superconductors acts as a perfect diamagnetic and repels the magnetic field when it maintained below critical temperature and unable to sustain higher magnetic fields. In Type II, superconductors exhibit a mixed state around the critical temperature and can sustain higher magnetic fields without exhibiting the quench behavior.

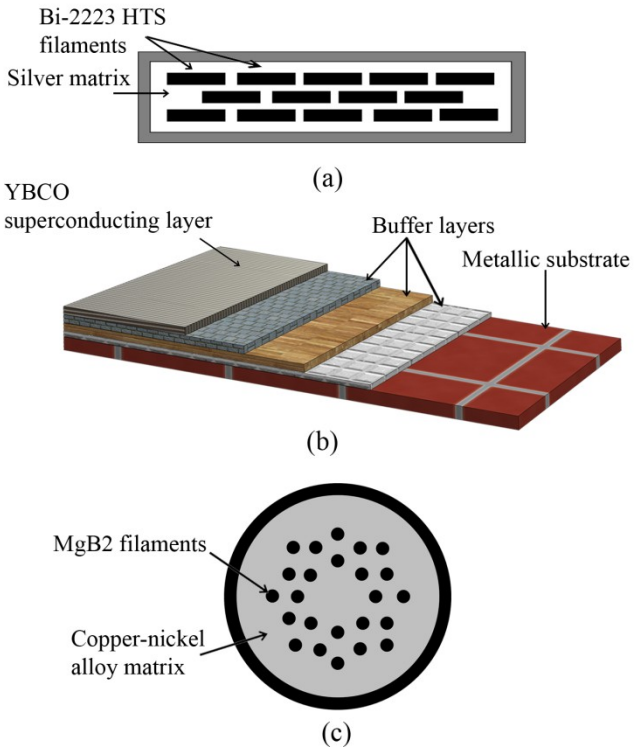

Figure 1-5: Superconductors used in SMES

The superconducting materials used in the SMES project based on the energy stored are shown in Table 1-4. Based on the critical temperatures, superconductors are classified into Low Temperature Superconductors (LTS), Medium Temperature Superconductors (MTS) and High Temperature Superconductors (HTS).

Figure 1-5 shows the superconductors used in storing the energy in SMES. These superconductors are manufactured in the form of wires such as LTS, BSCCO, MgB2 or tapes with multi layers sandwiching the powdered superconductor over deposition layers and buffer layers such as (Re)BCO. The key issue in SMES is selection of the superconductor based on the design and application. The optimal superconducting material should be selected depends on the parameters such as performance, cost, reliability, availability and manufacturing complexity.

Table 1-4: Superconducting materials used to store energy in SMES projects around the world in different applications

Superconducting Material	Energy (MJ)	Application	Country	Organization
NbTi	0.27	Power system stability	Japan	Tokyo Institute of Technology [3]
	1	UPS		National Nuclear Science Institute [4]
	2.9	power system stability		Kyushu Electric Power Company [5]

	7.34	Voltage drop compensation		Chubu Electrical Power Company [6], [7]
	20			
	0.2	Power quality	Italy	Bologna University [8]
	2.6	Load sensitivity		Ansaldo Ricerche Spa [9]
	0.3	Voltage drop compensation	China	Tsinghua University [10]
	2	Impulse Power source		Institute Of Electrical Engineering, CAS [11]
	1-5	Commercial application	USA	American Superconductor [12]
	30	Low frequency damping		Los Alamos Laboratory [13]
	100	Low frequency damping		University of Florida [14]
	3	UPS	Korea	Korean Electric Research Institute (KERI) [15]
Bi 2212	1	Voltage stability	Japan	Chubu [16]
	0.8	Impulse power source	France	DGA/CNRS [17]
NbTi, Bi 2212 (Hybrid SMES)	6.5	Experimental study	Japan	Toshiba Company [18]
Bi 2223	0.01	smart micro power grid (synchronization control)	China	University of Electronic Science and Technology of China & Innopower Corporation [19]
	0.03	Experimental study		Institute Of Electrical Engineering, CAS [20]
	0.035	Hubei province (Hydropower station)		Huazhong University of Science and Technology [21]
	1	Power quality		CAS [22]
	0.01	Voltage drop compensation	Korea	Changwon National University [19]
	0.6	Voltage and Power stability		KERI [23], [24]
	2.5	Power stability		KERI [25]
	0.15	UPS	Germany	ACCEL Instruments Gmbh [26]
	0.0348	UPS	Poland	Superconducting Technology Laboratory [27], [28]
	0.0248	Voltage drop compensation	Australia	Wollongong University [29]
YBCO	2.5	Power quality	Korea	KERI
		DG Networks	USA	Superpower, ABB, BNL, TcSUH
	2400	Load fluctuation compensation	Japan	Chubu and Waseda University [30]

1.7 **Superconducting coil topologies**

In SMES different topologies are designed using various superconducting materials depends on the availability of the superconductor, application and technical attribute of the SMES. In this section design of different SMES topologies such as solenoid, toroidal , four pole, racetrack, shielded and n-polygon topologies are presented.

1.7.1 *Solenoid topology of SMES*

The solenoid topology of SMES is simple in construction. The dimensions of the solenoid SMES depends on the coil dimensions such as diameter, height and winding thickness. Aspect ratio (A_s) is defined as the ratio of winding height of the coil to the diameter of the coil. The energy stored in the solenoid superconducting coil can be calculated using the aspect ratio to the maximum allowable magnetic field through the superconductor (B). Once the superconducting coil dimensions are predetermined based on the application, the design of the mandrel (structural steel) and volume of superconductor required are calculated. The critical current that the superconducting coil can withstand is set according to the mid-plane magnetic field. When the electrical current flows through the superconducting coil, hoop stress is developed that results in the radial Lorentz forces in coil. Figure 1-6 shows the design of solenoid SMES topology.

Figure 1-6 : Solenoid type SMES topology

For a thin solenoid, the volume of the superconductor required is given by [31]

$$Q_{sc} = \frac{C_s\left(A_s\right)E^{0.667}}{B^{0.334}} \tag{1}$$

where, $A_s = \frac{h}{2R}$ is the aspect ratio, s is solenoid, h and R are height and radius of the solenoid.

The energy stored energy per unit volume of the superconductor

$$E_s = \frac{E_{sc}}{Q_{sc}} = \frac{C_s E^{0.334} B^{0.334}}{A_s} \tag{2}$$

1.7.2 *Toroidal topology of SMES*

The toroidal SMES is complex in geometry compared to the solenoid topology. However the energy capacity of the toroidal SMES is higher than the solenoid. The total energy stored in the superconducting windings can be calculated similar to the thick-walled coil because the magnetic field generated due to flow of electrical current is stored in the toroidal windings. In the inner strut of superconducting coil maximum magnetic field will occur.

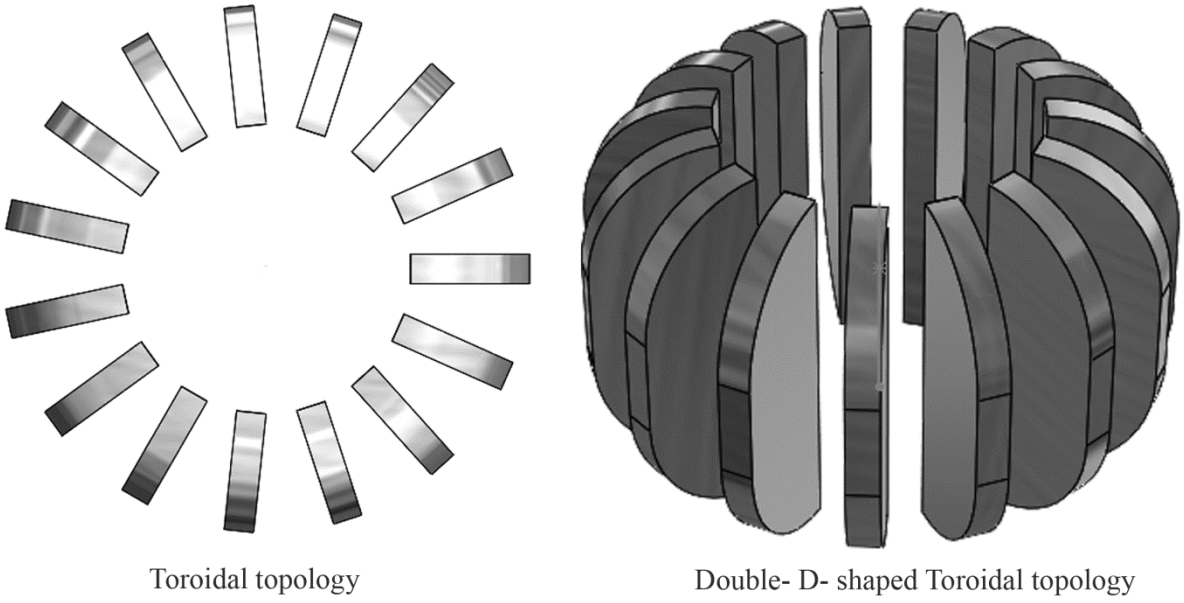

Figure 1-7: Toroidal topology of SMES

Further, the design of torus consists of discrete coils in large sections in order to minimize the magnetic field losses. For large storage capacity, toroidal design requires buckling cylinders additionally to compensate the net inward forces, that result in large Lorentz forces on the windings of the superconducting coil. The thickness of the buckling cylinder used in this topology can be calculated from the hoop stresses that are developed in the cylinder. In toroidal topology, two configurations of SMES are available depends on the application and is shown in Figure 1-7.

The inductance in the toroidal topology is given by [31]

$$L = \mu_0 R\left(1-\left(1-\left(\frac{r}{R}\right)^2\right)^{0.5}\right) \tag{3}$$

where, r is minor radius, R is major radius

Energy stored in the toroidal topology is given by

$$E_{SC} = 0.5\, I_C^2\, \mu_0 R \left(1 - \left(1 - \left(\frac{r}{R} \right)^2 \right)^{0.5} \right) \tag{4}$$

The maximum field in the toroidal topology is given by

$$B_m = \frac{\mu_0 I_C}{2\pi R \left(1 - \left(\frac{r}{R} \right)^2 \right)} \tag{5}$$

Volume of the superconductor required for coil

$$Q_{sc} = 2\pi a l_C^2 = 2\pi r I_C \tag{6}$$

$$Q_{sc} = \frac{2\pi r I_C^{1.334}}{I_C^{0.334}} = \frac{E^{0.667}}{B^{0.334}} \left[\frac{16\pi^2 \left(\frac{r}{R} \right)^3}{\left(\mu_0 \left(1 - \left(\frac{r}{R} \right) \right) \left(1 - \sqrt{1 - \left(\frac{r}{R} \right)^2} \right)^2 \right)^{0.33}} \right] \tag{7}$$

Equation (7) can be rewritten as

$$Q_{sc} = \frac{CP \left(\frac{r}{R} \right) E^{0.667}}{B^{0.334}} \tag{8}$$

The energy stored energy per unit volume of the superconductor

$$E_s = \frac{E_{SC}}{Q_{SC}} \tag{9}$$

Using equation (4) and equation (9)

$$E_s = \left(E_{SC} B \right)^{0.334} \left(\mu_0 \left(1 - \left(\frac{r}{R} \right) \right) \left(1 - \sqrt{1 - \left(\frac{r}{R} \right)^2} \right)^2 16\pi^2 \left(\frac{r}{R} \right)^3 \right)^{0.334} \tag{10}$$

1.7.3 *Shielded topology of SMES*

SMES technology is advancing in small scale power application to compensate the fluctuations in the voltage drop and stabilization of the power line. In such applications, superconducting coil in the SMES encounters AC losses (high pulse losses) within a short span of charging and discharging due to rapid change in the magnetic fields. In order to reduce such losses, a shielded topology of SMES is designed that consists of superconducting coil, shielded parallel with the normal coil, thereby the fluctuating current is shielded and constant electrical current flows through the superconducting coil.

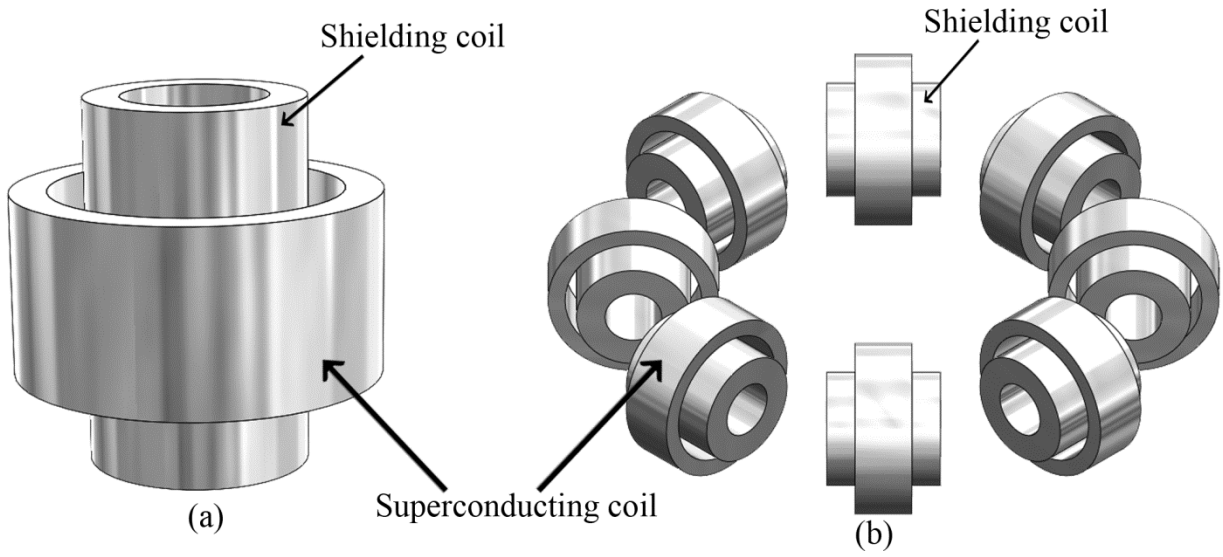

Figure 1-8: Shielded topology of SMES

The shielded type SMES is designed in solenoid and toroidal topologies as shown in Figure 1-8. In solenoid shielded type SMES, the shielding coil in placed in the space provided in the superconducting coil [32]. The field generated by the shielded coil may affect the magnetic field of the superconducting coil. For reducing the influence of the magnetic field, double shielded solenoid type coil with high coaxial winding density is preferable. The advantage with the solenoid shielded SMES is simple in construction of coil construction and cryostat design with refrigeration system. In toroidal shielded type SMES, the magnetic field developed in the superconducting coil are confined [33]. The fields due to fluctuating and stray components are small from the shielded coil on superconducting coil. However, the design of toroidal shielded type SMES is complicated in arranging the shield in torus.

The difference between the shielded topology and other topologies is mutual inductance between the shielded and superconducting magnetic coil because it affect the forces acting

on superconducting coil. The correction in the mutual inductance depends on the electrical current flow in the shielding and superconducting coils.

The self inductance in the shielding coil should be equal to the mutual inductance to satisfy the condition of shielding [32].

$$L_{Sh} = M \tag{11}$$

Maximum energy stored in the system is given by

$$E = \frac{1}{2} L_{SC} I_{SC}^2 + M I_{SC} I_{Sh} + \frac{1}{2} L_{Sh} I_{Sh}^2 \tag{12}$$

where, L_{SC} is self inductance in superconducting coil, L_{Sh} is self inductance in shielding coil and M is mutual inductance of the system.

From equation (12), the energy stored in superconducting coil is given by

$$E_{SC} = \frac{1}{2} L_{SC} I_{SC}^2 \tag{13}$$

In shielding coil, at energy absorption state the change in energy is given by

$$\Delta E = M I_{SC} I_{Sh} + \frac{1}{2} L_{Sh} I_{Sh}^2 \tag{14}$$

Equation (14) can be written as

$$\Delta E = \lambda_{Sh} F_{Sh}^2 \left(\frac{1}{2} + \frac{1}{K} \right) \tag{15}$$

where, $K = \frac{I_{Sh}}{I_{SC}}$, F_{Sh} is electromotive force (EMF) of the shielding coil

The EMF of the superconducting coil is given by

$$F_{SC} = \frac{\lambda_{Sh}}{m K_i} F_{Sh} \tag{16}$$

The amount of superconductor and normal required is given

$$Q_{SC} = 2\pi R_{SC} F_{SC} \tag{17}$$

$$Q_{Sh} = 2\pi R_{Sh} F_{Sh} \tag{18}$$

1.7.4 *Other configurations of basic topologies of SMES*

In general, the solenoid and toroidal topologies are majorly used for energy storage in SMES applications. The major advantage of solenoid is simple in construction and can store higher energy, however the strong drift magnetic fields developed within the SMES causes harmful impact on the environment. Similar fields are observed in the modular toroidal coils, that are designed with equal spacing pancake coil. However, such fields are available within the helical toroid where the superconductor is wound continuously. These are eco-friendly and can store huge amount of magnetic fields.

To utilize the advantage of solenoid and the modular toroid different modifications in the geometries are researched to increase the energy storage capability of the superconducting coil for particular volume of the superconductor. The various topologies of the superconducting coils includes polygon, racetrack and four pole for storing the magnetic fields

1.7.4.1 n-polygon configuration

Based on availability of space, the unidirectional design of solenoids can be modified to form polygons by splitting the single solenoid into multiple solenoids with reduced dimensions that are placed either horizontal or vertical to each other [34], [35] as shown in Figure 1-9. These compact configurations are designed using the same volume of the superconductor required for the unidirectional superconducting coil with relatively lower energy storage loss of approximately 5%.

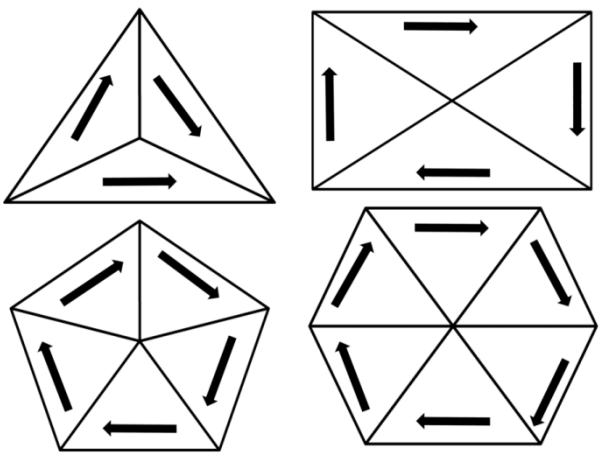

Figure 1-9: n-Polygon configuration of SMES

1.7.4.2 Racetrack coil configuration

The racetrack consists of a pack of 24 modules of racetracks placed one over the other as shown in Figure 1-10. These modules are placed similar to the modules of helical toroid. The advantage with this configuration is that the case walls of the racetrack responds to the various Lorentz loads [36].

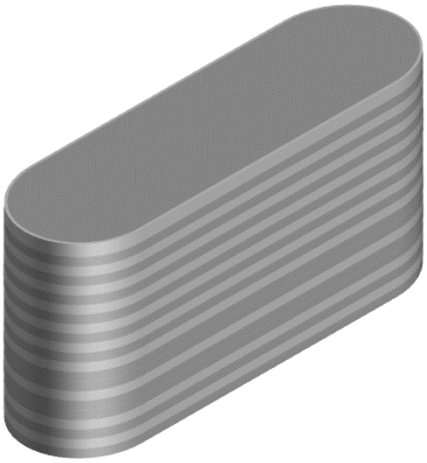

Figure 1-10: Racetrack coil configuration of SMES

1.7.4.3 Four pole configuration

The four pole coils are employed due to compactness, less volume of superconductor required, economical and small stray field compared to the toroidal topology. Two configurations such as flat and long pole are investigated to decrease the stray magnetic field as shown in Figure 1-11. These coils are suitable for high temperature superconductors such as BSCCO and YBCO, medium temperature superconductors (MgB2) [37], [38]. The parameters that influence the magnetic fields are Inner radius of the coil, thickness of the coil, length of the coil, radius of the pole from the orientation center and the operating electrical current.

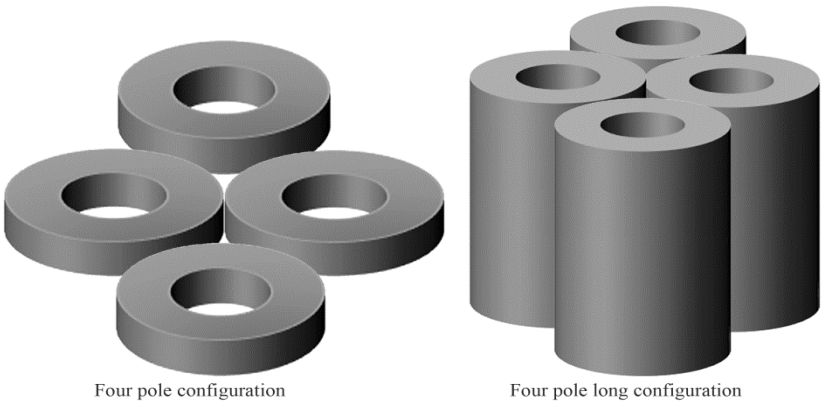

Figure 1-11: Four pole configurations

1.8 **Applications**

SMES proves be useful in industrial and residential sectors as its use will ensure system reliability and safety. Various specific applications of SMES are shown in Figure 1-12.

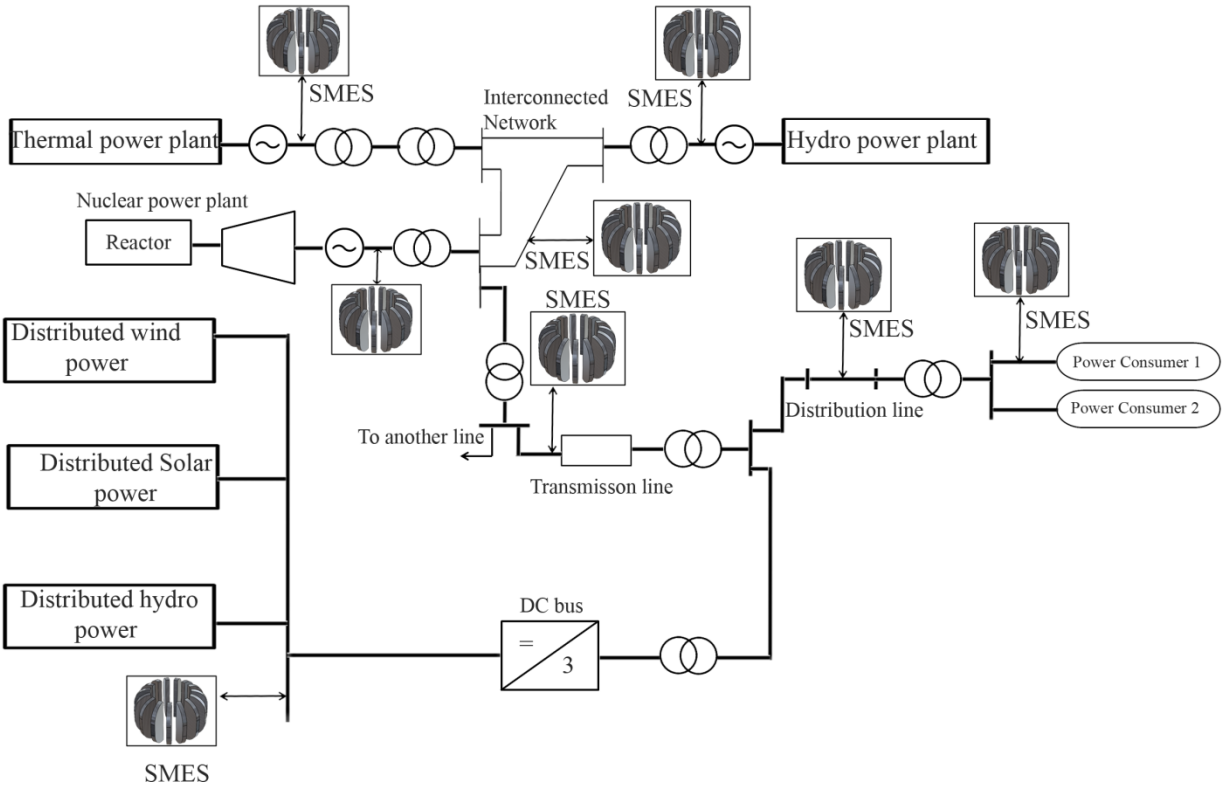

Figure 1-12: Application of SMES

1.8.1 ***System Stability-Damping***

Whenever large load is applied on a power line or when a generator is offline, then power systems may face problems in the form of instabilities across delivery of power. Hence a SMES device installed across the power line can stabilize the line.

1.8.2 ***Load leveling***

Demands for electric power vary randomly across power line. Variations could be seasonal like summers and winters or variations could be across day and night. Industries have different levels of variations, while residential sector shows different variations. Hence SMES device could prove helpful in overcoming the effects of these variation in a controlled environment.

1.8.3 ***Transient Voltage Dip***

Time dependent voltage dips may occur due to abrupt changes in loads that may continue till 10-20 cycles. This dip can be controlled by superconducting magnetic energy storage devices.

1.8.4 *Dynamic Voltage Instability*

Dynamic voltage instability is a condition that can occur when a loss of generation or transmission line and insufficient dynamic reactive power is available to support voltages. As a result, line voltage in all or part of the system will degrade. This process may occur over a period of minutes and result in voltage collapse.

1.8.5 *Spinning Reserve*

SMES also helps in storing the power in reserve kept for the emergency breakdown of a major generator or transmission lines. Its function is to supply immediate power within seconds to keep the system functioning.

2 Literature Review

2.1 Literature review on SMES

Hayashi et al 2006 [5] investigated on reducing the price of the SMES of 2.9 MJ capacity solenoid at an operating current of 9.6 kA. Further, a line with 6 kV distributions was compensated in 16.6 ms in active as well as reactive powers which can be used in practical large scale SMES.

The thermal run away of the SMES was studied by **Seong et al 2007** [39]. It was observed that for the 4-ply conductor the properties such as mechanical and electrical are increased. There are slight changes in the temperature and the thermal run away is at 400A. The temperature also increased due to the eddy losses by radial slitting. At 600kJ the eddy currents are very high for the conductor.

The new model of PSCAD/EMTDC to increase the voltage sag compensation as well as the currents due to the harmonics in the SMES was studied by **Kim et al 2008** [40]. The power supplied is DC and the coils made of both HTS and LTS are connected to the system. It was observed that response time is increased during the charging and discharging of the SMES.

The stability of SMES was measured by varying the temperature, charging and the discharging was measured by **Kim et al 2009** [41]. Further, the accuracy to decrease the eddy losses during transmission, magnetization losses due to current flow and internal energy due to storage during experimentation is measured.

For the WPGS connected to grid with single, double magnets of SMES fir stabilizing the frequency was studied by **Kim et al 2010** [42]. Dual magnet is better than the single magnet SMES during frequency stabilization. In future by varying the magnets critical currents, no turns of the coil and the superconducting wire length the experimentation was to be done.

The scheme for predicting the power oscillations was studied by **Yao et al 2016** [43]. During the connection between the interconnected grids and smart grids are suppressed. To calculate the optimized control an approach of control constrains in SMES was studied.

There are several prominent issues associated with SMES such as design related issues of superconducting coils, cooling up components of SMES, AC losses in superconducting tapes etc. Therefore, the available literature related to Superconducting Magnetic Energy Storage Devices can be divided among those issues. In this section a typical review on the aforementioned issues is presented and efforts are made to find out a technical gap for further research.

2.2 Literature review on Superconducting Coil

Superconducting coil can be developed in various configurations such as Solenoid type coil, Toroidal type coil, Pancake type coil, Double pancake type coil. Sometimes the solenoid configuration is developed by keeping pancake coil one over another axially. In double pancake coil, two pancake coils are connected to each other make one unit or module. Then these units are placed either in a solenoid configuration or in toroidal configuration depending upon the requirements. In this section literature of various design related issues of different types of Superconducting coils will be presented. It can be concluded that these issues proves to be critical in functioning of SMES as shown in Table 2-1.

Table 2-1: Literature review related to Design of superconducting coil of various configurations

Analysis	Author	Study	Coil	Tape Used	Remarks
Numerical	Saichi et al., 2014 [44]	SMES coil design using different tapes and configuration types was done.	Solenoid , Toroidal	MgB_2, Bi-2223, REBCO	• MgB_2 tape with solenoid configuration with flux density less than 5T was optimum for reducing cost of the wire. • Estimation of most suitable max Field density for minimizing length of wire used was also performed.
Numerical	Lee et al., 2012 [45]	Conceptual design of magnet for 5 MJ SMES was presented.	Toroidal	REBCO	• 5MJ SMES requires 141% of CC tapes than 2.5MJ. • Max value of Lorentz force was estimated to be 2.313GN/m^3
Numerical	Park et al., 2008 [46]	Design of Magnets for 5 MJ class	Solenoid	BSSCO, YBCO	• Under same conditions, 2G wires resulted in shorter

		SMES with different tapes are presented and compared.			lengths of wire, lower magnet volume and less number of DPC. • As 2G wires are less thick, current density of 2G wires was higher as compared to 1G wires.
Numerical	Kim et al., 2006 [47]	Design of magnet for 600 KJ SMES was presented.	Double Pancake coils	BSCCO -2223	• Auto Tuning Niching Genetic Algorithm was used to design magnet specifications. • AC losses associated were estimated.
Numerical	Noguchi et al., 2005 [48]	Optimal design method for magnet of 72MJ SMES was proposed	Toroidal	Bi-2223	• Investigations revealed that 16 toroidal coil had the least volume for required energy capacity. • Stray magnetic field associated with it was least.
Numerical	Hayashi et al. , 2001 [49]	Conceptual Design study was done for 1GJ storage capacity SMES	Toroidal	Bi-2223	• Magnet size, volume and stresses for 1 GJ SMES are calculated. • Magnetic field of 10-14 T is optimum to reduce the size, volume and stresses generated
Numerical	Tasaki et al., 2000 [50]	Design of a compact magnet for 3.6MJ SMES was studied	Toroidal	Bi-2223	• Magnetic field of 7-8 T is effective for reducing the magnet volume.
Numerical	Venkatratnam et al, 1999 [51]	Optimum design of a superconducting magnetic coil for a Micro SMES unit was done.	-	-	• The paper showed the difference between normal conductor and superconductor coil to store energy. • The design for normal conductor is controlled by thermal characteristics but for superconductors, it was maximum flux density.

Computational	Qui et al .,2017 [52]	Design of 3 MJ magnet was presented.	Toroidal	Bi-2223	• Using the model, the value of max magnetic field can be estimated which was used to calculate the maximum current and energy stored.
Computational	Zhu et al., 2013 [53]	Design process and cost analysis of Various SMES systems was presented.	Solenoid and Toroidal	YBCO	• Magnets are designed using Global Optimization Technique. • Cost per energy increases with increase in stored energy.
Computational	Kwak et al., 2008 [54]	Design results for 600kJ SMES magnet are proposed.	Double Pancake	BSCCO -2223	• Stress distribution and winding tension in each DPC is described. • Optimal design was also presented.
Numerical , Computational	Ren at al.,2017 [55]	SMES magnets of MJ class are optimized.	Toroidal and Solenoid	YBCO	• For energy capacities less than 1MJ, cost of toroidal SMES was less than solenoid SMES whereas energy capacity more than 30MJ, problem of stress was prominent. • Single solenoid magnet was simple in construction but suffers with field leakage which can be solved by magnetic shielding.
Numerical, Computational	Bae et al., 2009 [56]	Design of 600KJ SMES magnet was performed along with fabrication and electromagnetic analysis	Solenoid	Bi-2223	• Using Genetic Algorithm, HTS magnet for SMES was designed. • Thermal and electromagnetic behavior of magnet was investigated.
Numerical, Computational	Chen et al., 2009 [57]	HTS pancake type and Solenoid type magnets are designed	Pancake type, Solenoid	Bi-2223	• Various parameters such as inductance, magnetic field, critical current, maximum energy are

		and optimized			calculated for pancake and solenoid type magnet. • Computational analysis confirms the numerical results.
Numerical, Computational	Kwak et al., 2009 [58]	Conceptual designs of solenoid and toroidal type magnets for 2.5MJ SMES were presented and compared.	Solenoid, Toroidal	Bi-2223	• Multi grouped Particle Swarm Optimization was used to optimize different magnets. • For 2.5MJ SMES, toroidal type has minimum length of wire and minimized stray field.
Computational , Experimental	Otabe et al., 2009 [59]	Design, fabrication and analysis of Superconducting Magnet for 400J SMES.	Single Pancake	Bi-2223	• Max value of magnetic field at the centre was 0.43T for 50 A of current.

2.3 **Literature review on AC losses in SMES**

Zhao et al., (2017) [60] investigated AC losses for superconducting wire having twists using H formulation in FEM software. In this work, AC losses due to transport current and magnetic field profile was simulated along with the estimation of effect of pitch length on AC losses. It was concluded by the authors that the effect of transverse magnetic field on AC losses is more as compared to effect of longitudinal magnetic field. Also larger the pitch length assumed, larger was the AC losses.

Muzaffer Erdogan (2016) [61] proposed a novel method to estimate propose AC loss for power transmission cables using FEM software Comsol Multiphysics. The cable was assumed to have two layers in which current is equally distributed. Therefore, application of this model where two coaxial cylindrical tubes are there, the AC loss prediction came out to be in good agreement with analytical results by Duoblock model.

Y.D Agassi, (2015) [62] computationally investigated AC losses in superconductor electric field for a slab geometry carrying parallel AC magnetic field. It was reported that the results obtained were in good agreement with BSCCO data and with critical state model

Xu et al., (2015) [63] numerically and computationally investigated the distribution of AC loss for a storage superconducting magnet working on different operating conditions. These conditions are based on commercial Finite Element software as well as on properties of Bi-2223 tape. In this study, using Analytical results, AC loss was estimated which were verified with the computational results obtained.

***Otabe et al., (2013*)** [64] numerically estimated AC losses in superconductor wire with ripple current. It was reported by the authors that the value of AC losses increases with the value of direct current for strip superconductor. It was also recommended that cylindrical hollow structure will be ideal for reduction in AC losses.

Amemiya et al., (2013) [65] numerical electromagnetic field analyses were made for two-layer power transmission cables consisting of coated conductors with spiral geometry. The model for numerical electromagnetic field analyses, considering the spiral geometry of coated conductors in a two-layer cable, was validated successfully by comparing the calculated ac losses with the measured ones. The ac loss in a cable distributes along the cable axis, because the relative positions between inner-layer coated conductors and outer-layer ones vary along the axis. The spiral pitches of layers in a cable influence the current distribution between layers, and, hence, influence the ac loss of the cable. It should be noted that the uniform current distribution would not always minimize ac losses.

Zhao et al., (2011) [66] reported AC loss of HTS pancake coil measured by electrical method maintained at liquid nitrogen temperature. Numerical analysis was performed on Matlab and the theoretical and measured results were compared.

Coombs et al., (2010) [67] focused on computational H formulations to calculate AC loss for real life applications. There are several factors such as quality of mesh, order of element, and thickness of the tape, that affect the AC loss calculations and the time required to solve the computational analysis. Therefore the effect all of these factors was evaluated and an optimal settings of the model was determined that provides fast and accurate results. Computational results proved that AC loss increases with increase in the transport current and the applied magnetic field for single tape carrying current as well as for stack of tapes kept in magnetic field.

Kajikawa et al., (2010) [68] predicted AC loss in superconductor strip with DC and AC along with external AC magnetic field. For both cases, AC loss was in good agreement

with those cases where DC was applied with small amplitude values of external magnetic field.

Park et al.,(2007) [69] computationally designed cooling plates having slits and division all around its periphery so to reduce eddy current loss. These cooling plates are kept at different cross section of SMES.(Bottom, center, Top). Computational results confirmed that AC loss across the plate at the center was 5.97 Watts, across the 4.97 Watts and 3.12 Watts respectively. The total eddy current loss for the SMES was 103.3 Watts which is a considerably higher amount of energy loss.

Tasaki et al., (2001) [49] numerically estimated volumes, flux flow losses and AC losses for magnets of various shapes and confirmed that for 15kWh SMES system, the value of magnetic field should be more than 10T. Also the AC loss associated with the 15kWh SMES magnet range up to 3 Watts.

2.4 Literature review on Novel cooling of SMES with nano cryogenic coolants

The recent advancements in the field of nanotechnology is raised rapidly and attained a great attention after the development of nano fluids. The importance of the nano fluids is to increase the effective thermal conductivity by dispersion of nanometer-size particles in base fluids. Basically chemically stable metals such as Copper (Cu) , Silver (Ag), Gold (Au) etc, metal oxides such as CuO, Al_2O_3, TiO_2, Alumina etc and allotropes of Carbon such as Carbon nano tubes (Single and Multi-walled), Diamond and fullerenes are used to enhance the effective thermal conductivity of the base fluid such as Water, oils, cryogenic coolants and ethylene glycol. Numerous studies based on experimental, analytical and numerical studies are done to predict the thermodynamic and hydrodynamic behavior of nano fluids in various engineering applications.

2.4.1 *Nano fluids in Engineering systems*

From the literature, it was observed that the addition of nanoparticles increases the heat transfer rate in the engineering systems. The nanoparticles are prepared using different methods such as one-step method, two-step method. One-step method of nano-fluid indicates the simultaneous preparation of nanoparticle to the nano size and dispersion of nanoparticles in the base fluid. These method having advantages of reduced agglomeration and uniform dispersion of nano particles. The disadvantage with the method is synthesis of nano-fluid in large scale, high cost for preparation, availability of residual reactants in the nano-fluids. Two-step method is more extensively used for preparation of nano-fluid due

to the commercial advantage of large scale production. The nanoparticles are first prepared as a dry powder using physical and chemical methods. Later, these particles are suspended in to the base fluid utilizing ultrasonic agitation, magnetic force agitation, homogenization, high shear mixing and ball mixing. The disadvantage of this method is tendency of aggregate formation and can be minimized by using surfactants. Hence, different advanced techniques are developed for preparation of nano fluids including one-step method.

2.4.2 *Thermohydraulic characteristics of nano fluids*

The investigation of thermohydraulic characteristics is crucial to predict the performance of a designed system and to evaluate the better operating parameters. Different authors investigated on the thermal characteristics to predict the Nusselt number, heat transfer coefficient, heat transfer rate and cooling capacities in various engineering systems numerically, experimentally and computationally. Further, the hydraulic characteristics such as friction factor, pressure drop an pumping power for different nano particles including carbon nano tubes are investigated.

2.5 Feasibility of nano cryogenic fluids

The analytical feasibility studies on dispersion of nano particles in the **liquid oxygen** (LO_x) as a novel cooling approach for cooling the SMES was presented [70]. **Titanium Oxide** (TiO_2) nano particles with volume fraction of 1-5% are dispersed in the LO_x at the operating temperature of 55-110 K and at a pressure of 50 bar. The effective thermophysical properties of LO_x are enhanced with the dispersion of nano particles compared to LO_x at same operating conditions.

The feasibility studies on dispersion of nanoparticles in the **liquid nitrogen** (LN_2) as a novel cooling approach for cooling the HTS cables was presented analytically [71]. **Copper Oxide** (CuO) nanoparticles with volume fraction of 1-5% are dispersed in the LN_2 at the operating temperature of 65-75 K and at a pressure of 33.9 bar. The effective thermophysical properties of LN_2 are enhanced with the dispersion of nano particles compared to LN_2 at same operating conditions.

The analytical analysis on the feasibility of dispersion of nanoparticles with different diameters in the **liquid nitrogen** (LN_2) for cooling the HTS cables was presented [72]. The nanoparticles considered in the analysis are **CuO, Al_2O_3 and Fe_2O_3** with volume fraction of 1-5%. The nanoparticle diameters considered are 13nm, 27nm, 29nm, 36nm, 47nm, spherical and cylindrical. The nanoparticles are dispersed in the LN_2 at the operating

temperature of 65-75 K and at a pressure of 33.9 bar. The effective thermophysical properties of LN_2 are enhanced with the dispersion of nanoparticles compared to LN_2 at same operating conditions. Further, Fe_2O_3 nanoparticle with a diameter of 13nm at a volume concentration of 5% shows the better results than other nanoparticles.

The nanoparticle such as **Al_2O_3, TiO_2, SiO_2, SiC and CuO** are dispersed in the **liquid oxygen** (LO_x) to predict the thermophysical characterization analytically at cryogenic temperature [73]. The nanoparticles are dispersed with volume fraction of 1-5% in the LO_x at the operating temperature of 55-90 K and at a pressure of 2 bar. With the increase in temperature viscosity, density and thermal conductivity decreases while specific heat increases. Further, with the increase in the volume concentration the opposite tend with respect to temperature was observed.

3 AC losses in Superconducting Magnetic Energy Storage Devices (SMES)

It is a common belief that superconductors conduct electricity with no energy loss. In fact superconductors experience losses when transmitting an alternating current. Loss less transmission occurs for direct current transmission, but most of the power applications involve AC current and DC transmission requires costly converters at ends of transmission line so, most of the transmission lines are of AC.

3.1 AC losses calculations in HTS tapes for SMES applications

A high temperature superconducting power cable can transmit electric power with low loss when compared to conventional power cables. The most important aspect of an economical performance of the High Tc power cable is the refrigeration cost which depends on the AC losses. AC losses are classified as Hysteresis (Self and External field), Eddy current and Coupling losses.

The AC losses in the HTS tapes are given by following equations.

$$AC\,losses = W_{self} + W_{Ba} + W_{Bc} \tag{19}$$

Where, W_{self} = self field loss, W_{Ba} = axial field loss,

W_{Bc} = circumferential field loss

According to the Sumitomo's cable

$$W_{total} = W_{self} + W_B \,(\mathrm{W/m}) \tag{20}$$

Where, W_B is equal to summation W_{Ba} & W_{Bc}.

According to Furukawa's cable

$$W_{total} = W_B + W_{self} + W_{eddy} \,(\mathrm{W/m}) \tag{21}$$

Self field AC losses are calculated by using Norris Equation .

$$Qac = \frac{\mu_0 I_c^2 f}{\pi}\left[(1-\Gamma)\ln(1-\Gamma) + \Gamma - \frac{\Gamma^2}{2}\right] \mathrm{W/m} \tag{22}$$

$$\Gamma = \frac{I_{pk}}{I_c} \quad \text{For } \Gamma << 1 \tag{23}$$

$$Qac \cong \frac{\mu_0 I_c^2 f}{6\pi} \Gamma^3 \tag{24}$$

$$F_R = F_{field} . F_{strain} \tag{25}$$

$$I_{c,cable} = N . F_R . I_{c,tape} \tag{26}$$

$$I_{pk} = \sqrt{2} . I_{rms} \tag{27}$$

$$\Gamma = \frac{\sqrt{2} . I_{rms}}{I_{c,cable}} \tag{28}$$

$$P = V_{rms} \cdot I_{rms} \cdot \cos\phi \tag{29}$$

Where, Γ is the normalized current, F_R is retention fraction, N is the number of tapes in the cable, V_{rms} = RMS voltage (V),

I_{rms} = Transport current (A), cosΦ = power factor.

Hysteresis losses are calculated by using power law of cryo conductor.

$$\rho = kJ^n \tag{30}$$

Where, J= current density.

Dresner found that,

$$Q = G(n,\beta).b^{-1}(v.\mu_0 / J_c)^{(n+1)(n+2)} . E_c^{1/(n+2)} (J_p.b)^k \tag{31}$$

Where, $\beta = J_p / J_c$

$k = (3n+4)/(n+2)$, b=tape thickness, v=frequency, μ_0= magnetic permeability of free space=$4\pi * 10^{-7}$ H/m, E_c= criteria for critical current, E_c can be 1μv/cm or any other reasonable value

If β<1,

$$G(n,\beta) = \frac{1}{6} + 0.17n^{-0.427} \quad (32)$$

Here, Q α J_p to the (3n+4)/ (n+2)-power

If β>>1,

$$G(n,\beta) = D(n).\beta^{n(n+1)/(n+2)}.(E_c / [v\mu_0 J_c b^2])^{(n+1)/(n+2)} \quad (33)$$

Where,

$D(n) = \Pi^{-0.5}\tau[(n+3)/2]/\tau[(n+4)/2]$, τ is the gamma function, Q α J_p to the (n+2)-power.

Hysteresis Power Losses

i) For incomplete penetration limit

$$P_{cable} = 2\pi Db.4^{k-1}[\cos^{2k}\theta + (|\sin^2\theta - \cos^2\theta|/2)^k + 2^{-k}].Q \quad (34)$$

Where, D=diameter of cable

ii) For complete penetration

Power loss along the length of the cable

$$P_{cable} = L\pi DbQ \quad (35)$$

Where, L= number of layer

Surface area

Outer layer=2Nab, for incomplete penetration

Surface area= LNab, for full penetration

Where, N is number of tapes per layer, 'a' is width of the tape.

AC loss rate of 1-3 W/m at 1kA rms

$$P_{cable}\alpha I_C{}^{\alpha}.(I_p / I_c)^k \quad (36)$$

Where, α= (2n+3)/ (n+2)

Coupling losses occurs when two parallel superconducting wires in SMES.

$$B_i = B - \tau B^{\bullet} \quad (37)$$

$$\tau = \frac{\mu_0}{2\rho_t}(\frac{l_p}{2\pi})^2 \quad (38)$$

For round wire,

$$\frac{Q}{V} = \frac{B^2{}_{\max}}{\mu_0} * \frac{2\pi\omega\tau}{1+\omega^2\tau^2} \quad (39)$$

For flat wire,

$$\frac{Q}{V} = \frac{B^2{}_{\max}}{\mu_0} * \frac{\chi_0\pi\omega\tau}{1+\omega^2\tau^2} \quad (40)$$

Where, $\tau = \tau_{round}\frac{\chi_0}{2} * A$

Magnetization in SMES causes AC losses and is calculated by [6].

In MgB_2Superconducting cable 19 untwisted and 19 twisted filaments of MgB_2 with magnetic field perpendicular to the wire axis at various frequencies are considered.

$$T_p = T_c[1-(\frac{H_{AC}}{J_C d})] \quad (41)$$

Where, T_c=critical transition temperature, H_{AC}= AC applied magnetic field amplitude, d= sample thickness.

$$Q = \mu_0 \frac{2}{3}\frac{H_{AC}{}^3}{H_p} \text{ (J/m}^3\text{/cycle), } H_{AC} << H_P \quad (42)$$

$$Q = 2\mu_0 H_p H_{AC} - \frac{4}{3}\mu_0 H_p{}^2, \; H_{AC} >> H_P \quad (43)$$

Where, $H_p = \mu_0 J_c d/2$, for full penetration, J_C is critical current density

$$J_c(B) = J_{co}\frac{1-(B/B_1)}{(1+B)^\beta} \quad (44)$$

Where, J_{co} is zero field critical density, β is exponent of field dependence, B_1 is field in which transport current drops to zero

The electrical shielding is not present in this cable. So, at the former of cable and inner covering of the calorimeter, the magnetic fields, the axial field B_a, the circumferential field B_c causes eddy current losses

AC losses are dependent on the shape of the conductor. For tapes, the loss per AC cycle per unit length due to self field is predicted by Norris equations. For elliptical and thin strip cross sections, but multi filamentary tapes usually well fit the Norris ellipse equation.

The Norris equations are expressed as:

For an ellipse:

$$Qac = \frac{\mu_0 I_c^2 f}{\pi}[(1-\Gamma)\ln\ln(1-\Gamma)+\Gamma-\frac{\Gamma^2}{2}] \text{ W/m} \qquad (45)$$

For thin strips:

$$Qac = \frac{\mu_0 I_c^2 f}{\pi}\left[(1+\Gamma)\ln\ln(1+\Gamma)+(1-\Gamma)\ln\ln(1-\Gamma)-\Gamma^2\right] \text{W/m} \qquad (46)$$

Γ is the normalized current of the tape and described as the ratio of the peak AC current to the critical current.

$$\Gamma = \frac{I_{pk}}{I_c} \qquad (47)$$

$$Qac = \frac{\mu_0 I_c^2 f}{6\pi}\Gamma^3 \text{ W/m for } \Gamma < 1 \qquad (48)$$

Where μ_0 is the permeability of the free space, I_{pk} is the peak current, I_c is the critical current and f is the AC frequency.

Correlating tape properties to cable properties is most important to find AC losses in the High temperature superconducting power cable. The HTS cable will always have lower current carrying capacity than summation of the I_c values of all tapes from which the cable is constructed.

There are two major reasons for this the degradation of the current carrying capacity J_c. Firstly; the self magnetic field is different from an isolated tape, thereby lowering the tape J_c, to perhaps 75% of its original J_c.

3.2 Computational Electro Dynamics (CED) approach

The Cross sectional geometry of HTS tape on which the analysis on AC losses has been done is shown in Figure 3-1. Superconducting Magnetic Energy Storage (SMES) shown in Figure 3-2 contains a mandrel made up of Polytetrafluoroethylene (PTFE) on which HTS tapes are wound. This assembly inserted in to a cryostat with vacuum in the outer chamber and insulated with Multi-layer Insulation (MLI) to avoid radiation heat transfer. Finally a plate made with SS316 LN having vacuum port, current leads port and Liquid Nitrogen (LN2) port is used on the top of the cryostat for closure.

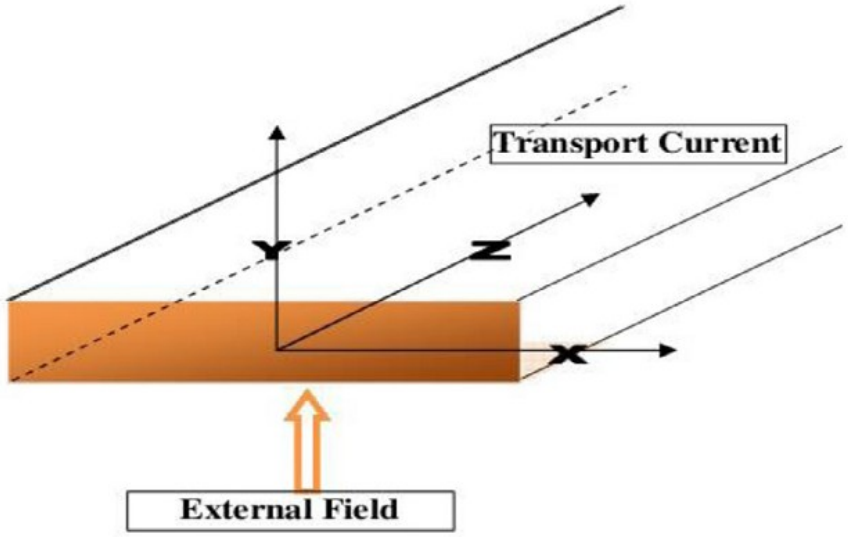

Figure 3-1 Cross-section of the HTS tape with boundary conditions as transport current in z-direction and applied magnetic field in y-direction.

Computational Electrodynamics (CED) employs Finite Difference Time Domain (FDTD) method to discretize the governing equations using finite difference method [74]. Recently, Finite Element Method (FEM) [75][67][76] is mostly used to solve the governing partial differential equations as the accuracy in dealing with irregular geometries is found to be high. Developing a computational geometry of HTS tape with a width (4 *mm*) and thickness (0.4 *mm*) in a Finite Element package is the first step involved in the solution methodology. The next step would be applying the conservation laws such as Ampere's law and Faraday's law on the computational domain (HTS Tape). With proper boundary conditions imposed on the HTS tape, one can evaluate the dependent variables. However,

the difference between modeling of conventional conductors and superconductors is taken into consideration while defining the constitutive relations. Motivated by the importance of estimating AC losses before establishing cooling strategies, the present work aims at determination of these AC losses using Computational Electro Dynamics (CED). The governing equations (conservation laws) along with constitutive relations with applied boundary conditions are solved simultaneously in Finite Element (FE) package COMSOL 3.5. The effect of transport current and external magnetic field on the magnetic flux density and electric field is presented in this section.

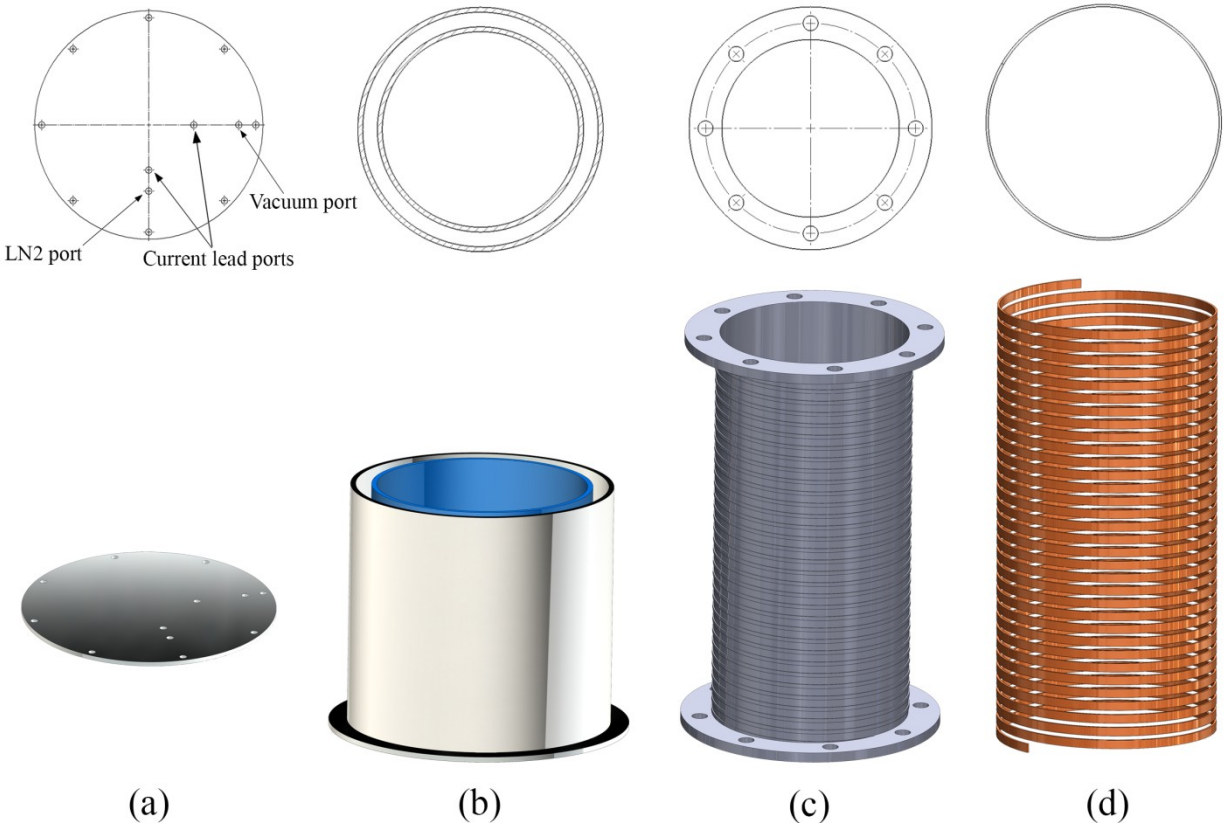

Figure 3-2: (a) Plate made up of SS316 LN (b) SMES Cryostat (c) Mandrel made up of PTFE (d) helically wound HTS tape

The time dependent Maxwell's equations can be written as [74]:

Faraday's Law:

$$-\frac{\partial \vec{B}}{\partial t} = -\nabla \times \vec{E} \quad \vec{M} \tag{49}$$

Ampere's Law:

$$-\frac{\partial \vec{D}}{\partial t} = -\nabla \times \vec{H} - \vec{J} \tag{50}$$

Gauss Law for Electric Field:

$\nabla \bullet$ (51)

Gauss Law for Magnetic Field:

$\nabla \bullet$ (52)

where $\vec{B}$ is the magnetic flux density (T), $\vec{E}$ is electric field (V/m) $\vec{M}$ is magnetic current density (V/m^2), $\vec{D}$ is Electric Flux Density (C/m^2), $\vec{H}$ is magnetic field (A/m) and $\vec{J}$ is Electric current density (A/m^2)

Constitutive relations are necessary to define the properties of materials and their response to electric and/or magnetic fields under consideration.

Considering HTS tape as isotropic, we can write [74]:

$\vec{D} = \varepsilon \vec{E} = \varepsilon_r \varepsilon_0 \vec{E}$ (53)

$\vec{B} = \mu \vec{H} = \mu_r \mu_0 \vec{H}$ (54)

Now, in the superconductor, the electric field and magnetic field can interact with heat as:

$\vec{J} = \vec{J}_{source} + \sigma \vec{E}$ (55)

$\vec{M} = \vec{M}_{source} + \sigma' \vec{H}$ (56)

where σ and σ' are electrical conductivity (S/m) and magnetic losses (ohm/m) of superconductor respectively. However, σ is of the superconductor is not linear and governed by *E-J* characteristics represented with power law as given by:

$$E = E_0 \left(\frac{J}{J_c} \right)^n \quad (57)$$

where E_0 is assumed to be equal to 1x10^{-4} V/m. Hence, under no sources in *J,* one can evaluate σ using equation(55).

Now, for two dimensional geometry of the tape (considering the tape length along *z*-direction as infinite), as in the present problem, the governing equations can be written by combining equations (49), (54)and (57) as:

$$\partial\left(\frac{E_0\left(\frac{\partial H_y}{\partial x}-\frac{\partial H_x}{\partial y}\right)^n}{J_c}\right)\Big/\partial x=-\mu_0\mu_r\frac{\partial H_x}{\partial t} \tag{58}$$

$$-\partial\left(\frac{E_0\left(\frac{\partial H_y}{\partial x}-\frac{\partial H_x}{\partial y}\right)^n}{J_c}\right)\Big/\partial y=-\mu_0\mu_r\frac{\partial H_y}{\partial t} \tag{59}$$

The influence of magnetic field created by adjacent tapes during current transport is assumed as external field and can be estimated by imposing the Dirichlet condition on the boundaries of the HTS tape. However, in the present problem, external field is considered to be perpendicular to the plane of paper. Hence, we have:

$$\left.\begin{array}{l} H_x=0 \\ and \\ H_y=f(t) \end{array}\right\} \tag{60}$$

The transport current assumed to flow in *z*-direction only. Coupling currents in the HTS tape are neglected. As the conductivity of the superconductor is much higher than that of air, the distribution of electric and magnetic fields in the tape is investigated.

The AC loss in the HTS tape can be found using the surface integral on the total computational domain as [77]:

$$\text{AC Loss (P)} = \bigcirc \tag{61}$$

3.3 **Results and Discussion**

In the present work, effect of transport current and external magnetic field on the magnetic flux density and electric field is presented.

3.3.1 *Effect of Transport Current on Electric field and Magnetic Flux density*

While investigating the effect of transport current density on the magnetic field and electric field distribution in the tape, we have imposed magnetic insulation boundary conditions on the surface of the tape signifying that there is no external magnetic field. The results obtained at various transport current densities are shown in Figure 3-3 and Figure 3-4. It can be observed from Figure 3-3 that at transport current densities beyond 4x107 A/m2, there is marginal variation in the y-component of magnetic flux density. However, the same is not true with electric field distribution as can be seen from Figure 3-4. The contours of z-component of electric field and y-component of magnetic flux density at a

current density of 2x107 A/m2 is shown in Figure 3-5. It can be observed that the direction of electric field is reversed near the edges on the HTS tape.

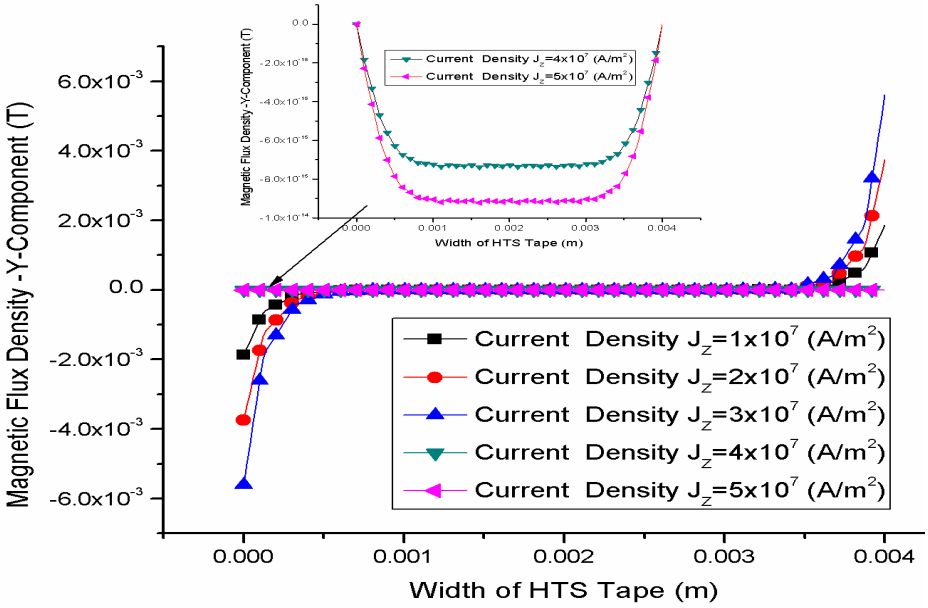

Figure 3-3: Variation of Y-Component of Magnetic Flux Density with Current Density at no external magnetic field

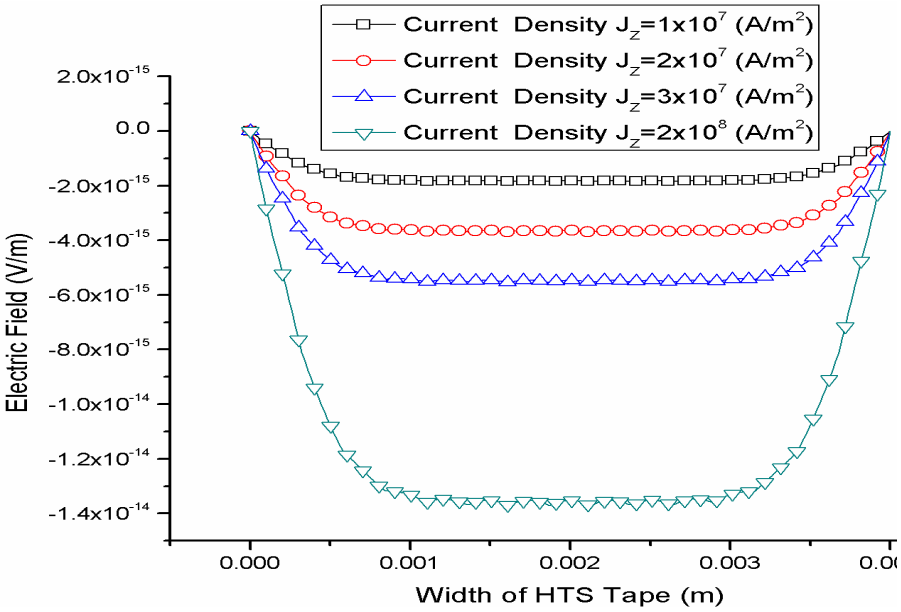

Figure 3-4: Variation of Z-Component of Electric field with current density at no external magnetic field

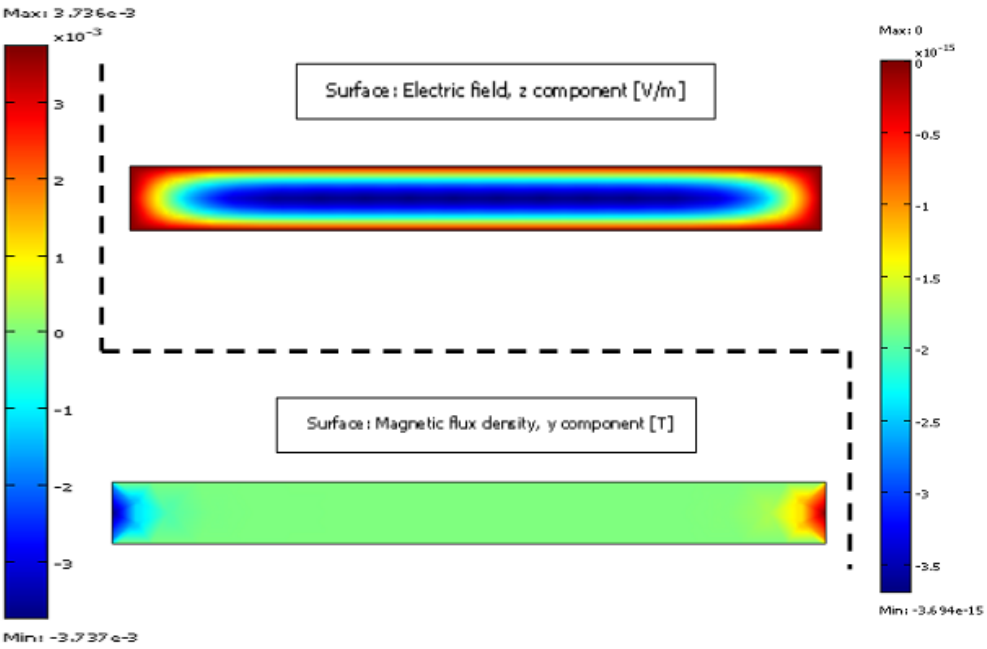

Figure 3-5: Magnetic flux and Electric field distribution contours in the HTS Tape at no external magnetic field and at a current density of 2x10^7 *A/m^2*

3.3.2 *Effect of External Field on Electric field and Magnetic Flux density*

The present analysis is further extended to investigate the effect of applied field on the electric and magnetic flux density. The results obtained by applying an external field of 2500 *A/m* to 8500 *A/m* at a constant current density of 2x10^7 *A/m^2* are presented in Figure 3-6 and Figure 3-7. The Y-Component of magnetic flux density varies considerably with applied external field as shown in Figure 3-6. However, the spatial variation of magnetic flux density along the width of the tape is not observed.

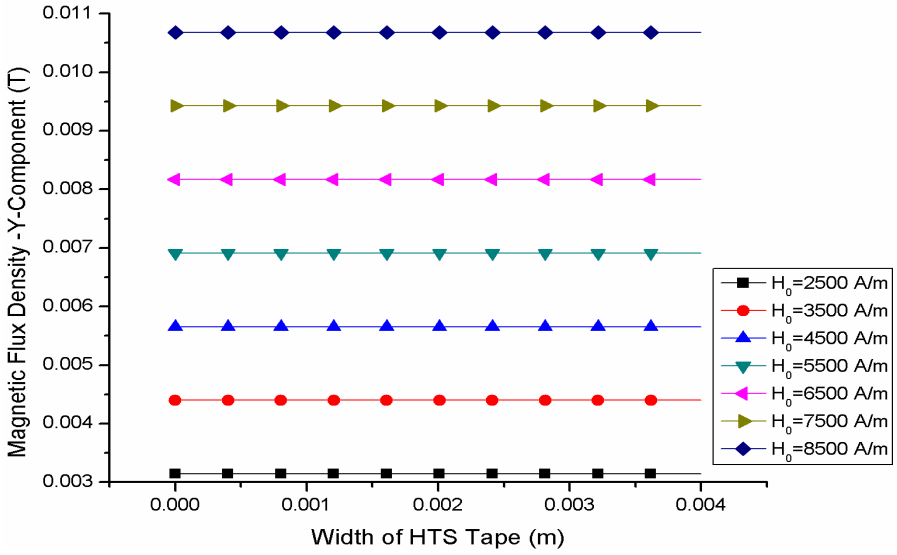

Figure 3-6: Variation of Y-Component of Magnetic Flux Density with externally applied Magnetic field at a current density of 2x10^7 *A/m^2*

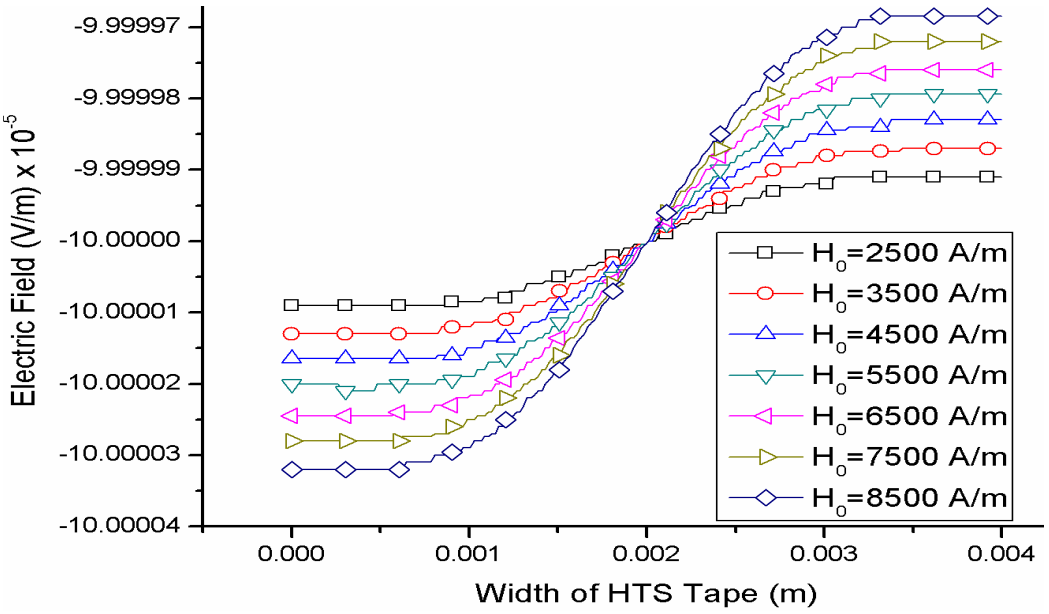

Figure 3-7: Variation of Z-Component of Electric field with externally applied Magnetic field at a current density of 2x10^7 *A/m^2*

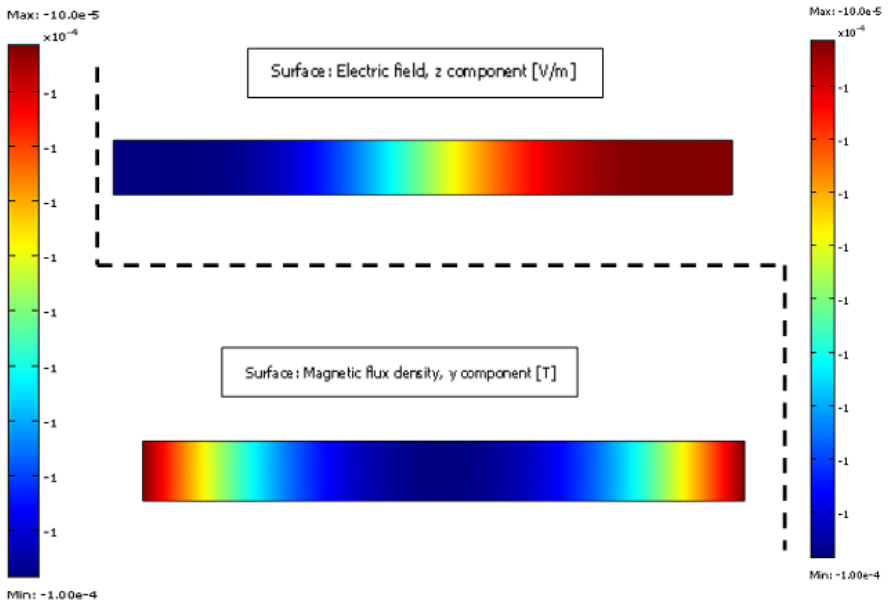

Figure 3-8: Magnetic flux and Electric field distribution contours in the HTS Tape at an external field of 6500 *A/m* and a current density of 2x10^7 *A/m^2*

Moreover, Y-Component of magnetic flux density is not affected with the increase in current density (results not shown here). The variation of electric field with applied magnetic field at a constant current density of 2x10^7 *A/m^2* is shown in Figure 3-7. The contours of *z*-component of electric field and *y*-component of magnetic flux density at a current density of 2x10^7 *A/m^2* and at an applied field of 6500 *A/m* is shown in Figure 3-8. It can be observed that the magnitude of magnetic flux density is minimum at the central portion of HTS tape indicating the drift due to applied external field.

3.3.3 *Transient AC Losses at Zero Field and at Applied Field*

Time dependent AC losses are predicted using Computational Electro Dynamics (CED) for the span of 1 hour (*t=3600*) starting from *t=0*. Equation (61) is used for this purpose. Recently, a periodic space-time formulation was proposed [13] to compute the AC losses in coated conductors.

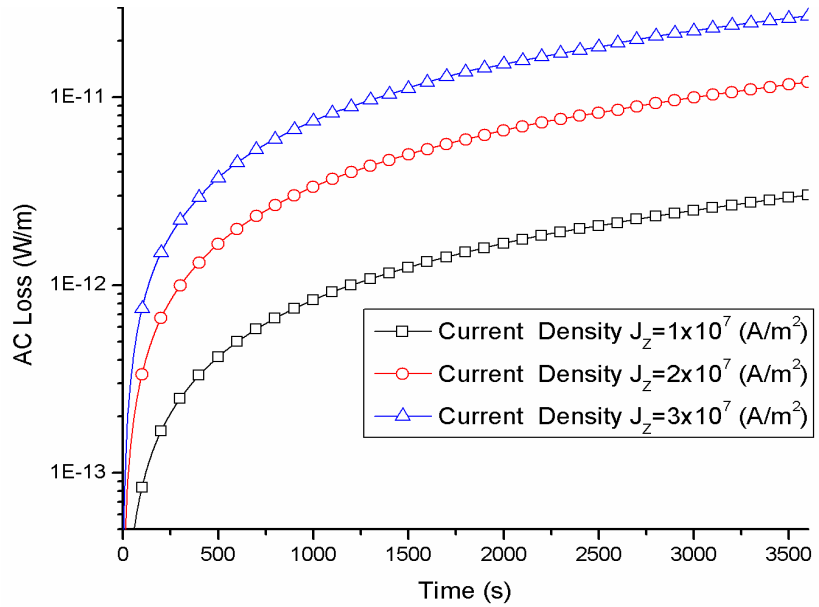

Figure 3-9: AC Loss prediction as a function of Current density for the span of 1 hour at Zero external magnetic field

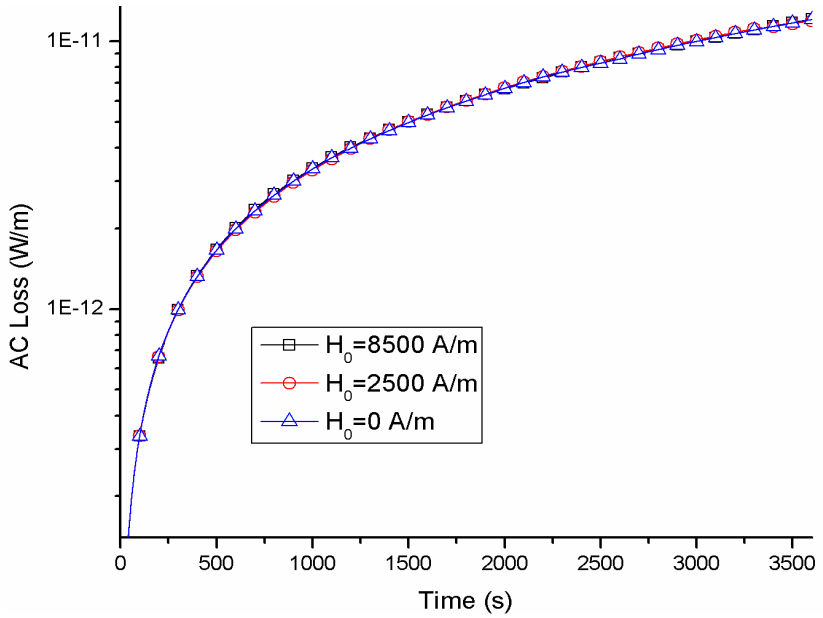

Figure 3-10: Time dependent AC Loss prediction at different applied magnetic fields and at constant current density of 2x10^7 *A/m2*

However, a finite difference technique was used to discretize the governing equations. In the present work, we made an attempt to simulate transient problem of AC loss in HTS

tape using FEM. AC losses over a period of 3600 *s* with varying current density is presented in Figure 3-9. It can be observed that a steep increase in the initial period and after a period of time the slope of the curve becomes lower. In order to understand the effect of applied field on AC Loss, we have compared the results of AC Loss obtained at different applied fields at a constant transport current density of $2x10^7\ A/m^2$ as shown in Figure 3-10. It is evident from the Figure 3-10 that the effect of applied magnetic field on the AC loss as a function of time is marginal. The dominant factor in contributing to AC Loss is found to be transport current density in the HTS tape.

3.4 **Summary**

The AC loss analysis in HTS tapes using Computational Electrodynamics (CED) yield interesting results and conclude that the influence of external magnetic field on the transient AC losses would be insignificant. Further, it can also be concluded that the effect of current density on the AC losses is significant. In addition, it can also be concluded that these AC losses will be contributing to the heat loads which have to be removed using suitable cooling medium such as Liquid Cryogens or Supercritical fluids or coolant with the addition of nanoparticles. Cooling techniques are discussed in Chapter 5.

4 Structural Analysis on mandrel of SMES

In present scenario, the use of composite materials in advanced applications such as automotive, space, building, marine etc. are increased compared to metal alloys due to exceptional mechanical properties, excellent physical properties and better ratio of stiffness to density. The potential utilization of composite materials is increased in world for large scale applications in development of aircrafts (civil and military), Space launch vehicles and satellites. The major failures that are encountered in the composite material applications are damage due to impact loading, micro-cracking in the matrix of laminate and de-bonding of matrix with fiber. The development of durable and resistance to damage against impact loads and cracks in composites are still challenges to the researchers. In space applications the factors need to be considered are impact loads, thermal loads at cryogenic temperatures, crack propagation and initiation.

From the literature, it is observed that mechanical and metallurgical characterization of different materials is enhanced by cryogenic treatment. Table 4-1 shows the mechanical and metallurgical characterization of cryogenically treated materials. However, the development of better composite materials with mechanical characterization for space applications is still need to be studied. Motivated by this, the main objective of study is to develop and design a composite material that have better mechanical properties compared to conventional metal alloys at cryogenic temperatures. This can be achieved by treating composite materials with cryogenic liquid such as LN_2 to enhance mechanical properties and can be used in space applications at variable conditions. In order to predict the behaviour of composite materials in real time space applications, it is necessary to predict the mechanical characteristics. For this investigation, the composites made of Carbon and Kevlar fibers with HINPOXY C RESIN used as a matrix are cured and treated with cryocoolant LN_2 for different time intervals. An experimental investigation is carried to predict the mechanical characterization of cryogenic treated composite materials. It is observed that cryogenic treatment of composite materials has increased the flexural and tensile strength and is very useful for the space applications.

Table 4-1: Mechanical and Metallurgical characterization of Cryogenic treated materials

CHARACTERIZATION	PROPERTIES	MATERIALS USED
Mechanical	Wear resistance	As-sprayed WC coating [78], Tungsten Carbide [79], D6 tool steel [80]
	Tensile and interfacial	Polyacrylonitrile-based carbon fiber [81]
	Fatigue behavior and fracture	En 353 steel [82]
	Tensile, Wear and interfacial	Kevlar fibers [83]
	Shear stress and interfacial	Carbon Nanotube fiber /bisphenol-F epoxy composite [84]
	Residual stresses	2024 aluminum alloy [85]
	Fracture toughness and hardness	tool steels [86]
	Hardness and Stability	large rolls [87]
	tensile, flexural, and impact	wood-flour/high-density-polyethylene composites [88]
Metallurgical	Tool life and Productivity	HSS tool [89]
	Micro structure	AISID2 tool steel [90], En 31 bearing steel[91]
	Hardness and Strength	4340 Steel [92], Cracked M35 tool steel [93]
Combined (Mechanical and Metallurgical)	Microstructure and Mechanical Hardness	Cr8-Type Cold Work Die Steel [94]
	Microstructure, Mechanical and Wear behavior	AISI H13 hot work tool steel [95], AISI D2 steel [90]
	Strength, Hardness and Wear resistance	B4Cp/Al–12% Si composites [96]
	microstructure and properties, hardness and bending strength	WC−11Co cemented carbides [97]

4.1 **Mechanical Characterization**

The mechanical characterization of composites shows the behavior of composite materials under variable operating conditions. The composites of Carbon fiber and Kevlar fiber are tested to predict the mechanical characteristics under operating temperature of 300K when treated and untreated with cryocoolant i.e. LN_2. The preparation of composite samples and curing are shown in Table 4-2. After treating in cryocoolant immediately, these samples are tested in ASTM and UTM for flexural and tensile load. The results obtained after

experimentation is compared with the mechanical properties of both treated sample and untreated sample for comparison. The samples are made of different layers such as E is Epoxy, C is Carbon Fiber & K is Kevlar into a laminate. The samples used for the experimentation are shown in Table 4-2. The specifications of the UTM machine used for testing are shown in Table 4-3.

Table 4-2: Composite layered samples used for the testing

Fiber Used	According to material layer	Testing immediately after Cryogenically Treatment with different time intervals	Samples	Layers
Carbon Fiber	Double layer Carbon	0 hour,1 hour, 3 hour	5	ECECE
Kevlar Fiber	Single layer Kevlar	0 hour, 1 hour, 3 hour	5	EKE
	Double layer Kevlar	0 hour, 1 hour, 3 hour	5	EKEKE
Carbon & Kevlar Fiber	Hybrid layer	0 hour, 1 hour, 3 hour	5	ECEKE

Table 4-3 Specifications of Testing Machine

Machine Type	UTM
Model Name/Number	201T
Automation Grade	Automatic
Driving Method	Gear ,Motor
Accuracy	+/-1% As per IS 1828
Place Of Origin	INDIA
Brand	KMI, KMI
Fine load resolution	4000 counts for each measuring range
Material for Construction	MS, SS, others
Capacity	Upto 10 KN

4.2 **Experimental Procedure**

For the composite samples preparation, a mold of proper dimensions is needed according to ASTM standards. Two different types of molds are prepared for Flexural (3-point testing) and tensile testing. For 3 point bending test, ASTM 7264 i.e. 32:1 length to thickness is used. According to the standard, a mould of 128mm length, 4mm thickness and 20mm width is prepared. The mould was made by Polycarbonate sheet. For smooth

surface finishing the mould was cut by laser cutting. In a single plate 7 cutting was made for the samples. Figure 4-2 shows the preparation of mould with Polycarbonate sheet using Laser Cutting.

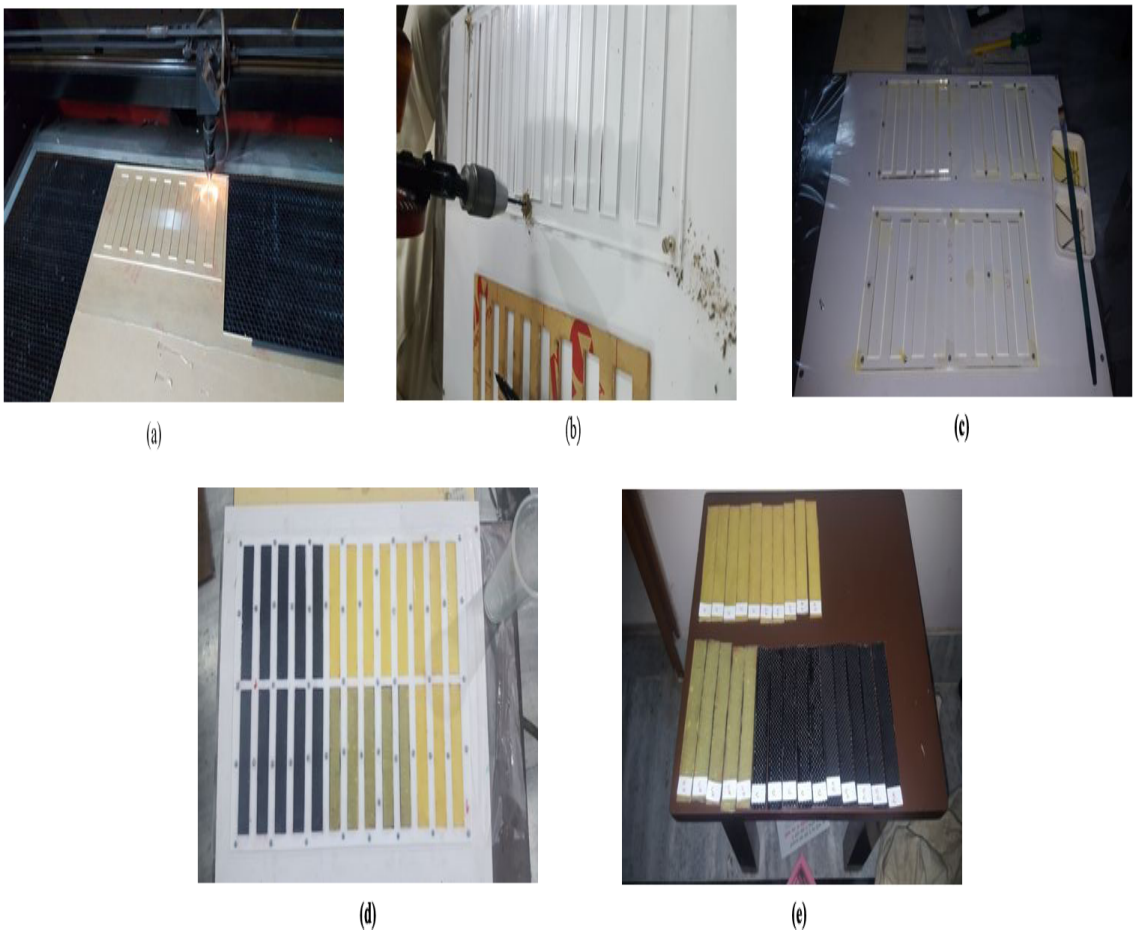

Figure 4-1: (a) Preparation of Mould with Polycarbonate sheet using laser cutting (b) Tightening the polycarbonate sheet (c) Oil courting (d) Curing of samples (e) Composite Samples after curing

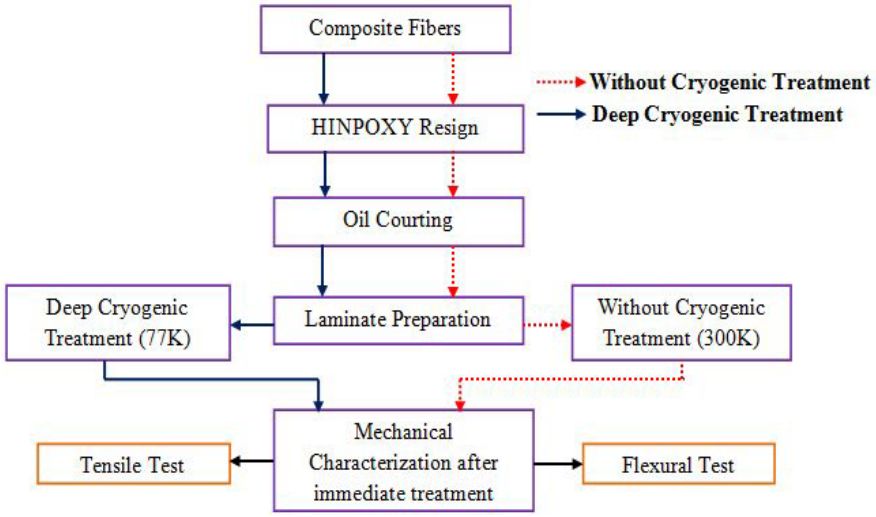

Figure 4-2 Research Methodology

The epoxy made my mixing resin and hardener in ration 100:30 by weight is taken and stirred vigorously for 10-15 minutes. The level of the surface was check by spirit level. The hole were made by using hand drill to be tightened by the 6mm long steel screw so that the epoxy should not get spread from one slots to other slots. A layer of wax or oil courting was done with the help of brush all around the slots so that after curing samples can easily removed. A layer of epoxy was poured at the bottom of every slot. The Carbon and Kevlar fibers are placed as per the requirement. Epoxy was filled on the top of the layer of every slot. The samples are cured at room temperature for 24 hours and removed from the polycarbonate sheet. ASTM and UTM are used for flexural and tensile testing of composite samples. The graphs were generated with the help of commercial UTM 5.5.1 software installed in the system attached to machine.

Figure 4-3: (a) Flexural testing of sample in ASTM (b) Tensile testing of sample in UTM

4.3 Results and Discussion

The mechanical properties such as flexural and tensile of samples which are made of Carbon fiber and Kevlar fiber before and after cryogenic treatment are measured. The results were compared for both the conditions, cryogenically treated and untreated. The number of samples used for testing both the tensile test and flexural test loads are 50.

4.3.1 *Comparison between Untreated and One Hour Cryogenically Treated Composite Materials*

4.3.1.1 Flexural Load Vs Displacement

Figure 4-4 shows the variation of displacement with respect to load under flexural load. Different composite samples are tested flexurally before treating in Liquid Nitrogen (LN_2) and it is observed that Single Layer Kevlar Composite sample withstand for peak load of 30kg with a displacement of 4 mm compared to other composite samples and rupture starts with further loading and the flexural failure of Double Layer Kevlar Composite is less compared to other composite samples. However, when the samples are cryogenically treated for one hour the flexural strength of Double Layer Carbon Composite sample is high and the failure takes place at 27kg at a displacement of 10mm. Hence, it is observed that flexural strength of Double Layer Carbon is higher when treated cryogenically for one hour.

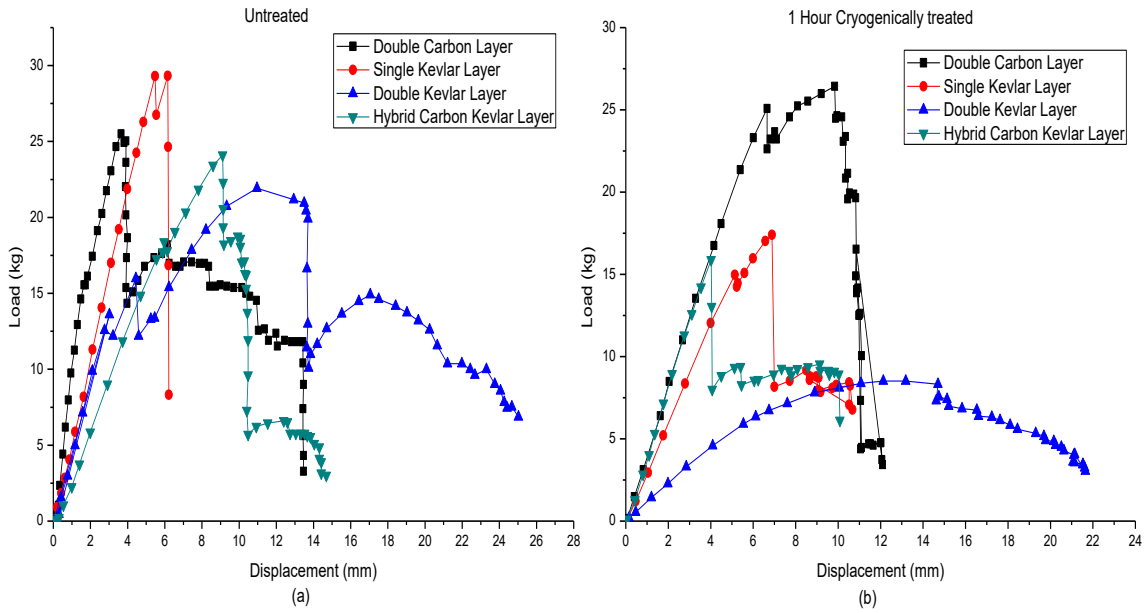

Figure 4-4: Variation of Displacement with respect to Load for different composites under Flexural load when (a) Cryogenically untreated (b) 1 hour Cryogenically treated

4.3.1.2 Flexural Stress Vs Strain

Figure 4-5 shows the variation of Stress with respect to Strain under Flexural loads. From the experimentation of different composite samples, it is observed that flexural strength is higher for Single Layer Kevlar with an elongation of 0.05mm at the peak load when the samples are untreated in LN_2. Hook's law is followed by the samples and at the yield point a brittle failure is occurred in all the samples. Further, when the samples are cryogenically

treated and tested for one hour, yield strength is increased and the brittle failure does not occurs prior when compared with samples are untreated in LN_2. Double Layer Carbon is having the highest flexural strength with an elongation of 0.10 mm at peak load when it is cryogenically treated before brittle failure.

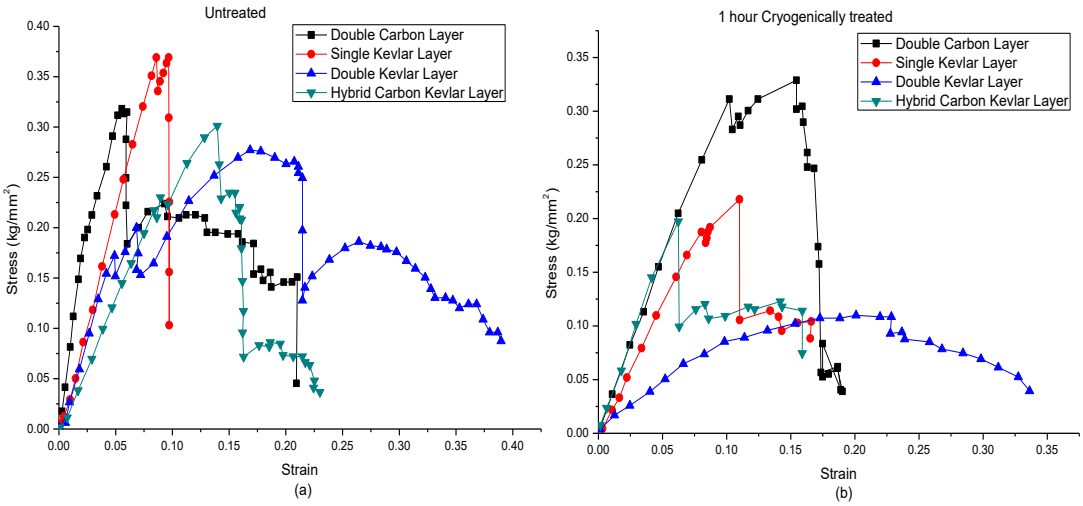

Figure 4-5: Variation of Stress with respect to Strain for different composite materials under Flexural load when (a) Cryogenically untreated (b) 1 hour Cryogenically treated

4.3.1.3 Tensile Load Vs Displacement

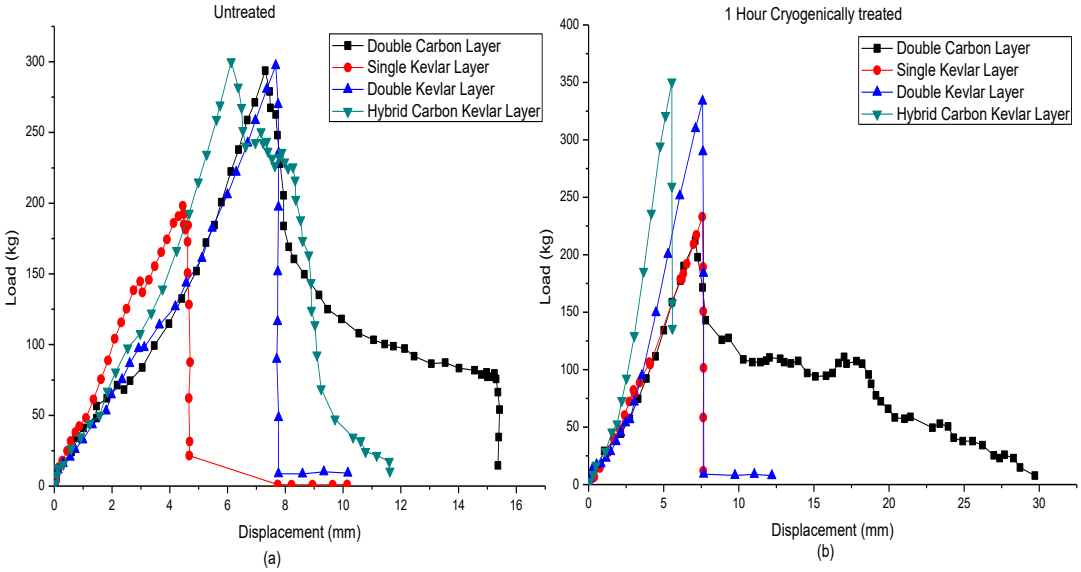

Figure 4-6: Variation of Displacement with respect to Load for different composites under Tensile load when (a) Cryogenically untreated (b) 1 hour Cryogenically treated

Figure 4-6 shows the variation of displacement with respect to load under tensile loads. The composite samples when untreated with the LN_2, the displacement increases with the increase in the load and brittle failure occur in every sample. In Single Layer Kevlar, the

brittle facture occurs prior compared to other samples. The maximum possible load that can withstand is 300kg with a displacement of 8mm for Double Layer Kevlar. When the samples are cryogenically treated for one hour the tensile load withstand increased for all the samples and decreased in Double Layer Carbon. However, the brittle failure occurs with reduced displacement compared with untreated composite samples at higher peak loads.

4.3.1.4 Tensile Stress Vs Strain

The variation of Stress with respect to Strain under tensile load is shown in Figure 4-7. The proportionality between Stress and Strain is followed by the composite samples and after the limit of proportionality a brittle failure is observed. When the composite samples are untreated with LN_2, the maximum stress withstand by the composite samples are $8kg/mm^2$ except Single Layer Kevlar having less resistance to withstand the load.

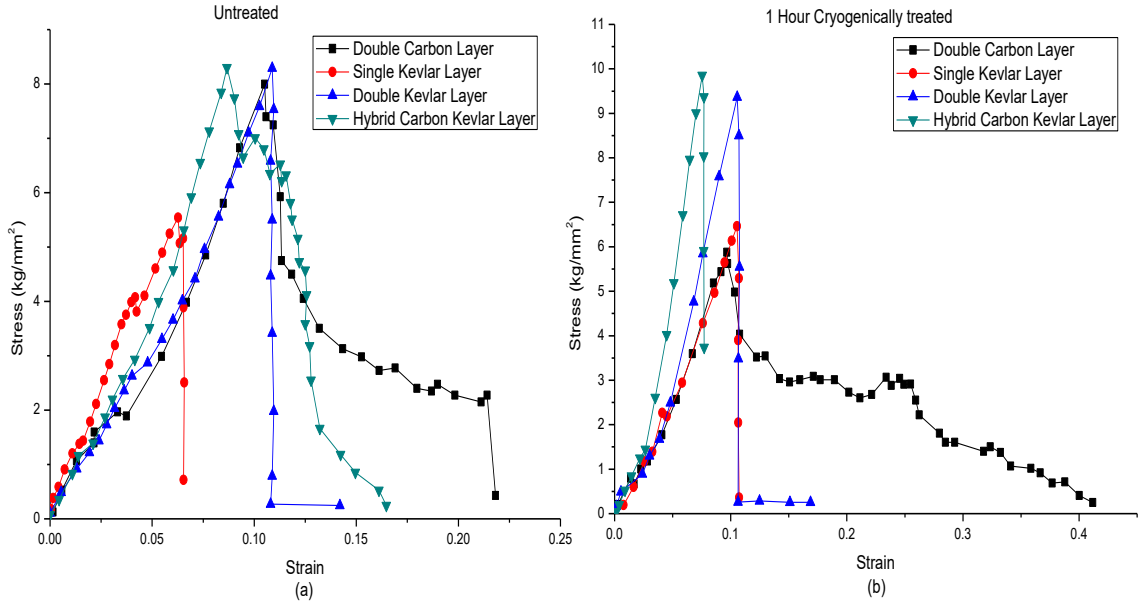

Figure 4-7: Variation of Stress with respect to Strain for different composites under Tensile load when (a) Cryogenically untreated (b) 1 hour Cryogenically treated

Further, when the samples are treated cryogenically for one hour, the Stress sustainability is increased for the samples and in case of Double Layer Carbon it is decreased compared to other samples. From the experimentation, it is observed that the samples untreated in LN_2 having the lower Strain compared to one hour treated before the brittle facture occurs in the samples.

4.3.2 *Mechanical Characterization of Composite Materials with and without Cryogenic Treatment*

4.3.2.1 Flexural Load Vs Displacement

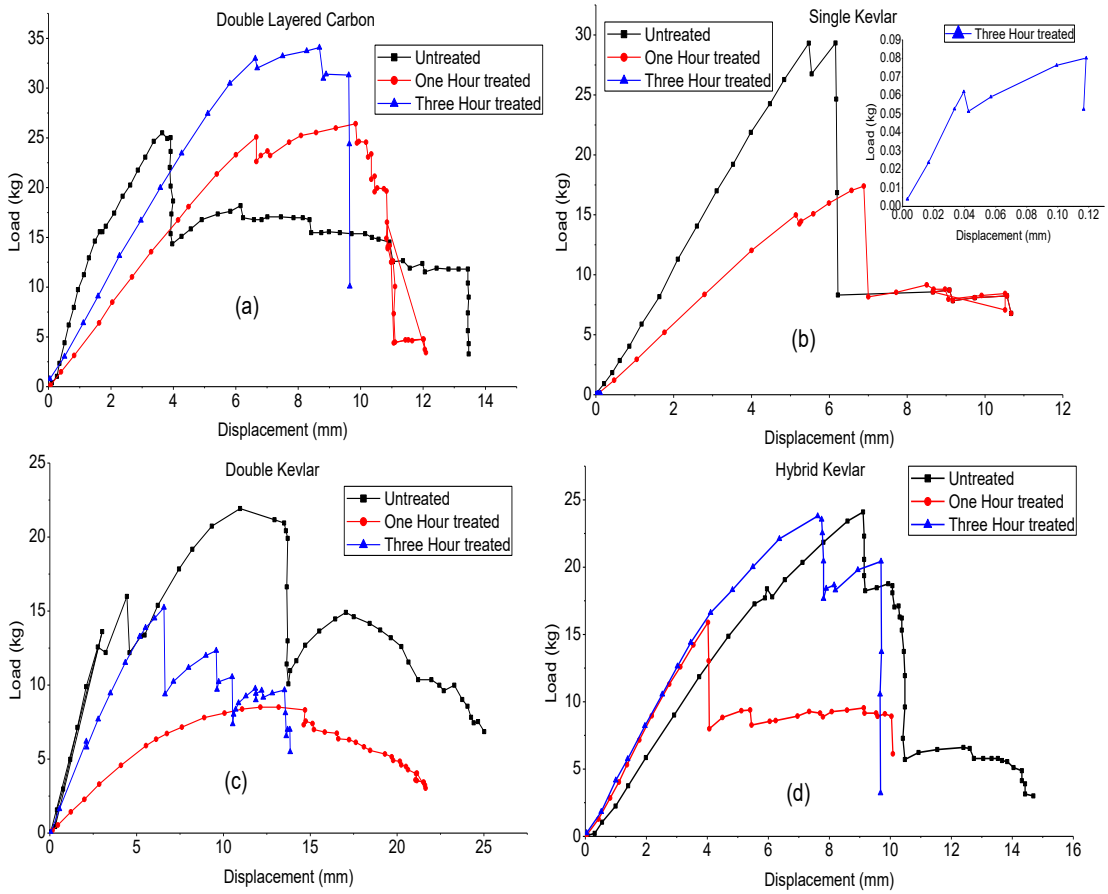

Figure 4-8: Variation of Displacement with respect to Load for different composites treated in Liquid Nitrogen (LN_2) under Flexural load (a) Double Layer Carbon (b) Single Layer Kevlar (c) Double Layer Kevlar (d) Hybrid Composite

The samples of Carbon and Kevlar fiber composite materials are untreated and treated for one, three hours in cryogenic liquid (LN_2) and tested under flexural load is shown in Figure 4-3. The results of the experimentation are shown in Figure 4-8 and it is evident that Double carbon Layer when cryogenically treated for three hours, its load carrying capability has increased. However, Kevlar in Single layer have better resistance towards the load when untreated and lower displacement to peak loads. Further, the Double Layer Kevlar and Hybrid (Carbon and Kevlar) Composite show better results for peak loads Vs Displacement when treated for three hours. Sample of Double Layer Carbon treated cryogenically for three hours has the highest load resistive capability of 35kg and displacement of 10mm compared to other samples.

4.3.2.2 Flexural Stress Vs Strain

Flexural load is applied on different samples before cryogenic treatment and after cryogenic treatment for one hour and two hours and the variation of stress with respect to Strain is shown in Figure 4-9.

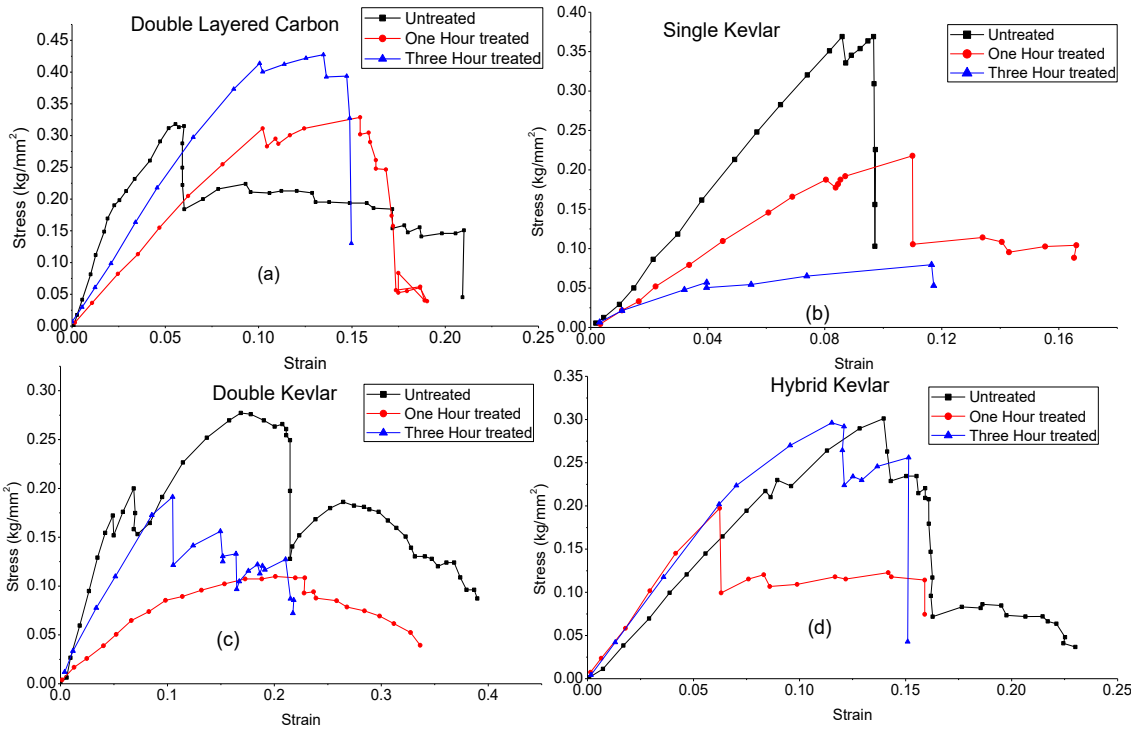

Figure 4-9: Variation of Stress with respect to Strain for different composites treated in Liquid Nitrogen (LN_2) under Flexural load (a) Double Layer Carbon (b) Single Layer Kevlar (c) Double Layer Kevlar (d) Hybrid Composite

After the proportionality limit, due to cryogenic treatment brittle failure occurred in all the samples with higher strain at peak loads. Three hours treated Double layer Kevlar and Hybrid Composite shows the better results than cryogenic untreated composites. Double Layer Carbon has the maximum Stress of 0.43kg/mm^2 when cryogenically treated for three hours in LN_2.

4.3.2.3 Tensile Load Vs Displacement

Different Samples made up of composites are tested under tensile load to predict the failure due to brittle fracture and the results are shown in Figure 4-10. From the experimentation, it is observed that cryogenic treatment of the composite samples increases the brittleness and immediately after the proportionality limit the brittle fracture takes place in the samples.

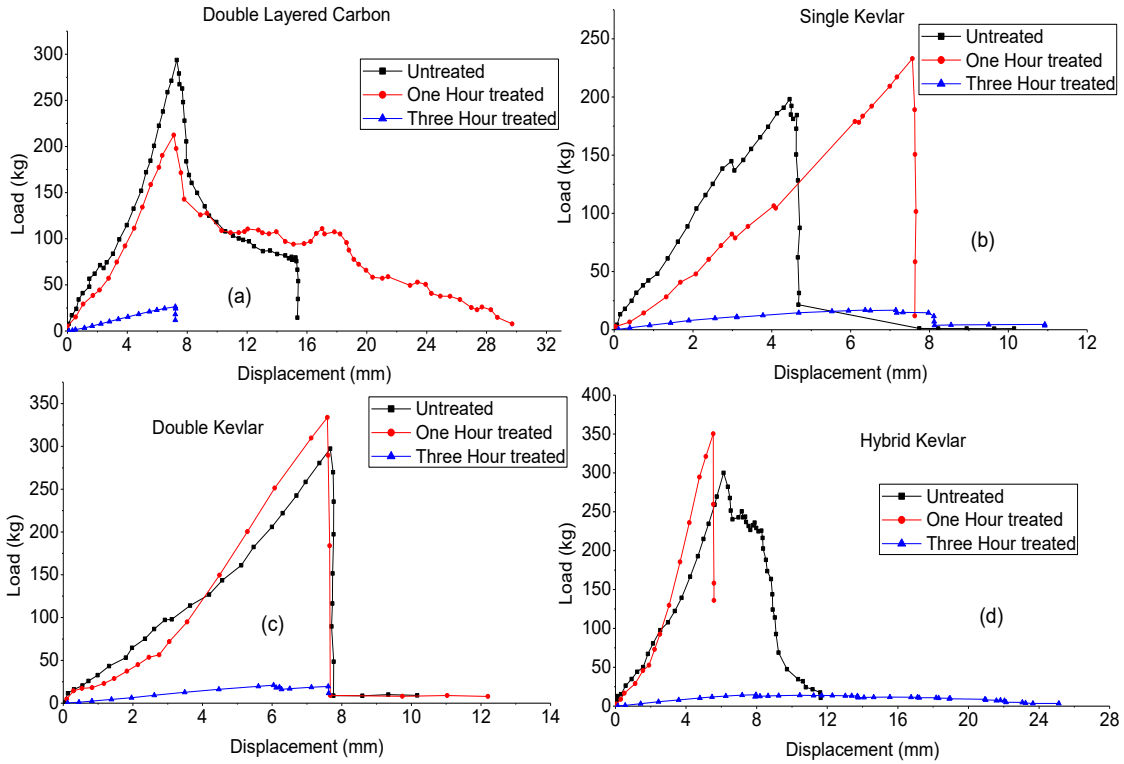

Figure 4-10: Variation of Displacement with respect to Load for different composites treated in Liquid Nitrogen (LN_2) under Tensile load (a) Double Layer Carbon (b) Single Layer Kevlar (c) Double Layer Kevlar (d) Hybrid Composite

However, compared to the untreated the displacement with respect to peak load is higher in the composites that are treated cryogenically. The composites having Kevlar Layer shows the better results when they are treated cryogenically for one hour. Double and Hybrid Kevlar having the highest load carrying capacity of 350 kg with a displacement of 8mm at the peak loads.

4.3.2.4 Tensile Load Vs Strain

Figure 4-11 shows the cryogenically treated and untreated composite samples used in experimentation for determining the mechanical characterization. The resistance against the brittle facture is increased by cryogenic treatment of the composite samples having Kevlar layers and Carbon layers at peak loads.

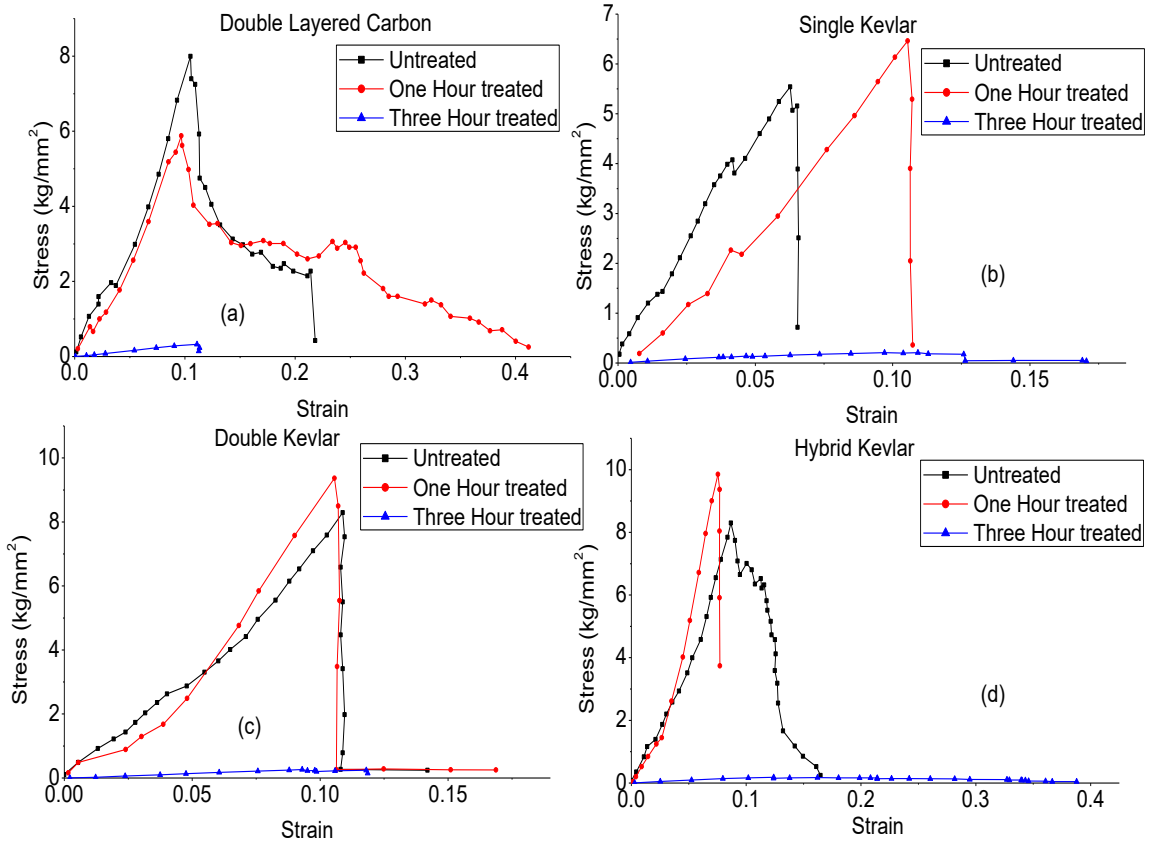

Figure 4-11: Variation of Stress with respect to Strain for different composites treated in Liquid Nitrogen (LN_2) under Tensile load (a) Double Layer Carbon (b) Single Layer Kevlar (c) Double Layer Kevlar (d) Hybrid Composite

The layers with Kevlar shows better stress and strains with maximum values of 10kg/mm^2 and 0.1 approximately. However, in hybrid composites the brittle failure takes place prior compared to Kevlar composites.

4.4 Summary

From the experimental investigation, mechanical characterization of different composite samples is predicted with and without cryogenic treatment for Superconducting Magnetic Energy Storage applications. The composite samples when treated cryogenically show better strength against the brittle failure. It is observed that the Double Layer Carbon Fiber, the peak load capacity for flexural testing various from 25.38 to 34.01 N for untreated and three hour treated fiber respectively. The cryogenically treated Double Layer Carbon Fiber has an increment of 34% in peak load capacity. The Hybrid Composite with Carbon Kevlar Fiber has a peak load capacity for flexural testing various from 24.14 to 25.67 N for untreated and three hours treated. There is an increase about 6% in peak load capacity. The Single Layer Kevlar Fabric has peak load capacity for tensile testing various from 198 to 233.5 N for untreated and immediate 1 h treated fiber respectively.

5 Thermohydraulic Performance of SMES

5.1 Generalized thermo-electrical strategy for designing superconducting coil

The designing of superconducting coil depends on the electric current flow in the coil and joule heat generation due to flow of electrical current [98].

Heat transport in SMES can be solved using conventional heat transfer equation,

$$\rho_g c_p \frac{\partial T}{\partial t} - \rho_g c_p u.\nabla T = \nabla.(k\nabla T) + Q \quad (62)$$

where, ρ_g is density of coil configuration used, c_p is specific heat of coil, T is temperature, Q is heat source, k is thermal conductivity of coil, u is velocity vector.

Since, convection can be neglected in solids. Equation (62) can be written as

$$\rho_g c_p \frac{\partial T}{\partial t} - \nabla.(k\nabla T) = Q \quad (63)$$

From the joule heating and from the basis of super conductivity

$$Q = E.J \quad (64)$$

where, J =total current density, E =electric field strength and can be written as

$$E = -\nabla V \quad (65)$$

where, V =electric potential

From E-J power law

$$\frac{E}{E_0} = \left(\frac{J}{J_c}\right)^n$$

$$(66)\, J = \left(\frac{1}{\rho} + \varepsilon \frac{\partial}{\partial t}\right) E + J_e \quad (67)$$

where, J_e =total current density, ε =electric permittivity, ρ = resistivity of superconductor

Further the heat conducted due to electric current flow and joule heat generation from the HTS coil is dissipated to the cryostat.

Electrical resistivity can be calculated by

$$\frac{T}{\rho k} = constant \tag{68}$$

$$-n\left(-k\nabla T\right) - q_0 = h\left(T_\infty - T_s\right) + e\sigma\left(T_{amb}^4 - T_s^4\right) \tag{69}$$

where, n=unit vector normal to a boundary surface of the HTS coil. h=heat transfer coefficient of cryogenic fluid, q_0=inward heat flux, T_∞=Bulk temperature of cryogenic fluid, T=Surface temperature, e=Emissivity of the coefficient of the coil, σ=Stefan Boltzmann constant. The convection heat transfer coefficient depends on geometrical configuration of HTS coil, surface temperature, thermophysical properties of cryogenic coolant.

5.2 Thermophysical Properties of Cryogenic coolants used in analysis

5.2.1 *Thermophysical Properties of SCN*

The objective of the present study is to investigate the thermohydraulic performance of the SMES when SCN is employed as cryogenic coolant. The temperature dependent thermophysical properties of SCN are considered for the analysis.

5.2.1.1 Evaluating the Thermophysical Properties of SCN

The correlations should be developed for the Thermophysical properties such as Thermal Conductivity, Specific heat, Viscosity and Density because they are varying with the temperature. These correlations are used for simulating the Computational Dynamics of the SCN flow in the different corrugations. The Thermophysical properties are studied from NIST data [99].

1) Density

Figure 5-1 shows the variation of density with the temperature of SCN is shown above to the critical temperatures. From the figure it is evident that, as the temperature of the SCN increases density decreases because temperature and density are inversely proportional to each other.

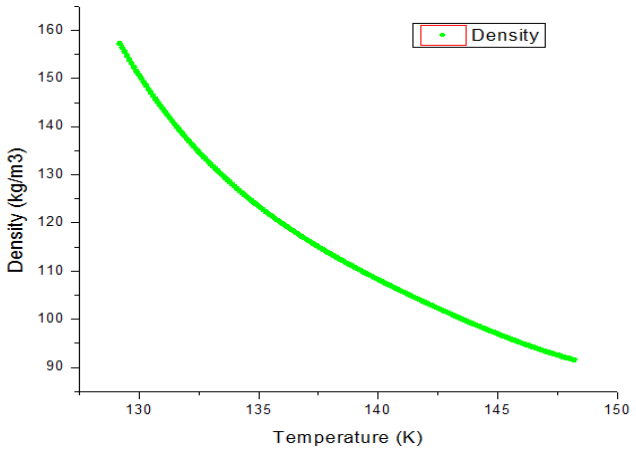

Figure 5-1: Variation of Density with respect to Temperature

2) Viscosity

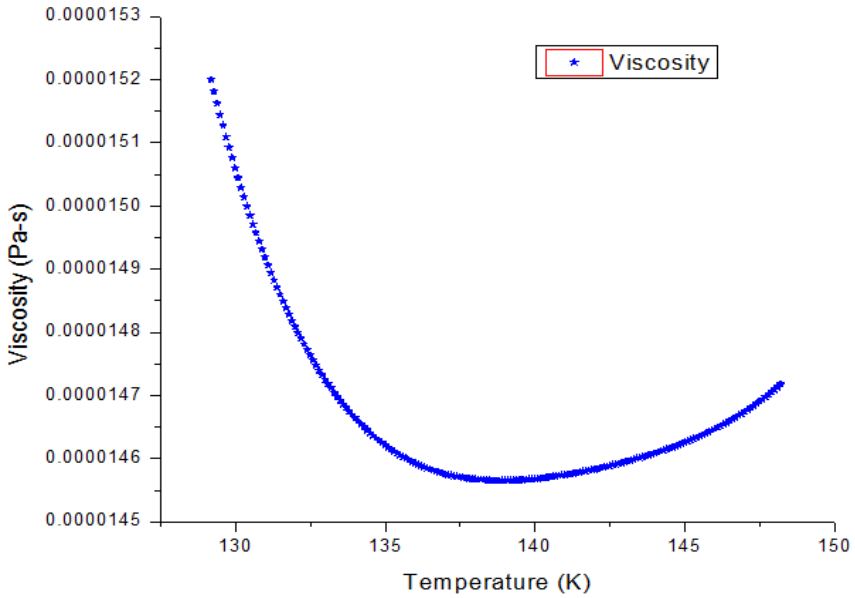

Figure 5-2: Variation of Viscosity with respect to Temperature

Figure 5-2 shows the variation of viscosity with the temperature of SCN is shown above to the critical temperatures. From the figure it is evident that, as the temperature of the SCN increases viscosity decreases later it increases with the increase in the temperature above 140K.

3) Specific heat

Figure 5-3 shows the variation of specific heat with the temperature of SCN is shown above to the critical temperatures. From the figure it is evident that, as the temperature of the SCN increases Specific heat decreases. For the SCN, Specific heat is very high compared to the other cryogenic coolants and is approximately 740kJ/kg-K.

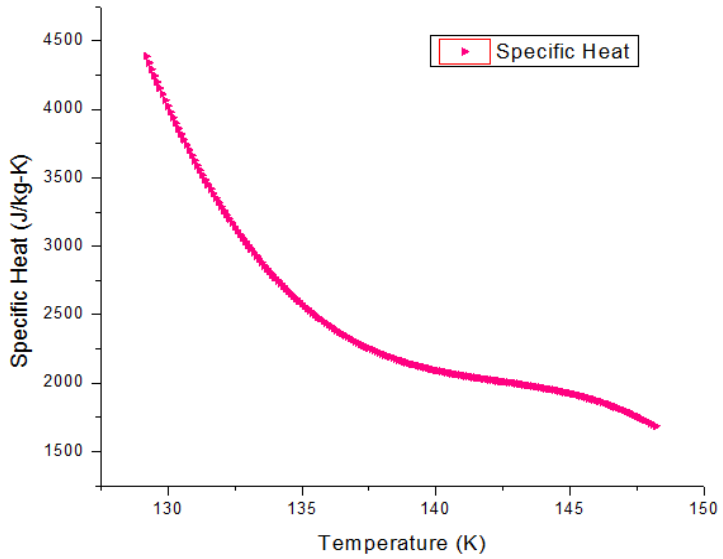

Figure 5-3: Variation of Specific heat with respect to Temperature

4) Thermal Conductivity

Figure 5-4 shows the variation of thermal conductivity with the temperature of SCN is shown above to the critical temperatures. From the figure it is evident that, as the temperature of the SCN increases thermal conductivity decreases.

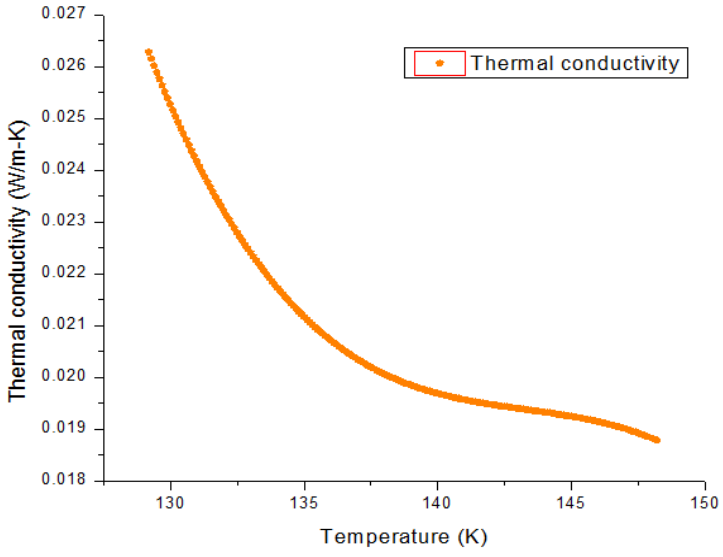

Figure 5-4: Variation of Thermal conductivity with respect to Temperature

5.2.1.2 Development of Thermophysical properties of SCN

In any engineering system, the selection of thermophysical properties is crucial while estimating the thermohydraulic performance. From the NIST database, the thermophysical properties of SCN at a pressure of 33.958 bar and temperature of 129.19 K are extracted [100]. The polynomial functions are developed to achieve the relationship of independent

variables with the dependent variables. The range of temperatures is chosen in such a way that the operating temperature of HTS tapes would be below the critical temperature of HTS tapes.

Table 5-1: Coefficients of analytical functions for temperature dependent thermophysical properties of SCN

Thermophysical Properties	Polynomial function	Coefficients of polynomial function
Density (kg/m^3)	$\rho(T) = a + \rho_1 T + \rho_2 T^2 + \rho_3 T^3 + \rho_4 T^4$	a = 229112.6 ρ_1 = -6415.201 ρ_2 = 67.48431 ρ_3 = -0.31584 ρ_4 =5.547 x 10^{-04}
Specific Heat (J/kg-K)	$C_p(T) = b + C_{p1} T + C_{p2} T^2 + C_{p3} T^3 + C_{p4} T^4$	b = 2490240 C_{p1} = -52349.22 C_{p2} = 367.3157 C_{p3} = -0.85959 C_{p4} =9.349936x10^{-11}
Thermal Conductivity (W/m-K)	$k(T) = c + k_1 T + k_2 T^2 + k_3 T^3 + k_4 T^4$	c = 6.20177 k_1 = -0.12928 k_2 = 5.2237 x 10^{-06} k_3 =9.1 x 10^{-04} k_4 =1.89 x 10^{-16}
Viscosity (Pa-s)	$\mu(T) = d + \mu_1 T + \mu_2 T^2 + \mu_3 T^3 + \mu_4 T^4$	d = 0.00804 μ_1 = -2.25514 x 10^{-04} μ_2 = 2.377x 10^{-06} μ_3 = -1.1143 x 10^{-08} μ_4 = 1.9596 x 10^{-11}

The developed functions are in the temperature range of 129.19 K - 149.99 K and 210 data points are used for fourth order polynomial fit. To attain the super critical state of cryogenic fluids and the utilizing such fluids as a cryogenic coolant in HTS SMES for cooling HTS SMES are great challenges to the researchers. The objective of the present study is to investigate the thermohydraulic performance of the SMES when SCN is employed as cryogenic coolant. The temperature dependent thermophysical properties of SCN are considered for the analysis. Table 5-1 shows the polynomial functions and their

coefficients which are further utilized in predicting the thermohydraulic performance in SMES.

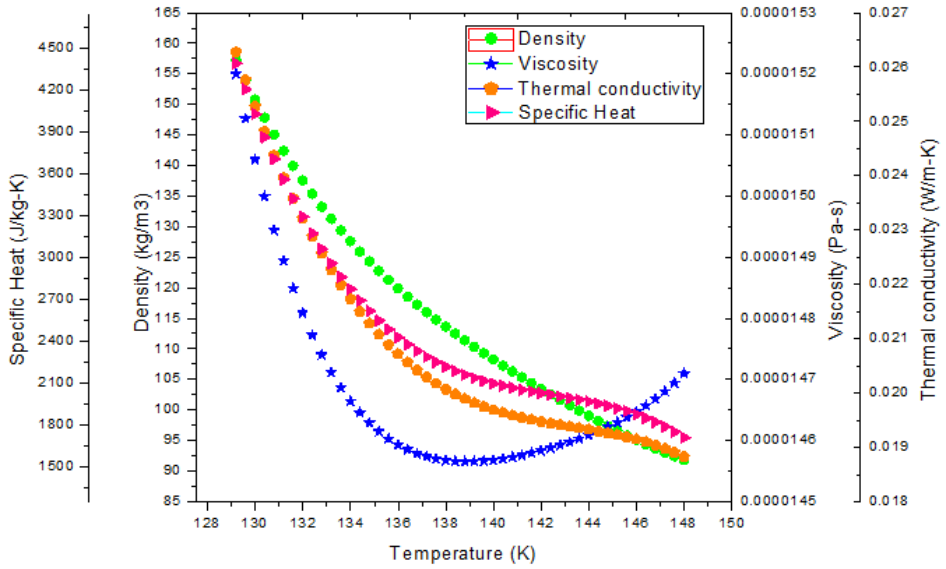

Figure 5-5: Temperature dependent thermo-physical properties of SCN at corresponding saturation pressures

5.3 Thermophysical properties of LN_2 used for central channel flow in SMES

The transportation and thermodynamic properties are vital for the simulation of hydraulic and convective heat transfer in HTS SMES. For better accuracy of analysis, the temperature dependent thermophysical properties are used in the present investigation for flow of LN_2 through HTS cable. This properties such as density, viscosity, thermal conductivity and specific heat are extracted from the NIST database [100]. Figure 5-6 shows the both hydraulic and thermal temperature dependent thermophysical properties of LN_2 operated at temperature range of 77-86 K and at an operating pressure of 2.7 bar [101] as shown in Table 5-2.

Table 5-2: Thermophysical properties of LN_2 used for the analysis

Properties	Operating temperature (K)	Analytical function	Coefficients of analytical function
Density (kg/m^3)	65	$\rho = a_1 + \rho_1 T + \rho_2 T^2$	a_1 = 1001.73488, ρ_1 = -0.50588, ρ_2 = -0.02609
	67	$\rho = a_2 + \rho_1 T + \rho_2 T^2$	a_2 = 1001.73488, ρ_1 = -0.50588, ρ_2 = -0.02609
	69	$\rho = a_3 + \rho_1 T + \rho_2 T^2$	a_3 = 1001.73488, ρ_1 = -0.50588, ρ_2 = -0.02609
	71	$\rho = a_4 + \rho_1 T + \rho_2 T^2$	a_4 = 1001.73488, ρ_1 = -

			0.50588, ρ_2 = -0.02609
	73	$\rho = a_5 + \rho_1 T + \rho_2 T^2$	a_5 = 1001.73488, ρ_1 = -0.50588, ρ_2 = -0.02609
	75	$\rho = a_6 + \rho_1 T + \rho_2 T^2$	a_6 = 1001.73488, ρ_1 = -0.50588, ρ_2 = -0.02609
	77	$\rho = a_7 + \rho_1 T + \rho_2 T^2$	a_7 = 1001.73488, ρ_1 = -0.50588, ρ_2 = -0.02609
Specific Heat (J/kg-K)	65	$C_p = b_1 + C_{p1} x + C_{p2} x^2$	b_1 = 3219.43549, C_{p1} = -35.10567, C_{p2} = 0.25667
	67	$C_p = b_2 + C_{p1} x + C_{p2} x^2$	b_2 = 3219.43549, C_{p1} = -35.10567, C_{p2} = 0.25667
	69	$C_p = b_3 + C_{p1} x + C_{p2} x^2$	b_3 = 3219.43549, C_{p1} = -35.10567, C_{p2} = 0.25667
	71	$C_p = b_4 + C_{p1} x + C_{p2} x^2$	b_4 = 3219.43549, C_{p1} = -35.10567, C_{p2} = 0.25667
	73	$C_p = b_5 + C_{p1} x + C_{p2} x^2$	b_5 = 3219.43549, C_{p1} = -35.10567, C_{p2} = 0.25667
	75	$C_p = b_6 + C_{p1} x + C_{p2} x^2$	b_6 = 3219.43549, C_{p1} = -35.10567, C_{p2} = 0.25667
	77	$C_p = b_7 + C_{p1} x + C_{p2} x^2$	b_7 = 3219.43549, C_{p1} = -35.10567, C_{p2} = 0.25667
Thermal Conductivity (W/m-K)	65	$K = c_1 + K_1 x + K_2 x^2$	c_1 = 0.34223, K_1 = -0.00294, K_2 = 5.2237 x 10^{-06}
	67	$K = c_2 + K_1 x + K_2 x^2$	c_2 = 0.34223, K_1 = -0.00294, K_2 = 5.2237 x 10^{-06}
	69	$K = c_3 + K_1 x + K_2 x^2$	c_3 = 0.34223, K_1 = -0.00294, K_2 = 5.2237 x 10^{-06}
	71	$K = c_4 + K_1 x + K_2 x^2$	c_4 = 0.34223, K_1 = -0.00294, K_2 = 5.2237 x 10^{-06}
	73	$K = c_5 + K_1 x + K_2 x^2$	c_5 = 0.34223, K_1 = -0.00294, K_2 = 5.2237 x 10^{-06}
	75	$K = c_6 + K_1 x + K_2 x^2$	c_6 = 0.34223, K_1 = -0.00294, K_2 = 5.2237 x 10^{-06}
	77	$K = c_7 + K_1 x + K_2 x^2$	c_7 = 0.34223, K_1 = -0.00294, K_2 = 5.2237 x 10^{-06}

Viscosity (kg/m-s)	65	$\mu = d_1 + \mu_1 x + \mu_2 x^2$	$d_1 =$ 0.00147, $\mu_1 =$ -2.75384 x 10^{-05}, $\mu_2 =$ 1.3752 x 10^{-07}
	67	$\mu = d_2 + \mu_1 x + \mu_2 x^2$	$d_2 =$ 0.00147, $\mu_1 =$ -2.75384 x 10^{-05}, $\mu_2 =$ 1.3752 x 10^{-07}
	69	$\mu = d_3 + \mu_1 x + \mu_2 x^2$	$d_3 =$ 0.00147, $\mu_1 =$ -2.75384 x 10^{-05}, $\mu_2 =$ 1.3752 x 10^{-07}
	71	$\mu = d_4 + \mu_1 x + \mu_2 x^2$	$d_4 =$ 0.00147, $\mu_1 =$ -2.75384 x 10^{-05}, $\mu_2 =$ 1.3752 x 10^{-07}
	73	$\mu = d_5 + \mu_1 x + \mu_2 x^2$	$d_5 =$ 0.00147, $\mu_1 =$ -2.75384 x 10^{-05}, $\mu_2 =$ 1.3752 x 10^{-07}
	75	$\mu = d_6 + \mu_1 x + \mu_2 x^2$	$d_6 =$ 0.00147, $\mu_1 =$ -2.75384 x 10^{-05}, $\mu_2 =$ 1.3752 x 10^{-07}
	77	$\mu = d_7 + \mu_1 x + \mu_2 x^2$	$d_7 =$ 0.00147, $\mu_1 =$ -2.75384 x 10^{-05}, $\mu_2 =$ 1.3752 x 10^{-07}

5.4 Mathematical methods for estimating the thermophysical properties of Novel cryogenic coolant with dispersion of nano particles for cooling SMES

Due to massive developments in usage of cryogenic fluid and material in order to acquire low temperatures, there has been increase in demand of these materials in various applications such as food preservation, cryogenic fuels, medicine and surgery. A majority of these application use liquid nitrogen due to abundant existence. Liquid Oxygen can be used as a substitute for liquid nitrogen. Similarly, other applications like cryo-surgery, cyro-therapy, cryogenic fuels, etc can be replaced by liquid oxygen. Various industrial methods like fractional distillation in cryogenic air separation plant and also as propellant for space craft in rocket science use liquid oxygen. In order to improve these technologies nano particles were introduced into these fluids which can enhance the thermo physical properties of the fluids.

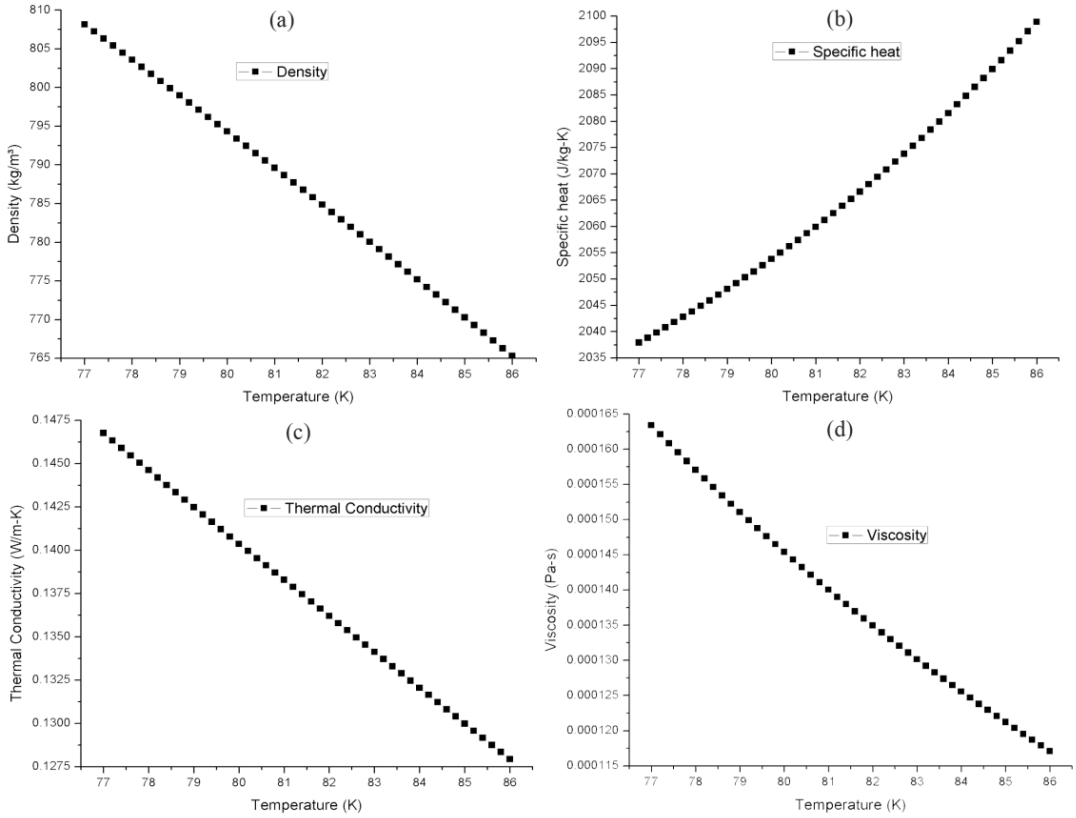

Figure 5-6: Temperature dependent thermophysical properties of LN_2 at 77K and 2.7 bar

5.4.1 *Selection of nanoparticle*

Selection of a particular nanoparticle is primal for the variation of thermo physical properties in the nanocryogenic fluid. Based on the properties of nanoparticles, properties of cryogenic coolants like density, specific heat, thermal conductivity and viscosity changes takes place.

Table 5-3: Thermo physical properties of nano particle

Nano particle	Density (ρ) kg/m³	Thermal conductivity, W/m-K	Specific heat (c_P) J/kg-k
TiO2	4157	13	710

Nano particles are in form of metallic (Al, Cu, Si) and metallic oxides such Al_2o_3, Sio_2, Sic, Tio_3 and CuO nano articles. To prepare these nano-fluids, nanoparticles with particular volume fraction is suspended uniformly in base fluid. It can to be noted that volume fraction of 1 - 5% nanoparticles are considered by authors. [1-3] it was also reported by Mustafa. [4] reported that the fluid flow would be non-Newtonian in nature beyond 6% of volume fraction of nanoparticles. Further, the thermo physical properties depend upon the volume fraction of nanoparticles. Dispersion of these nanoparticles in

base fluid (coolant) enhances the thermal conductivity of resultant fluid. Moreover, Nano particles exhibit significant stability, higher heat transfer capabilities and reduced particle clogging. The dispersion of nanoparticles enhances the heat transfer characteristics in base fluids because of thermal physical properties such as Thermal conductivity, Density, Viscosity, specific heat. Choi et al. [5] proposed the term nano-fluids by dispersing metallic or non-metallic particles in base fluids. From the literature, it is observed that nano-fluids possess enhanced thermo physical properties compared to conventional fluids.

Table 5-4: Thermophysical Properties of nano particles and LN_2

Properties	Thermal Conductivity (W/m-K)	Viscosity(μPa-s)	Specific Heat (J/kg-K)	Density (kg/m^3)
LN_2	0.1495	1169.96	2007.8	814.51
Al_2O_3	17.65	---------	525	3970
Fe_2O_3	20	-------	650	5250
CuO	18	---------	540	6510

5.4.2 *Solution Methodology*

Different mathematical correlations are used to investigate the thermophysical properties of mixed nano cryogenic coolants which are developed in the past. The feasibility study is carried by considering the assumptions such as the sphericity of nanoparticles as unity i.e., TiO_2 nano particles are spherical in shape and the average size of each nanoparticles is considered as 20nm.

The variation of thermo physical properties with respect to temperature for nanocryogenic coolants at equal compositions is plotted in the graph below. From the graph it is evidenced that the curve for density, viscosity, Thermal Conductivity decreases with the increase in temperature whereas, specific heat curve increases exponentially with the increase in temperature.

1) Viscosity

The need to determine the viscosity of nano cryogenic fluids is due to direct effect on pressure drop and pumping power. Hence, determination of viscosity is necessary to study the feasibility of nanocryogenic fluids.

By using Einstein model [102], viscosity of nanocryogenic fluids is determined

$$\frac{\mu_{eff}}{\mu_{ref}} = 1 + 2.5\phi$$

(70)

Where,

μ_{eff} = Effective viscosity of nanocryogenic fluid

μ_{ref} = Viscosity of nanocryogenic fluid

The nano dispersed nano cryogenic fluid viscosity is determined using Brinkman model as follows

$$\frac{\mu_{eff}}{\mu_{ref}} = \frac{1}{(1-\phi)^{2.5}} \quad (71)$$

Gherasim model for calculating viscosity is given as follows

$$\frac{\mu_{eff}}{\mu_{ref}} = 0.904e^{14.8\phi} \quad (72)$$

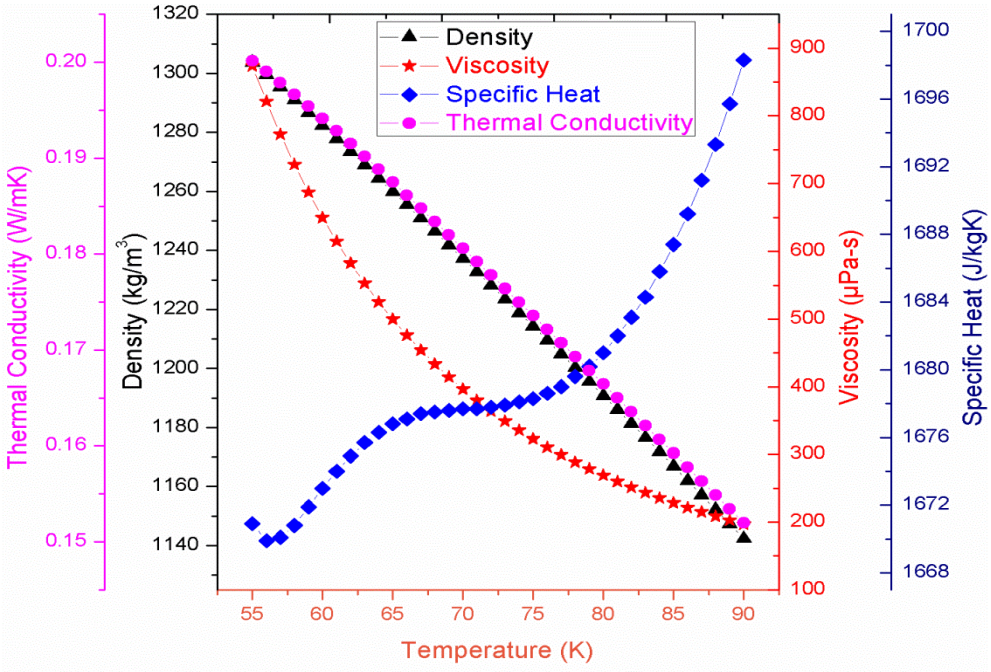

Figure 5-7: Temperature dependent thermo physical properties of LOx

Wang model of viscosity is given by

$$\frac{\mu_{eff}}{\mu_{ref}} = (1 + 7.3\phi + 123\phi^2) \quad (73)$$

Pak and Cho model of viscosity is used to determine the viscosity of nano cryogenic fluid

$$\mu_{eff} = 1 + 2.5\phi + 6.2\phi^2 \quad (74)$$

2) Density

The nanocryogenic fluid effective density can be calculated by using Xuan and Roetzel

$$\rho_{eff} = (1-\phi)\rho_{ref} + \phi\rho_{NP} \quad (75)$$

Where,

ρ_{eff} = Effective density of nanocryogenic fluid

ϕ = Volume concentration of the nanoparticles

ρ_{ref}, ρ_{NP} = Density of nanocryogenic fluid, nanoparticle

3) Thermal conductivity

The enhancement of heat transfer rate depends mainly on thermal conductivity of nanoparticle and cryogenic coolant used. Depending on overall thermal conductivity of nanocryogenic coolant heat transfer rate may vary. Moreover, thermal conductivity of conventional cryogenic coolants and nano cryogenic fluids are lower compared to the nano particles. For the heterogeneous mixture of nanoparticles in base cryogenic coolants, Maxwell proposed a model. The discontinuous and continuous phases of nano-mixture is used to determine these model.

The nanocryogenic fluid effective thermal conductivity can be determined using Maxwell relation

$$\frac{K_{eff}}{K_{ref}} = \frac{2K_{ref} + K_P + 2\phi(K_P - K_{ref})}{2K_{ref} + K_P - \phi(K_P - K_{ref})} \quad (76)$$

Where,

K_{eff} = Effective thermal conductivity of nano cryogenic fluid

K_P, K_{ref} = Thermal conductivity of nano cryogenic fluid, nano particle

By considering the sphericity, of nanoparticles, Hamilton and Crosser developed a model.

$$\frac{K_{eff}}{K_{ref}} = \frac{(n+1)K_{ref} + K_P - (n-1)\phi(K_{ref} - K_P)}{(n+1)K_{ref} + K_P + \phi(K_{ref} - K_P)} \quad (77)$$

Where,

n= shape factor = $\frac{3}{\psi}$

ψ = sphericity or non-spherical edge

An experimental correlation developed by Buongiorno model is used to determine Thermal conductivity as follows

$$\frac{K_{eff}}{K_{ref}} = 1 + 2.92\phi - 11.99\phi^2$$

(78)

The theory of effective medium dispersion in nano cryogenic fluid is given by Timofeeva model

$$\frac{K_{eff}}{K_{ref}} = (1 + 3\phi) \quad (79)$$

4) Specific heat

The Specific heat of nanocryogenic fluid is determined by using Pak and Cho model

$$(C_p)_{eff} = \frac{(1-\phi)(\rho C_P)_{ref} + \phi(\rho C_P)_{NP}}{(1-\phi)\rho_{ref} + \phi\rho_{NP}} \quad (80)$$

Where,

$(C_P)_{eff}$ = Effective specific heat of nano cryogenic fluid

$(C_P)_{ref}, (C_P)_{NP}$ = Specific heat of nano cryogenic fluid, nano particle

ρ_{ref}, ρ_{NP} = Density of nano cryogenic fluid, nano particle

5.5 Thermohydraulic Analysis of central channel

5.5.1 *Pressure Drop and Heat Transfer Analysis*

5.5.1.1 Pressure Drop (Smooth Pipe)

Step 1:

Find out the ***Thermophysical properties*** at operating conditions.

For the given cryogenic liquid (LN_2, LOX, LHe, LAr etc) the Thermophysical properties such as Density (ρ), Viscosity (μ), Specific heat (Cp) and Thermal conductivity (K) from the data given on the CYROGENIC Heat Transfer or from the NIST data.

Step 2:

Calculate the Mass flow rate per unit Cross section area

$$G = \frac{\dot{m}}{A_c} \tag{81}$$

Where, $\dot{m}$ is given gm/sec

$$A_c = \frac{\pi}{4} D^2 \tag{82}$$

Step 3:

Find out the Reynolds number (Re)

Reynolds number is given as the Inertia force (F=ma) to the Viscous force

$$\mathrm{Re} = \frac{inertia\ force}{viscous\ force} = \frac{DG}{\mu} \tag{83}$$

Where,

D= diameter of the pipe (m), given

G= mass flow rate per unit cross section area (kg/s*m^2), calculated above

μ= viscosity, taken from the data of NIST

Note:

Decide whether the flow is laminar or turbulent

If the Reynolds number Re is < 2300, it is Laminar flow

If the Reynolds number Re is > 2300, it is Turbulent flow

Step 4:

Calculate the friction factor (f)

Note: There is no direct formula for the friction factor. Depends on the Reynolds number choose the appropriate formula

Example:

For the laminar flow,

$$f = \frac{64}{\mathrm{Re}} \tag{84}$$

For the turbulent flow,

$$f = 0.25(0.82\log_{10}\mathrm{Re}_D - 1.64)^{-2} \tag{85}$$

Step 5:

Calculate the pressure drop (Δp)

$$\Delta p = \frac{fLG^2}{2D\rho} \tag{86}$$

Where,

f= friction factor, calculated above

L= length of the pipe, given in data

$$\text{Velocity } v = \frac{G\pi D^2}{4\rho A_c} \tag{87}$$

D= diameter of the pipe, G= mass flow rate per unit area cross section

5.5.1.2 Heat Transfer Rate (Smooth Pipe)

Step 1:

Calculate the Graetz number

$$Greatznumber = (\mathrm{Re})(\mathrm{Pr})(\frac{D}{L}) \tag{88}$$

Where, Pr= Prandtl number, taken from the data of Book

$$\mathrm{Pr} = \frac{convective\,heat\,transfer}{conductive\,heat\,transfer} = \frac{\mu Cp}{K} \tag{89}$$

Step 2:

Calculate the Nusselt number

$$Nu = \frac{hD}{K} \tag{90}$$

$Nu = 0.036(\mathrm{Re})^{0.8}(\mathrm{Pr})^{0.33}$, for turbulent flow (91)

$$Nu = 3.66 + \frac{0.0668(\frac{D}{L})\mathrm{Re}_D\,\mathrm{Pr}}{1 + 0.04((\frac{D}{L})(\mathrm{Re}_D)(\mathrm{Pr}))^{0.7}}\text{, for laminar flow} \tag{92}$$

Note: There is direct formula for the Nusselt number. Use the correlation by taking the Reynolds number into consideration.

Step 3:

Calculate the Heat transfer coefficient (h) from the Nusselt number

$$Nu = \frac{hD}{K} \Rightarrow h = \frac{Nu * K}{D} \tag{93}$$

Step 4:

Calculate the heat transfer through the pipe

$$Q = hA_s\Delta T \tag{94}$$

Where,

h= convective heat transfer coefficient in W/m^2K

Surface area $A_s = \Pi DL$ (95)

$\Delta T = T_{wall} - T_{fluid}$ (96)

5.5.1.3 Pressure Drop (Rough Pipe)

Step 1:

Find out the Thermophysical properties at operating conditions

For the given cryogenic liquid (LN_2, LOX, LHe, LAr etc) the Thermophysical properties such as Density (ρ), Viscosity (μ), Specific heat (Cp) and Thermal conductivity (K) from the data given on the CYROGENIC Heat Transfer or from the NIST data.

Step 2:

Calculate the Mass flow rate per unit Cross section area

$$G = \frac{\dot{m}}{A_c} \tag{97}$$

Where, $\dot{m}$ is given gm/sec

$$A_c = \frac{\pi}{4} D^2 \tag{98}$$

Step 3:

Find out the Reynolds number (Re)

Reynolds number is given as the Inertia force (F=ma) to the Viscous force

$$\mathrm{Re} = \frac{inertia\ force}{viscous\ force} = \frac{DG}{\mu} \tag{99}$$

Where,

D= diameter of the pipe, given

G= mass flow rate per unit cross section area, calculated above

μ= viscosity, taken from the data of NIST

Note:

Decide whether the flow is laminar or turbulent

If the Reynolds number Re is < 3500, it is Laminar flow

If the Reynolds number Re is > 3500, it is Turbulent flow

Step 4:

Here we need to decide whether the tube is rough-tube or smooth tube. We need to calculate (e/D) ratio because for a laminar flow the heat transfer coefficient is independent of the surface roughness; however for a turbulent flow the roughness will affect the heat transfer coefficient.

$(\frac{e}{D})\,\mathrm{Re} > 5$, tube is a rough-tube

$(\frac{e}{D})\,\mathrm{Re} < 5$, tube is a smooth pipe

Step 5:

Calculate the friction factor (f)

Case 1:

For a rough-tube

The friction factor for the rough tube is found out by the following correlation given by Round in 1980

$$\frac{1}{f^{0.5}} = 0.782 \ln[\frac{1}{0.135(\frac{e}{D}) + (\frac{6.5}{\mathrm{Re}})}] \qquad (100)$$

$$f = \frac{1.325}{[\ln(\frac{e}{3.7D} + \frac{5.74}{\mathrm{Re}^{0.9}})]^2}\ ;\ 10^{-6} \le \mathrm{e/D} < 10^{-2};\ 5000 < \mathrm{Re} < 10^{8} \qquad (101)$$

Case 2:

For a smooth-tube

Follow the steps which are given for the smooth tube

Step 6:

Calculate the pressure drop (ΔP)

$$\Delta p = \frac{fLG^2}{2D\rho} \qquad (102)$$

5.5.1.4 Heat Transfer Rate (Rough Pipe)

Step 1:

Calculate the convective heat transfer coefficient

For a rough tube the heat transfer coefficient is given by the correlations

1) Gnielinski correlation developed in 1976

$$\frac{8j_H}{f} = \frac{[1-(1000/\mathrm{Re})]\mathrm{Pr}^{0.67}}{1+1.27(f/8)^{0.5}(\mathrm{Pr}^{0.67}-1)} \tag{103}$$

2) Colburn J-factor for heat transfer

$$j_H = \frac{h_c \mathrm{Pr}^{0.67}}{C_p \rho V_{avg}} = \frac{h_c \mathrm{Pr}^{0.67}}{C_p G} \tag{104}$$

Step 2:

Calculate the Nusselt number

The Nusselt number is given by the Colburn J-factor for heat transfer as

$$j_H = \frac{Nu}{\mathrm{Re}*\mathrm{Pr}^{0.33}} \tag{105}$$

Step 3:

Calculate the heat transfer rate

$$Q = h_c A_w (T_w - T_{avg}) \tag{106}$$

Where, Area of the surface of the tube $A_w = \prod DL$

5.5.2 *Pressure Drop and Heat Transfer Analysis Using CFD*

5.5.2.1 Pressure Drop Analysis

Step 1:

Calculation of friction factor

$$f = \frac{8\tau_{wall}}{\rho v_{avg}^{\ 2}} \tag{107}$$

Where,

F= friction factor.

τ_{wall} = shear stress at the wall.

ρ = density of the cryocoolant (kg/m^3).

v_{avg} =average velocity of the cryogenic fluid (m/s).

Step 2:

Calculation of Reynolds number

$$\mathrm{Re} = \frac{D_h v_{avg} \rho}{\mu} \tag{108}$$

Where,

Re= Reynolds number.

D_h = hydraulic diameter.

v_{avg} =average velocity of the cryogenic fluid.

ρ = density of the cryocoolant (kg/m^3).

μ= viscosity of the cryogenic fluid.

Step 3:

Calculation of pressure drop

$$\Delta p = \frac{\rho f L v_{avg}^{\ 2}}{2 D_h} \tag{109}$$

Where,

f= friction factor, calculated above

L= length of the corrugated pipe

D_h = hydraulic diameter.

v_{avg} =average velocity of the cryogenic fluid (m/s).

ρ = density of the cryocoolant.

Step 4:

Calculation of pumping power

$$W = \Delta p \dot{V} \quad (110)$$

Where,

Δp = pressure drop (Pa)

$\dot{V}$ = volume flow rate

$$\dot{V} = A * v_{avg} \text{ (Lit/min)} \quad (111)$$

A= area of cross section in m^2

v_{avg} =average velocity of the cryogenic fluid (m/s)

5.5.2.2 Heat Transfer Analysis

Step 1:

Calculate Nusselt number

$$Nu = \frac{h_c L}{k} \quad (112)$$

Where,

h_c= heat transfer coefficient(W/m^2-K)

K= thermal conductivity (W/m-K)

Step 2:

Unknown heat transfer coefficient can be calculated as follow

$$q'' = h_c \Delta T \quad (113)$$

Where,

q"= heat flux (W/m^2)

$\Delta T = T_{wall} - T_{bulk}$, temperature difference in K (114)

Step 3:

Cooling capacity of the cryogenic coolant is given by

$$Q = \dot{v}\,\rho C_P (T_{outlet} - T_{inlet}) \qquad (115)$$

C_p = specific heat

T_{outlet}, T_{inlet} are temperatures of cryogenic coolant in K.

The complete solution methodology is shown in Figure 5-8.

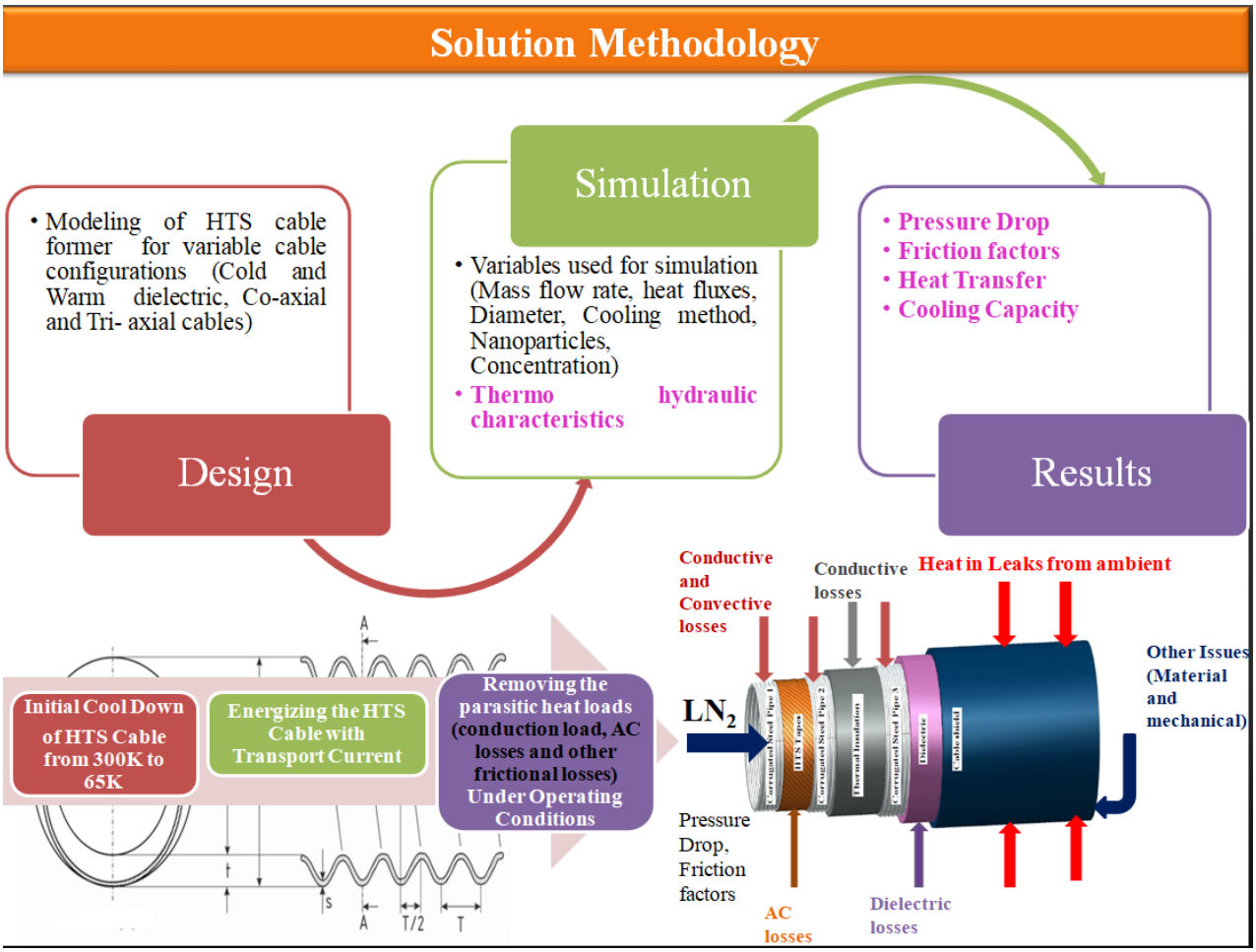

Figure 5-8: Solution Methodology for Thermohydraulic Analysis

5.6 Governing Equations

5.6.1 *Governing Equations used for solving the Thermohydraulic characteristics in SMES using LO_X as cryogenic coolant*

The governing equations for conservation of mass, momentum and energy valid for incompressible and steady flow through corrugated former of HTS cable are discussed in

this section. Since the flow through corrugated former of HTS cable is turbulent, the time averaged Reynolds Averaged Navier-Stokes (RANS) equations are implemented. These equations are discritized and solved using Finite Volume Method (FVM). Further, the realizable $\kappa-\varepsilon$ turbulence scheme is employed in the ANSYS-FLUENT as closure to the RANS governing equations. The numerical results obtained from the pressure fields, velocity fields and temperature distribution in the corrugated former are used for calculating the thermohydraulic performance of HTS cable. The following assumptions are considered for developing the mathematical model of the present analysis are the flow of SCN through HTS cable is steady and incompressible, mass transfer, gravitational and radiation heat transfer are negligible because single phase forced flow of SCN through the proper insulated (dielectric materials, multilayered insulation as well as vacuum sealed) HTS cable.

The time averaged conservation of mass applicable for flow of SCN through corrugated former in HTS cable can be written as [103], [104]

$$\nabla\bullet \qquad {}_{r}\,\bar{\mathbf{u}}\big)=0 \tag{116}$$

where, $\bar{\mathbf{u}}$ is the time averaged velocity vector and $\rho(T)_{SCN}$ is temperature dependent density of SCN.

The time averaged conservation of momentum equation for flow of SCN through corrugated former in HTS cable can be written as [103], [104]

$$\nabla\bullet \qquad\qquad\qquad \bullet \tag{117}$$

$\bar{P}$ is time averaged pressure of SCN in the computational domain, $\mathbf{u}'$ is fluctuating component of velocity vector, $\mu(T)_{SCN}$ is temperature dependent viscosity of SCN.

The time averaged conservation of energy equation for flow of SCN through corrugated former in HTS cable can be written as [103], [104]

$$\nabla\bullet \qquad\qquad \bullet \qquad\qquad \bullet \tag{118}$$

where, $\bar{\boldsymbol{\psi}}$ is the time averaged component of mean flow property, $\boldsymbol{\psi}'$ is fluctuation in flow property and $k(T)$ is temperature dependent thermal conductivity of SCN.

For internal flows, an intensive verification is done on the applicability of $\kappa-\varepsilon$ model and strongly recommended because of high accuracy in computational solution [105]. Hence, the realizable $\kappa-\varepsilon$ turbulent scheme with standard wall function is adapted for estimating the thermohydraulic performance in HTS SMES. The time averaged turbulent transport equations for Turbulence kinetic energy (TKE) and Turbulence dissipation rate (TDR) can be written as [106]

$$\nabla\bullet \left[\left(\frac{(T)_{SCN}}{\sigma_k} \right) \nabla\kappa \right] + 2\mu_t(T)_{SCN}\,\bar{e}_{ij}\bar{e}_{ij} - \rho(T)_{SCN}\,\varepsilon \tag{119}$$

$$\nabla\bullet \left[\left(\frac{(T)_{SCN}}{\sigma_\varepsilon} \right) \nabla\varepsilon \right] - C_{2-\varepsilon}\rho(T)_{SCN}\frac{\varepsilon^2}{\kappa\sqrt{v(T)\varepsilon}} \tag{120}$$

where, κ is Turbulent kinetic energy (m^2/s^2), $\kappa = \overline{u'^2}/2$, $\mu_t(T)_{SCN}$ is turbulent viscosity of SCN, $\mu_t(T)_{SCN} = \rho(T)_{SCN} C_\mu \left(\kappa^2/\varepsilon\right)$, σ_k is turbulent kinetic energy (TKE) Prandtl number (σ_k=1), $\bar{e}_{ij}$ is steady mean rate of deformation, e'_{ij} is fluctuating component of rate of deformation and ε is dissipation rate per unit mass, $\varepsilon = 2v\overline{e'_{ij}.e'_{ij}}$, σ_ε is turbulent dissipation rate (TDR) Prandtl number (σ_ε=1.2), $v(T)$ is temperature dependent kinematic viscosity, $v(T) = \mu(T)/\rho(T)$ and the constants used for the analysis are $C_{2-\varepsilon} = 1.9$, Energy Prandtl number = 0.85, Wall Prandtl number = 0.85.

5.6.2 *Governing Equations used for solving the Thermohydraulic characteristics in SMES using LN_2 as cryogenic coolant*

The steady, incompressible time averaged Reynolds Averaged Navier-Stokes (RANS) equations applicable to flow through HTS SMES central channel are as follows.

The continuity equation for flow of LN_2 through HTS SMES central channel can be represented as [103], [107], [108]

$$div\left(\bar{\mathbf{u}}\right) = 0 \tag{121}$$

where, $\bar{\mathbf{u}}$ is the time averaged velocity vector.

The conservation of momentum equation applicable to flow through HTS SMES central channel with is given by [103], [107], [108]

x momentum

$$\rho(T)\left(div\left(\bar{u}\bar{\mathbf{u}}\right)\right)=-\frac{\partial\bar{p}}{\partial x}+\mu(T)\,div\,grad\,\bar{u}+\rho(T)\left[-\frac{\partial\overline{u'^2}}{\partial x}-\frac{\partial\overline{u'v'}}{\partial y}-\frac{\partial\overline{u'w'}}{\partial z}\right] \quad (122)$$

y momentum

$$\rho(T)\left(div\left(\bar{v}\bar{\mathbf{u}}\right)\right)=-\frac{\partial\bar{p}}{\partial y}+\mu(T)\,div\,grad\,\bar{v}+\rho(T)\left[-\frac{\partial\overline{u'v'}}{\partial x}-\frac{\partial\overline{v'^2}}{\partial y}-\frac{\partial\overline{v'w'}}{\partial z}\right] \quad (123)$$

z momentum

$$\rho(T)\left(div\left(\bar{w}\bar{\mathbf{u}}\right)\right)=-\frac{\partial\bar{p}}{\partial z}+\mu(T)\,div\,grad\,\bar{u}+\rho(T)\left[-\frac{\partial\overline{u'w'}}{\partial x}-\frac{\partial\overline{v'w'}}{\partial y}-\frac{\partial\overline{w'^2}}{\partial z}\right] \quad (124)$$

$\bar{p}$ is time averaged pressure, $\bar{u}$, $\bar{v}$, $\bar{w}$ are time averaged components of velocity in x, y and z directions respectively, u', v', w' are fluctuating component of velocity in x, y and z, $\mu(T)$ is temperature dependent viscosity of LN_2 and $\rho(T)$ is temperature dependent density of LN_2. In equation (117), (123) and (124) the first term on the right hand side represents pressure gradient, second term represents viscous stress and the last term represents turbulent shear stress respectively. The turbulent or Reynolds stresses are given by $\tau_{ij}=\mu_t(T)\left(\frac{\partial\bar{u}}{\partial y}+\frac{\partial\bar{v}}{\partial x}\right)$ and $\mu_t(T)$ represents eddy viscosity

The conservation of energy equation for internally forced flow of LN_2 through HTS SMES central channel is given by [103], [107], [108]

$$div\left(\Phi\bar{\mathbf{u}}\right)=div\left(k(T)\,grad\,\Phi\right)+\left[-\frac{\partial\overline{u'\psi'}}{\partial x}-\frac{\partial\overline{v'\psi'}}{\partial y}-\frac{\partial\overline{w'\psi'}}{\partial z}\right] \quad (125)$$

where, Φ is the time averaged component of mean flow property, ψ' is fluctuation in flow property and $k(T)$ is temperature dependent thermal conductivity of LN_2.

The $\kappa-\varepsilon$ model used for estimating the thermohydraulic performance of HTS SMES central channel can be written as [106]

Turbulence kinetic energy (TKE)

$$div\left(\rho(T)\kappa\bar{\mathbf{u}}\right)=div\left[\frac{\mu_t(T)}{\sigma_k}grad\kappa\right]+2\mu_t(T)\bar{e}_{ij}\cdot\bar{e}_{ij}-\rho(T)\varepsilon \quad (126)$$

where, κ is Turbulent kinetic energy (m^2/s^2), $\kappa=\overline{u'^2}/2$, $\mu_t(T)$ is turbulent viscosity, $\mu_t(T)=\rho(T)C_\mu\left(\kappa^2/\varepsilon\right)$, σ_k is turbulent kinetic energy (TKE) Prandtl number, $\bar{e}_{ij}$ is steady mean rate of deformation, e'_{ij} is fluctuating component of rate of deformation and ε is dissipation rate per unit mass, $\varepsilon=2v\overline{e'_{ij}.e'_{ij}}$

Turbulence dissipation rate (TDR)

$$div\left(\rho(T)\varepsilon\bar{\mathbf{u}}\right)=div\left[\frac{\mu_t(T)}{\sigma_\varepsilon}grad\varepsilon\right]+C_{1-\varepsilon}\frac{\varepsilon}{\kappa}2\mu_t(T)\bar{e}_{ij}\cdot\bar{e}_{ij}-C_{2-\varepsilon}\rho(T)\frac{\varepsilon^2}{\kappa} \quad (127)$$

where, σ_ε is turbulent dissipation rate (TDR) Prandtl number, the standard wall function constants used for the analysis are $C_\mu=0.09$, $C_{1-\varepsilon}=1.44$, $C_{2-\varepsilon}=1.92$, σ_k=1 and σ_ε=1.3

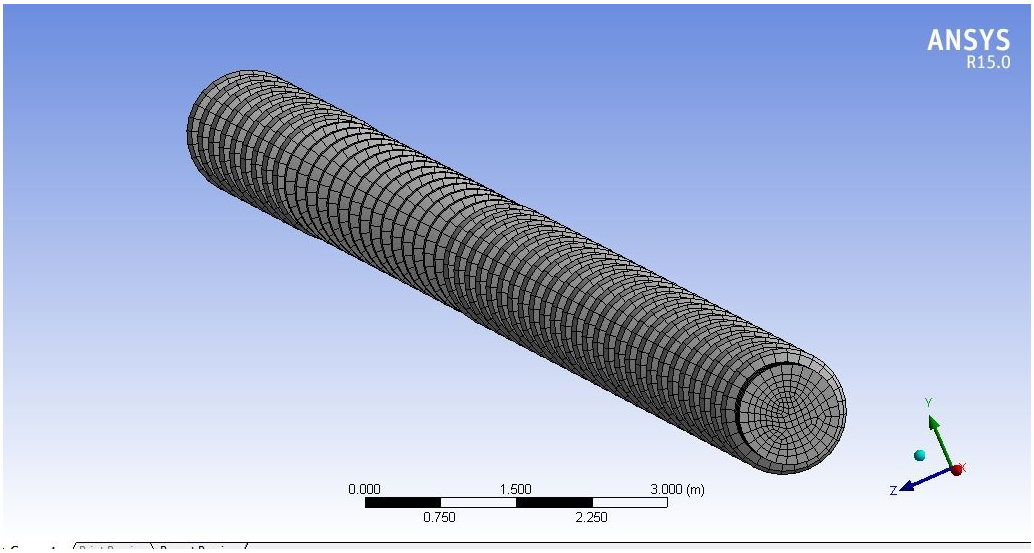

Figure 5-9: Mesh topology of central channel for SMES

5.6.3 *Assumptions*

For investigating the thermohydraulic characteristics of SMES with mesh topology is shown in Figure 5-9 and the following assumptions were taken into account

- The flow of is in steady-state condition and the thermal and hydraulic boundary layer are fully developed
- LN_2 enters the HTS cable with a uniform bulk temperature

- AC losses from HTS tapes and heat-in-leak from surrounding are imposed as uniformly distributed heat flux on the wall of the corrugated pipe. Moreover, these thermal losses are assumed to be solely absorbed by the corrugated pipe, and no heat loss is present at the terminations of HTS cable system
- Effect of gravitational forces LN_2 flow is considered to be negligible as a consequence of forced-flow phenomenon in the corrugated pipe

5.7 Results and Discussions

5.7.1 *Thermohydraulic analysis with SCN as cryogenic coolant*

The methodology used for investigating the thermohydraulic performance with SCN flow through corrugated former of HTS SMES is presented. The computational geometry is modeled, meshed and the boundary conditions applicable for the computation of HTS cable are applied. Later, results of the closure problem are obtained by solving the governing equations such as conservation of mass, momentum and energy with imposed boundary conditions in ANSYS-FLUENT. Different heat loads due to heat intrusions and AC losses ranging from 1 W/m to 3 W/m (0.8 W/m^2 to 1.2 W/m^2) are uniformly distributed over the computational domain, flow rate ranging from 5 L/min to 9 L/min (0.02 kg/sec to 0.024 kg/sec) are used and the results obtained.

5.7.1.1 Hydraulic Analysis

1) Variation of friction factor with Reynolds number

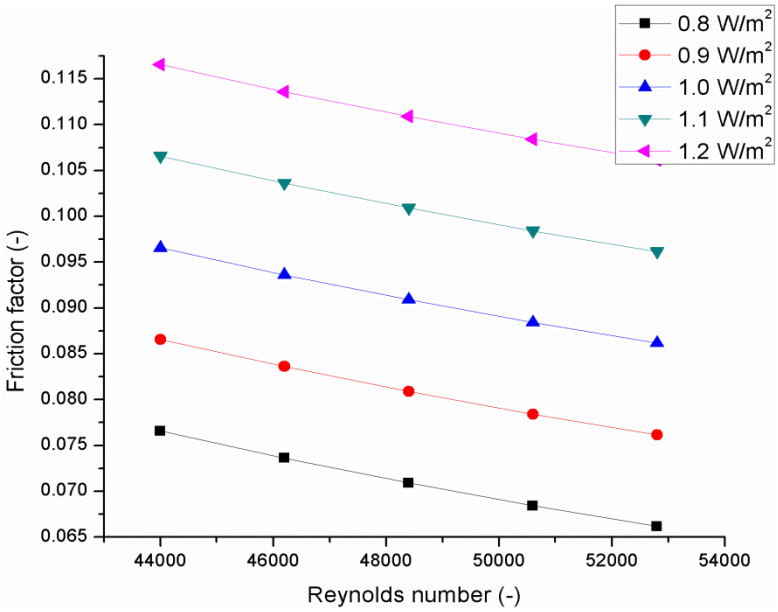

Figure 5-10: Variation of friction factor with Reynolds number

When the cryogenic fluid (SCN) is sent through the corrugation domain ***shear stresses*** are developed between the walls of the former and cryogenic fluid and between the layers of the fluid because of the friction. Hence, friction factor should be considered. The variation of Reynolds number for different friction factors with flow of SCN through corrugated former shown in Figure 5-10. By varying the heat fluxes from 0.8W/m^2 to 1.2W/m^2 friction factor is calculated for various mass flow rates 5 L/min to 9 L/min. It is observed that the flow is turbulent and varies from 44,000 to 54,000 and when the Reynolds number increases gradually friction factor also decreases. It is found that at 1.2W/m^2, friction factor is high. Higher the mass flow rate and heat flux higher the friction developed.

2) Variation of pumping power with mass flow rate

The variations of the pumping power for different mass flow rates are shown in Figure 5-11. From the figure, it is evident that for triangular domain pumping power is high and lower for the circular domain. This is due to the higher frictional force and the drag on the corrugated domain walls. Hence more power is required to pump the SCN thorough out the corrugation domain. Figure 5-11 shows the variation of the pumping power with respect to the mass flow rate. By varying the heat fluxes from 0.8W/m^2 to 1.2W/m^2 pumping power is calculated for various mass flow rates 5 L/min to 9 L/min. It is observed that the pumping power required increases with the mass flow rate. Higher the mass flow rate and heat flux higher the pumping power required to pump the SCN through the computational domain.

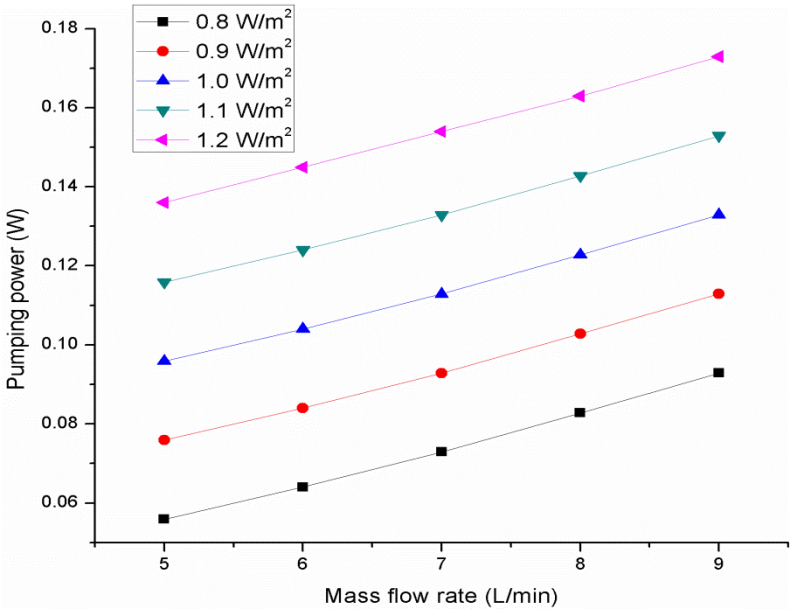

Figure 5-11: Variation of Pumping power with mass flow rate

5.7.1.2 Heat Transfer Analysis

1) Temperature Distribution

The variation of the temperature difference at different flow rates are shown in Figure 5-12. From the results it is proved that SCN is having the lesser temperatures between the inlet and outlet of the corrugated pipe. Hence, it can be used for long cooling of HTS SMES. The results are validated with the analytical analysis done by Dondapati et al [109] and experimental analysis done by Ivanov et al [110] by using Liquid Nitrogen (LN_2) as a cryocoolant.

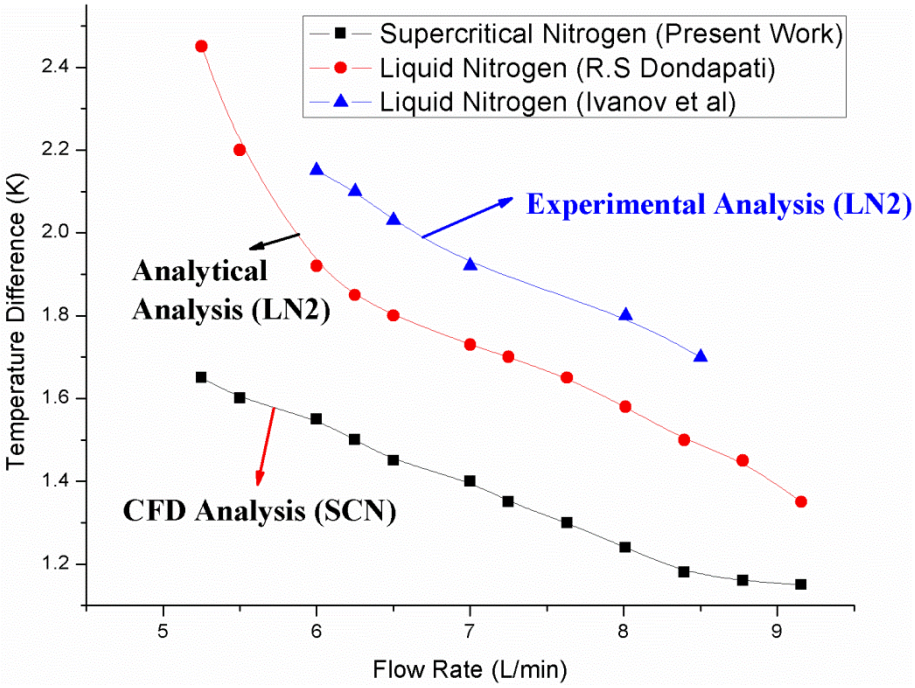

Figure 5-12: Temperature difference profile for computational analysis.

2) Variation of Nusselt number with Reynolds number

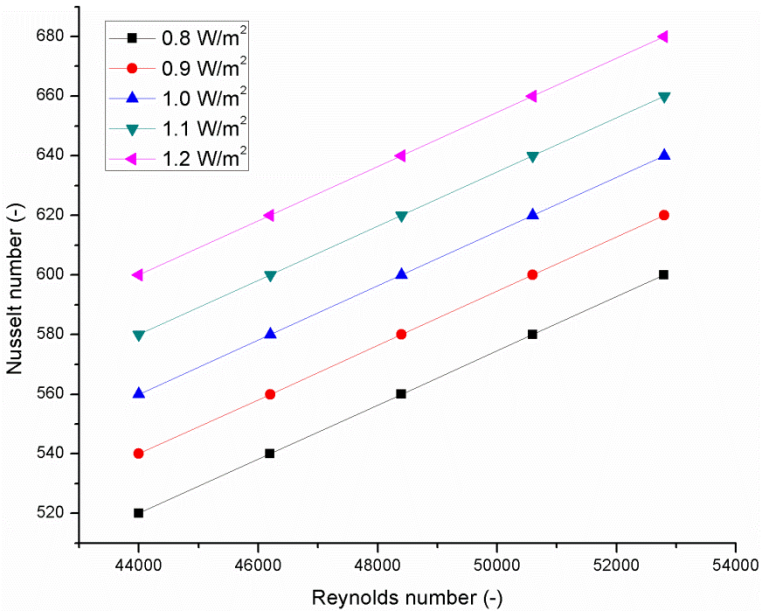

Figure 5-13: Variation of Nusselt number with Reynolds number

The relation between the fluid characteristics and the heat transfer characteristics is given by the Nusselt number as the function of Reynolds number. Nusselt number and the Reynolds number are directly related to each other. If Nusselt number increases Reynolds number will increase accordingly. Smooth pipes are having laminar flow and the heat developed due to the flow by shear is less. Smooth pipe is having less pressure drop when compared with the corrugated pipe. The present work aims to investigate the necessity of using the corrugated former with different corrugations. The advantage with the corrugated pipe is it will enhance the heat transfer rate and even decreases the stresses due to bending of the cable.

Figure 5-13 shows the variation of the Nusselt number with respect to the Reynolds number. By varying the heat fluxes from $0.8W/m^2$ to $1.2W/m^2$ Nusselt number is calculated for various mass flow rates 5 L/min to 9 L/min. It is observed that the Nusselt number increases ***slightly*** with the mass flow rate.

3) Variation of cooling capacity with mass flow rate

Superconductivity depends on the Critical current (I_C), Critical magnetic field (B_C) and Critical temperature (T_C). If the temperature of the HTS tape increase because of the transport current and magnetic field the conductor acts as a normal conductor. In order to retain superconductivity of the HTS tape it should be cooled below to its critical temperature. Hence, cooling capacity of the cable is necessary to investigate with

cryogenic coolant i.e., SCN. Figure 5-14 shows the variation of the heat fluxes from 0.8W/m^2 to 1.2W/m^2 for various mass flow rates 5 L/min to 9 L/min. The irregularities in the computational domain are due to the higher eddies produced at the corrugations of the geometry.

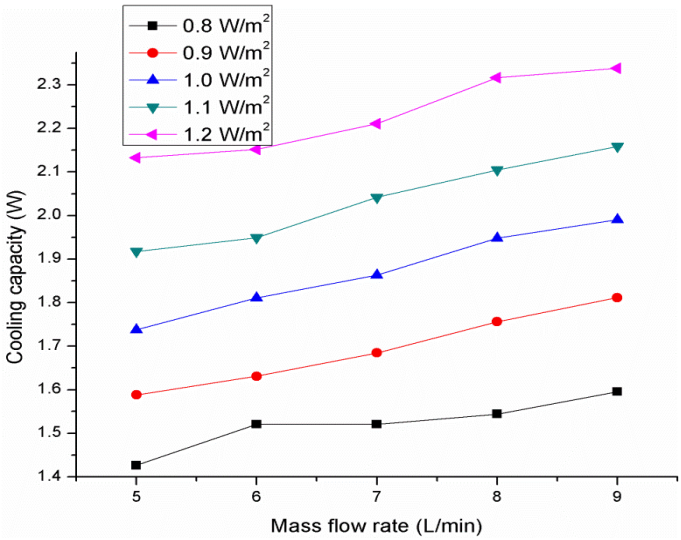

Figure 5-14: Variation of Cooling capacity with mass flow rate

5.7.2 *Thermohydraulic analysis with LN_2 as cryogenic coolant*

5.7.2.1 Hydraulic characteristics

1) Variation of friction factor with Reynolds number

When the cryogenic fluid (LN2) is sent through the corrugation domain ***shear stresses*** are developed between the walls of the former and cryogenic fluid and between the layers of the fluid because of the friction. Hence, friction factor should be considered. The variation of Reynolds number for different friction factors with flow of LN2 through corrugated former shown in Figure 5-15. By varying the heat loads from 1 W/m to 3 W/m friction factor is calculated for various mass flow rates 11 L/min to 20 L/min. It is observed that, when the Reynolds number increases gradually friction factor also decreases. It is found that at 3 W/m, friction factor is high. Higher the mass flow rate and heat flux higher the friction developed.

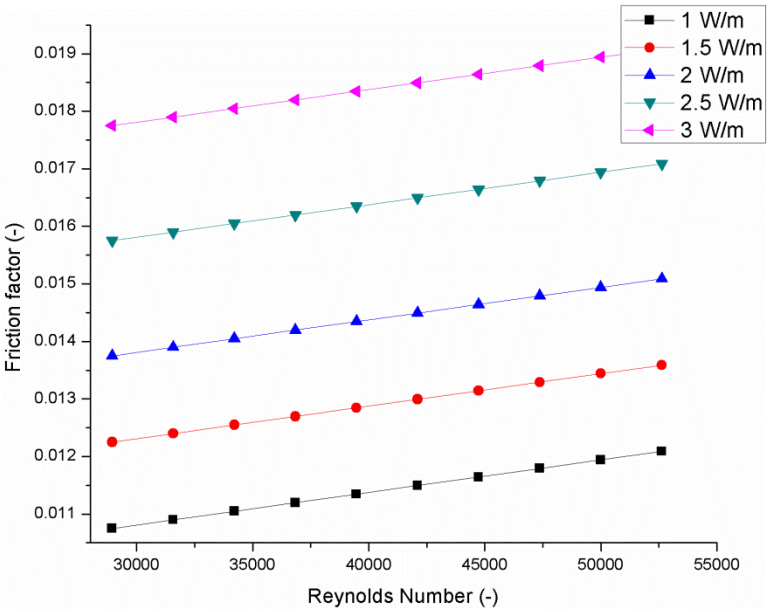

Figure 5-15: Variation of friction factor with Reynolds number

2) Pumping power

The variations of the pumping power for different mass flow rates are shown in Figure 5-11. From the figure, it is evident that for triangular domain pumping power is high and lower for the circular domain. This is due to the ***higher frictional force and the drag on the corrugated domain walls***. Hence more power is required to pump the LN2 thorough out the corrugation domain. Figure 5-16shows the variation of the pumping power with respect to the mass flow rate. By varying the heat loads from 1 W/m to 3 W/m pumping power is calculated for various mass flow rates 11 L/min to 20 L/min. It is observed that the pumping power required increases with the mass flow rate. Higher the mass flow rate and heat flux higher the pumping power required to pump the LN2 through the computational domain.

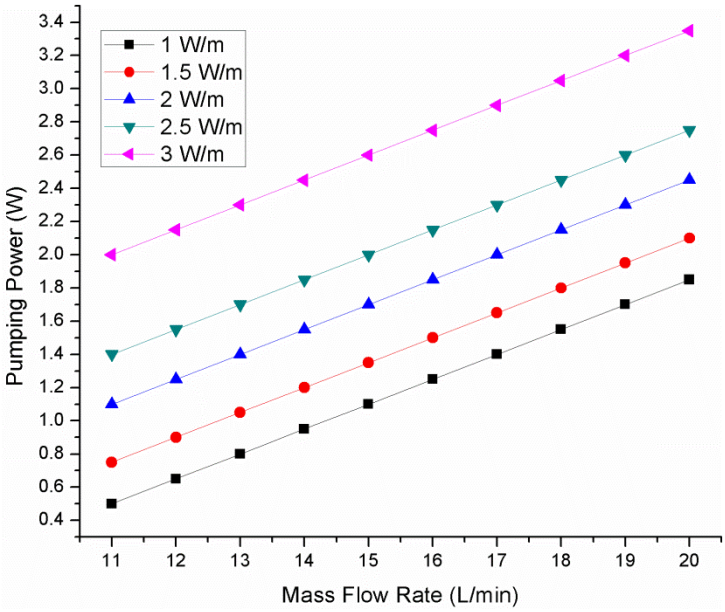

Figure 5-16: Variation of Pumping power with mass flow rate

5.7.3 *Thermal characteristics*

1) Temperature Distribution

The variation of the temperature difference at different flow rates are shown in Figure 5-17. From the results it is proved that LN2 is having the lesser temperatures between the inlet and outlet of the corrugated pipe. Hence, it ***can be used for long cooling of HTS SMES***. The results are validated with the analytical analysis done by Dondapati et al [109] and experimental analysis done by Ivanov et al [110] by using Liquid Nitrogen (LN_2) as a cryocoolant.

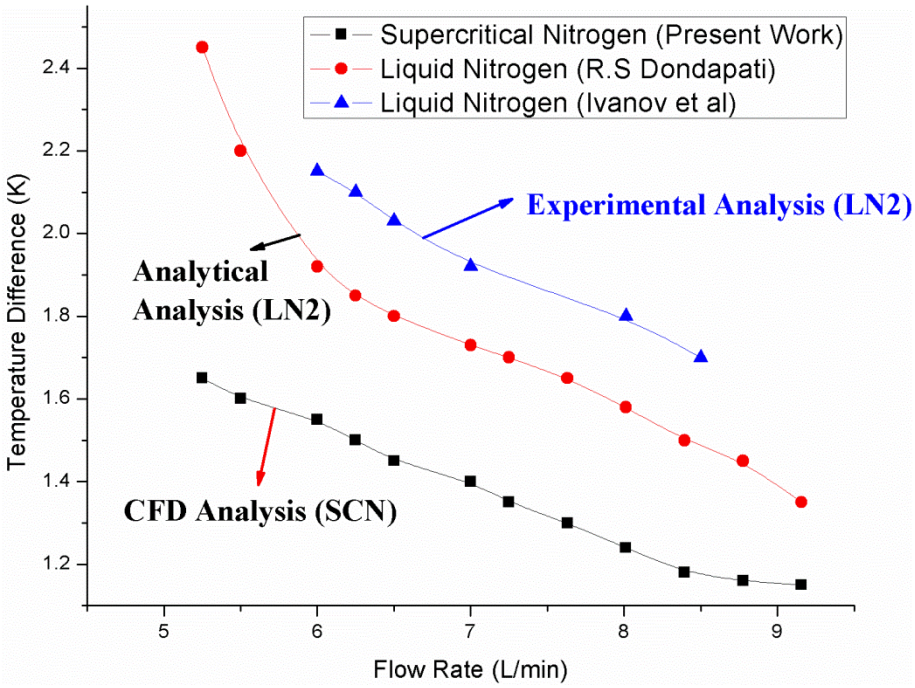

Figure 5-17: Temperature difference profile for computational analysis

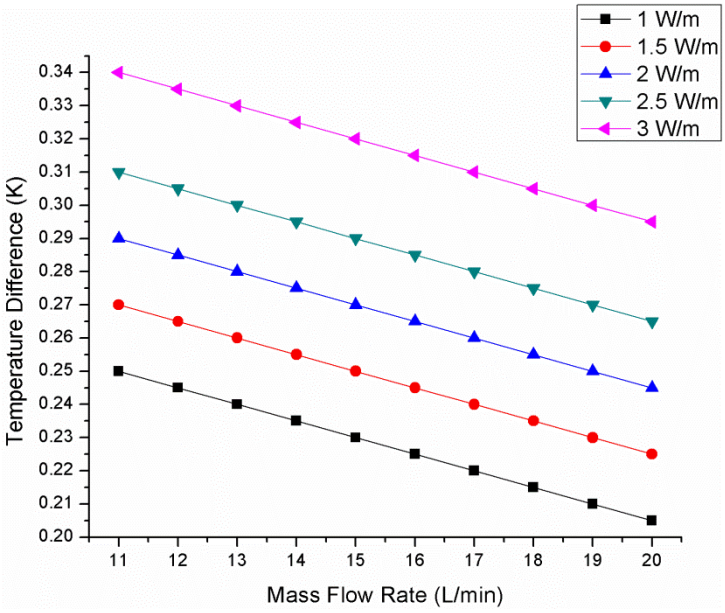

Figure 5-18: Temperature difference between the outlet and inlet of the computational domain

The temperature difference between the outlet and inlet temperature of central channel of computational domain is shown in Figure 5-18. From the figure, it is observed that at a constant heat load with the increase in flow rate temperature difference is decreased. The lower temperature difference signifies that the distance between the termination of HTS SMES can be increased and the installation cost of cryogenic cooling station can be reduced. Further, at a particular flow rate higher the heat load higher will be temperature difference.

2) Nusselt number

The relation between the fluid characteristics and the heat transfer characteristics is given by the Nusselt number as the function of Reynolds number. Nusselt number and the Reynolds number are directly related to each other. If Nusselt number increases Reynolds number will increase accordingly. Smooth pipes are having laminar flow and the heat developed due to the flow by shear is less. Smooth pipe is having less pressure drop when compared with the corrugated pipe. The present work aims to investigate the necessity of using the corrugated former with different corrugations. The advantage with the corrugated pipe is it will ***enhance the heat transfer rate*** and even ***decreases the stresses due to bending of the cable***.

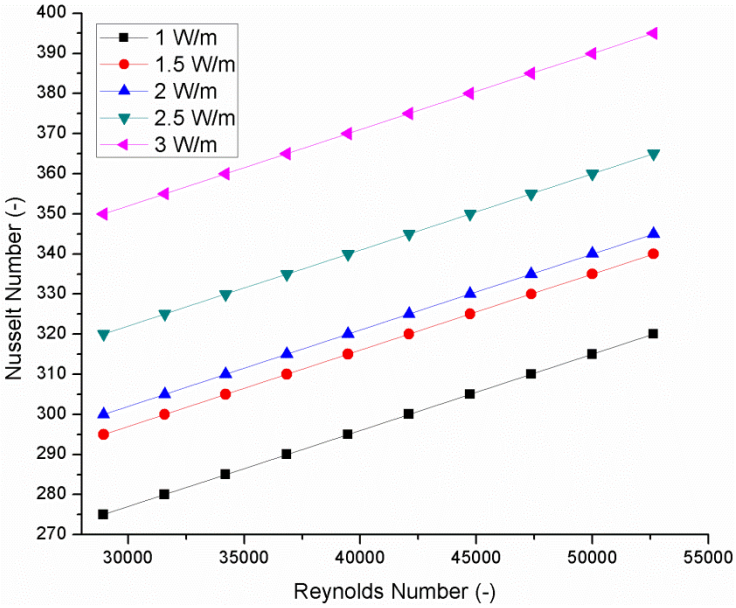

Figure 5-19: Variation of Nusselt number with Reynolds number

Figure 5-19 shows the variation of the Nusselt number with respect to the Reynolds number. By varying the heat loads from 1 W/m to 3 W/m. Nusselt number is calculated for various mass flow rates 11 L/min to 20 L/min. It is observed that the Nusselt number increases ***slightly*** with the mass flow rate.

3) Cooling capacity

Superconductivity depends on the Critical current (I_C), Critical magnetic field (B_C) and Critical temperature (T_C). If the temperature of the HTS tape increase because of the transport current and magnetic field the conductor acts as a normal conductor. In order to retain superconductivity of the HTS tape it should be cooled below to its critical temperature. Hence, cooling capacity of the cable is necessary to investigate with

cryogenic coolant i.e., LN2. Figure 5-21 shows the variation of the heat loads from 1 W/m to 3 W/m for various mass flow rate of 11 L/min to 20 L/min. The irregularities in the computational domain are due to the higher eddies produced at the corrugations of the geometry.

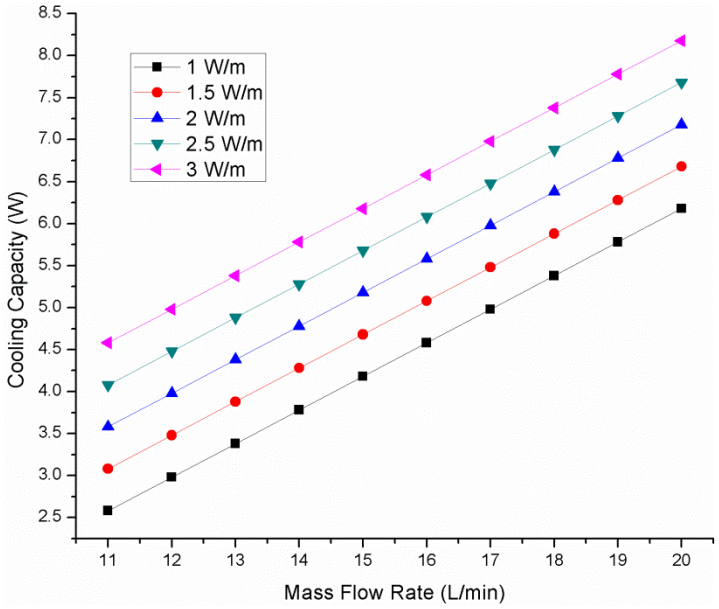

Figure 5-20: Variation of Cooling capacity with mass flow rate

5.7.4 *Estimation of thermophysical characteristics of Novel cryogenic coolant with dispersion of nano particles for cooling SMES*

5.7.4.1 Thermophysical properties with variation in volume concentration of different nano particle dispersion in Liquid Oxygen (LOx)

1) Density

The variation of density as a function of temperature with volume dispersion of TiO_2 nano particle in LO_X is shown in Figure 5-21. From the figure, it is observed that the effective density of nano cryogenic coolant with dispersion of nano particle shows higher density compared to LO_X at particular temperature. Further at a particular volume dispersion of nano particle, increase in temperature of cryogenic coolant the effective density of nano cryogenic coolant will decreases.

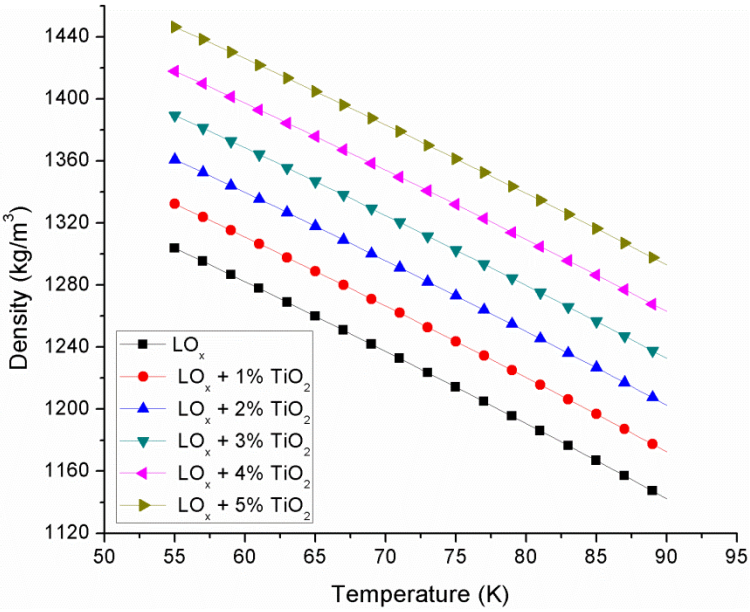

Figure 5-21: variation of effective Density with respect to temperature at different concentration

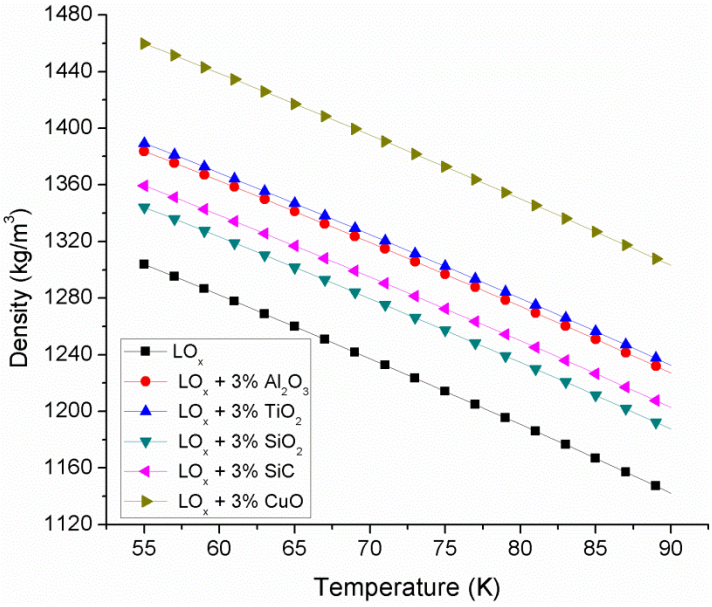

Figure 5-22: Variation of effective density with respect to Volume concentration at 3 % for different nano particles

Figure 5-22 represents the effective density of nano cryogenic coolant for dispersion of different nano particles at 3 % volume concentration. From the figure, it is observed at a particular temperature, the effective density of nano cryogenic fluid with dispersion of 3 % volume concentration of CuO nano particles increases the effective density approximately by 13 %. Further, for particular nano fluid increase in temperature of the nano cryogenic coolant, the effective density decreases.

Figure 5-23 shows the effective density of nano cryogenic coolant at various volume concentration of different nano particles at a cryogenic temperature of 73 K. From the figure, it can be seen that at particular volume concentration of nano particles, the effective density of the CuO nano cryogenic coolant is higher compared to other nano cryogenic coolants. Further, for a particular nano cryogenic coolant, increase in the volume concentration of nano particle increases the effective density.

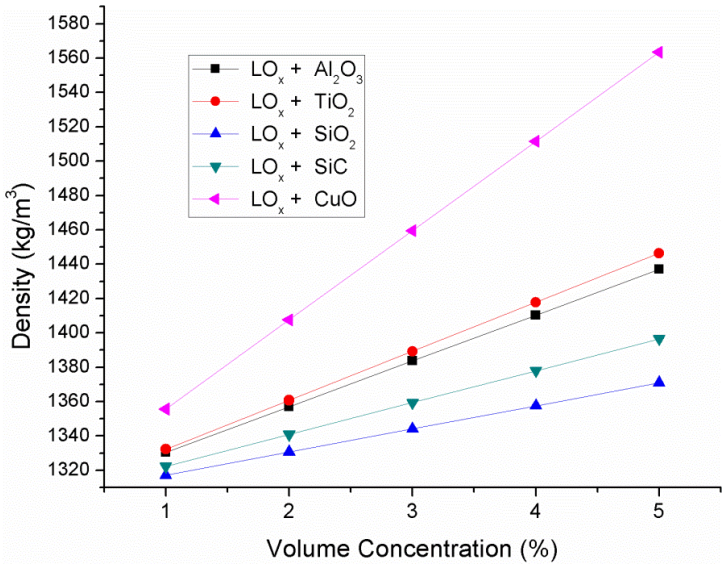

Figure 5-23: Variation of effective Density with respect to different volume concentration and nano particles at Liquid Oxygen temperature of 73 K

2) Specific Heat

Figure 5-24 represents the Specific Heat as a function of temperature for TiO_2 nano particle at different volume concentrations and temperature range of 55 K to 90 K. From the figure, it can be concluded that, at a particular temperature the specific heat of cryogenic coolant shows higher specific heat compared to dispersion of nano particle in cryogenic coolant. Further, at a particular volume concentration of TiO_2 nano particle, it can be seen that with increase in temperature the specific heat of the nano cryogenic coolant increases.

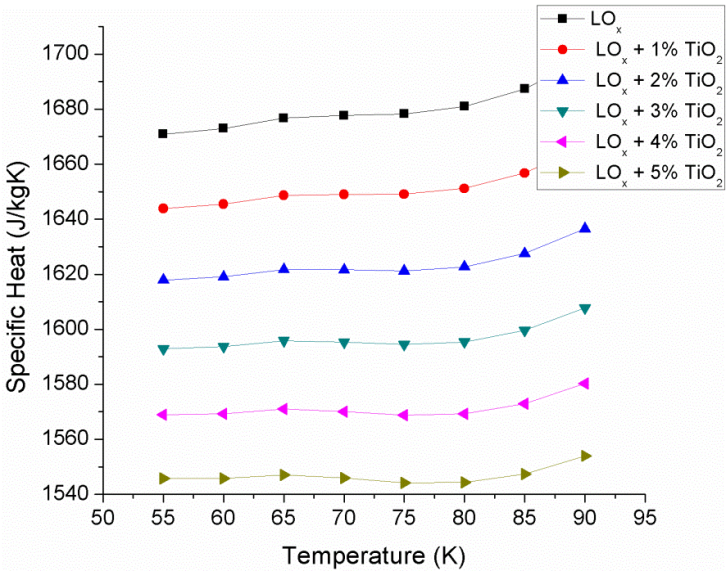

Figure 5-24: Variation of Specific Heat with respect to Temperature for different nano particles

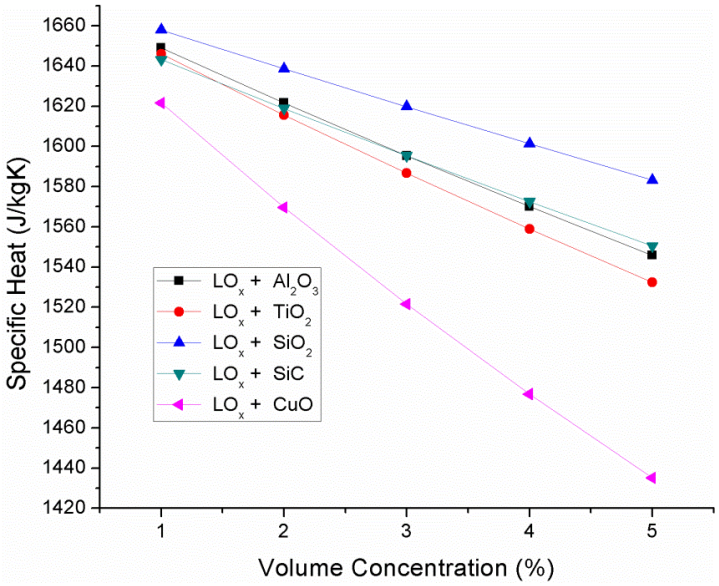

Figure 5-25: Variation of Specific Heat with respect to volume concentration for different nano particles

The variation of Specific Heat as a function of volume concentration at a temperature of 73 K is shown in Figure 5-25. From the figure, it is observed that lower the volume concentration of the nanoparticles in cryogenic coolant, higher the specific heat of the nano cryogenic coolant. Further, at particular volume concentration, higher specific heat of the nano cryogenic coolant can be seen with dispersion of SiO_2 nanoparticles and lower specific heat of the nanocryogenic coolant can be seen with CuO nanoparticles.

3) Thermal Conductivity

Hamilton & Crosser Model is employed for calculating the effective thermal conductivity of nano cryogenic coolant with dispersion of TiO_2 nano particle for a temperature range of 55 K to 90 K as shown in Figure 5-26. From the figure, it can be observed that at a particular temperature, with 5 % volume dispersion of nanoparticles in cryogenic coolant the effective thermal conductivity is higher compared to cryogenic coolant. Further, at a particular volume concentration of nanoparticle dispersion in cryogenic coolant, with increase in temperature of cryogenic coolant the effective thermal conductivity decreases.

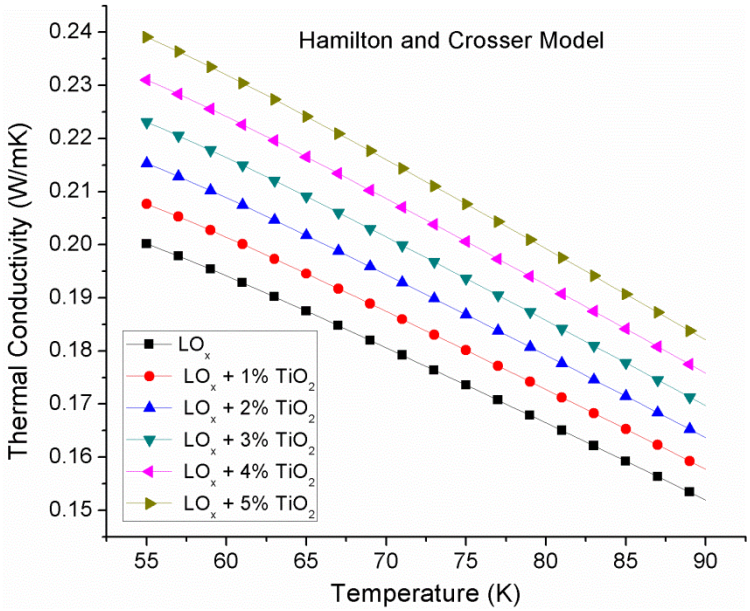

Figure 5-26: Variation of Thermal conductivity with respect to Temperature and volume concentration of TiO_2 for Hamilton and Crosser Model

Figure 5-27 shows the variation of effective thermal conductivity of different nano cryogenic coolant at different volume concentrations and cryogenic temperature of 73 K using Hamilton & Crosser Model. From the figure, it can be concluded that for a particular nano particle, increase in volume concentration increases the effective Thermal conductivity of nano cryogenic coolant. Further, at a particular volume concentration, SiO_2 based nano cryogenic coolant has lower effective thermal conductivity and SiC has higher effective thermal conductivity.

The comparison between cryogenic coolant and effective thermal conductivity of different models at volume concentration of 3 % for temperature range of 55 K to 90 K is shown in Figure 5-28. From the figure, it can be seen that at a particular temperature Hamilton and Crosser model shows higher effective thermal conductivity compared to other models and thermal conductivity of cryogenic coolant. Further, for a particular model at 3 % volume

concentration of nano cryogenic coolant, with increase in temperature the effective thermal conductivity decreases.

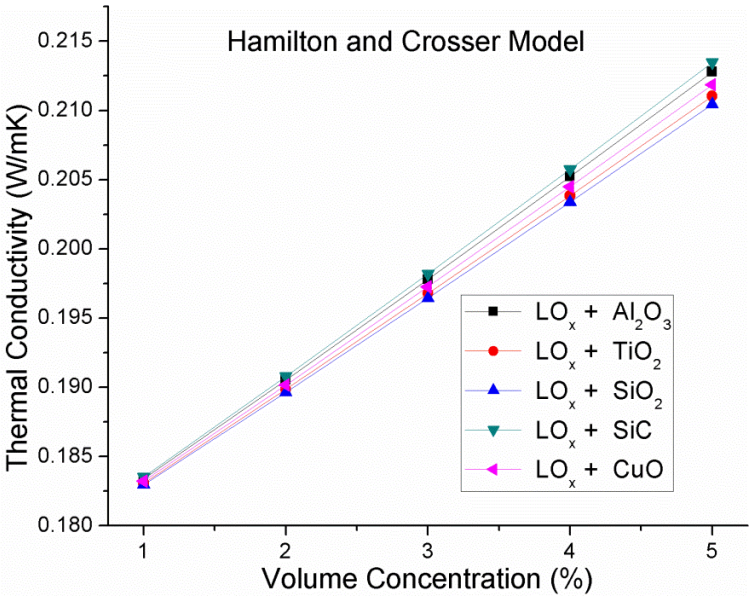

Figure 5-27: Variation of Thermal conductivity with respect to volume concentration and different nanoparticles of Liquid Oxygen at temperature of 73 K for Hamilton and Crosser Model

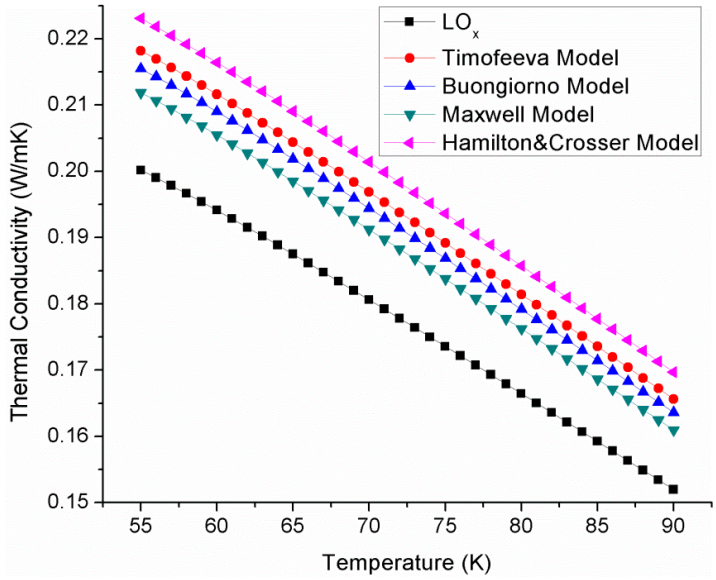

Figure 5-28: Variation of Thermal Conductivity with respect to to temperature at 3 % volume concentration for different models

Higher the effective thermal conductivity of nano cryogenic coolant higher will be the cooling capacity. Hence, dispersion of nano particles in cryogenic coolant (LO_X) increase the efficiency of the SMES by cooling the HTS tapes effectively without run-off at lower flow rates.

4) Viscosity

The effective viscosity of nano cryogenic coolant calculated by using Gherasim model for TiO_2 nano particle with volume concentration of 1-5% is shown in Figure 5-29. From the figure, it can be observed that effective viscosity reduces with the increase in temperature a particular volume concentration. Further, at a particular temperature effective viscosity of the nano cryogenic coolant is higher for 5% volume concentration compared to other concentration and cryogenic coolant.

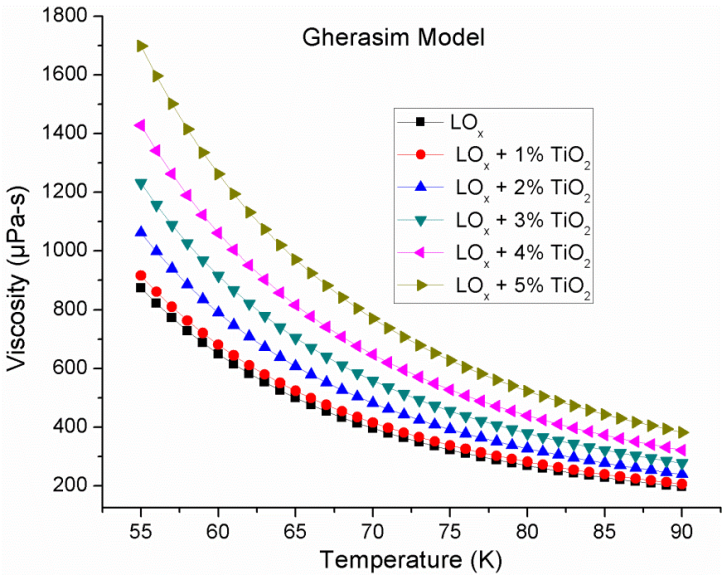

Figure 5-29: Viscosity as a function of Temperature with 1-5% volume concentration of nano particles

From Figure 5-30 shows the behavior of effective viscosity of nano cryogenic coolant for different models, the viscosity decreases non-linearly with increase in temperature from 55 K to 90 K. In this work it was found that the effective viscosity decreases with increase in temperature and volume fraction. Einstein model, Pak and Cho and Brickman models are having similar viscosity. Further, it can be seen that Gherasim model is having higher viscosity compared to other models and cryogenic coolant.

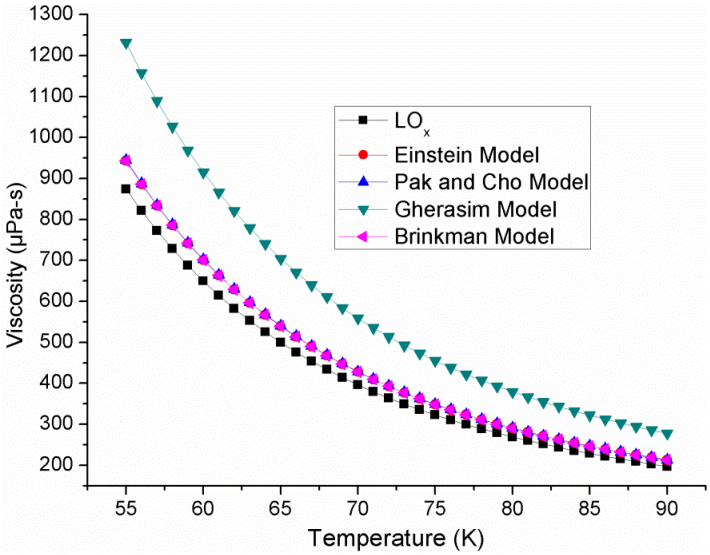

Figure 5-30: Variation of Viscosity with respect to Temperature with 3% volume concentration of nano particles

5.7.4.2 Thermophysical properties with variation in volume concentration of nano particle dispersion (CuO) in Liquid Oxygen (LOx) and Liquid Nitrogen (LN_2)

1) Density

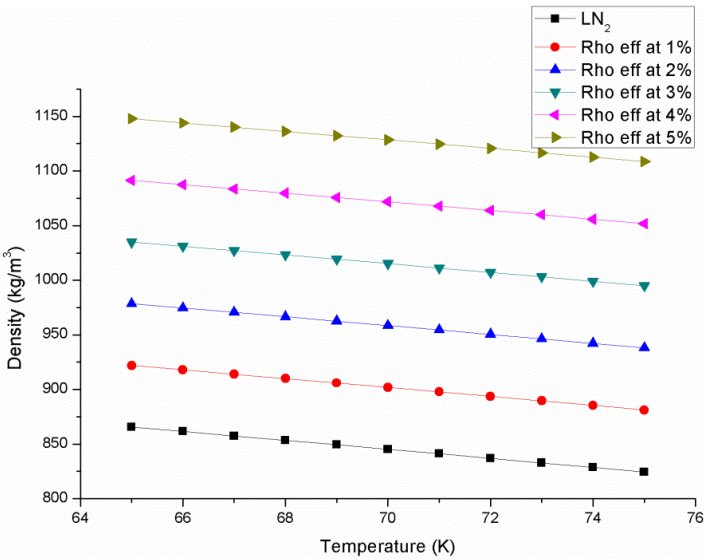

Figure 5-31: Variation of density with respect to temperature by varying concentration of nano particle

Figure 5-31 shows the variation of density with respect to temperature for varying volume concentration of CuO. It is observed that the density of the nano cryogenic coolant is increased with the dispersion of the nano particles. Moreover, with increase in temperature, density is decreasing gradually and the same trend is followed with different volume concentration.

2) Specific Heat

The specific heat for nano cryogenic coolant is calculated by using Pak and Cho model. Figure 5-32 shows the variation of specific heat with respect to temperature for varying volume concentration. Specific heat is decreasing with the increasing of nano particle dispersion. Furthermore, with the increase in the temperature specific heat is increasing gradually following the similar trend with increase in volume concentration.

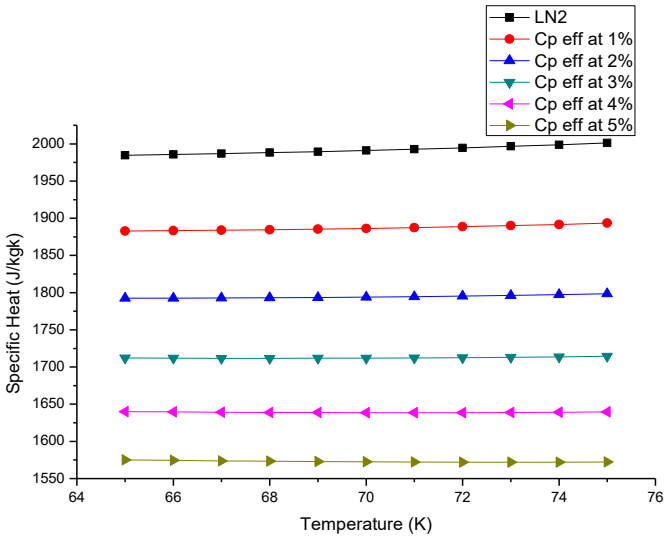

Figure 5-32: Variation of Specific heat with respect to temperature by varying concentration of nano particle

3) Thermal Conductivity

Figure 5-33(a) shows the variation of the thermal conductivity as a function of temperature at 3% volume concentration for different models. It is observed that, thermal conductivity will decrease with the increase in the temperature for all models. Further, Hamilton and Crosser model having higher and Buongiorno model having lower thermal conductivities compared to other models. Figure 5-33(b) shows that the variation of the thermal conductivity as a function of temperature at 70K for different models. From the figure it is observed that, thermal conductivity increases with increase in the volume concentration for all models. Further, Hamilton and Crosser having higher thermal conductivity with 6.66% of variation with Buongiorno and 1.18% with Maxwell model .

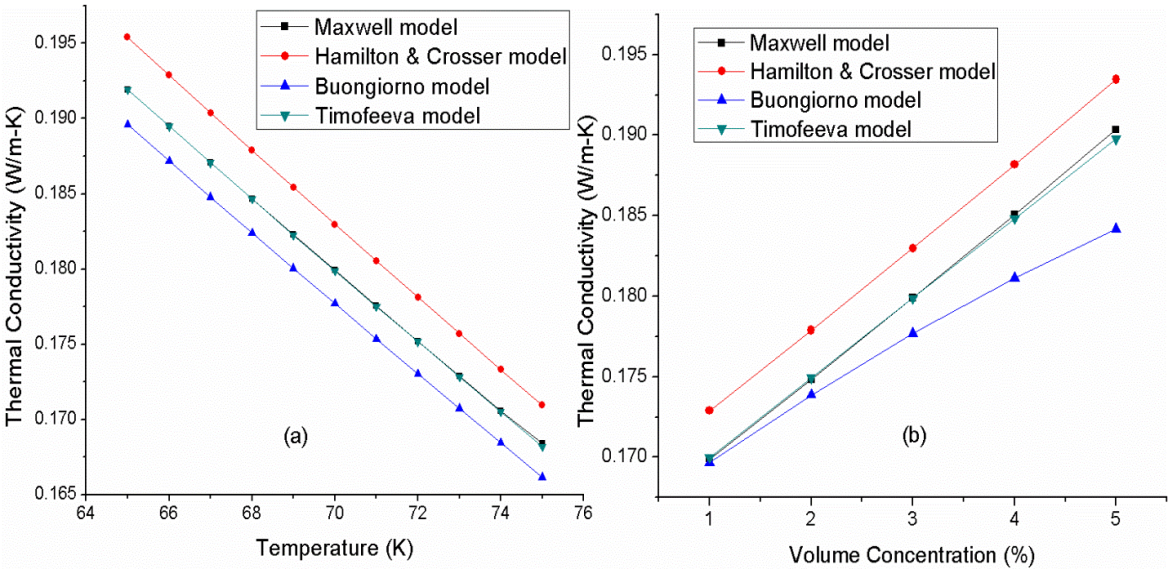

Figure 5-33: (a) Variation of Thermal conductivity with respect to temperature for different models at 3% volume concentration (b)Variation of Thermal conductivity with respect to volume concentration for different models at 70K

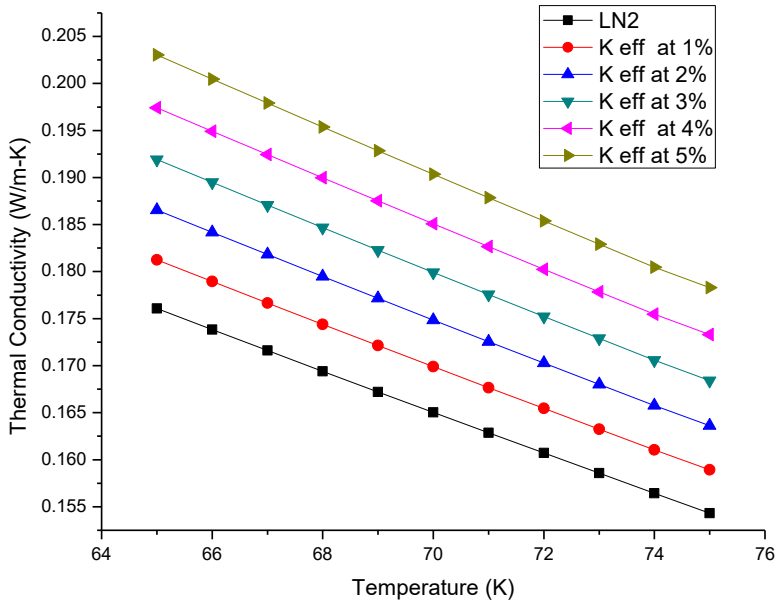

Figure 5-34: Variation of Thermal conductivity with respect to temperature for varying volume concentration

Thermal conductivity is an important parameter need to calculate because the heat transfer rate directly dependent on it. The cryogenic coolant having higher thermal conductivity is suitable for increasing the cooling rate. Figure 5-34 shows the variation of thermal conductivity as a function of temperature for varying volume concentration. It is observed that, thermal conductivity is increasing with the increase in volume concentration. Further, thermal conductivity is decreasing with the increase in temperature and follows the similar trend for varying volume concentration of nano particles. Hence, nano cryogenic coolant

with 5% of nano particle dispersion is better for cooling HTS SMES due to increased thermal conductivity.

4) Viscosity

The viscosity for nano cryogenic coolant is calculated by using different models. Figure 5-35 shows that variation of viscosity as a function of temperature for varying volume concentration. It is observed that, viscosity is increasing with the increasing in volume concentration. Further, viscosity is decreasing with increase in temperature and follows similar trend for increase in volume concentration.

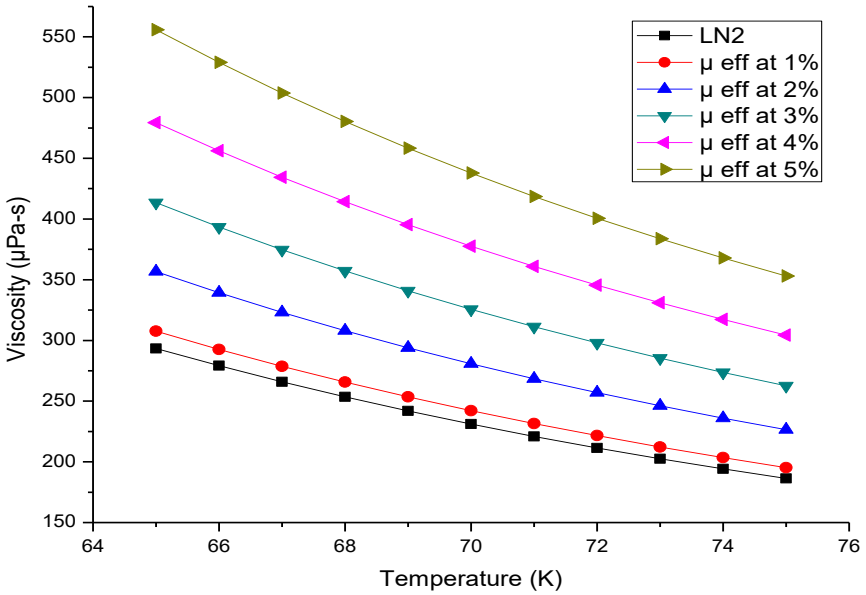

Figure 5-35: Variation of Viscosity with respect to temperature for varying volume concentration

Figure 5-36 (a) shows the variation of viscosity as a function of temperature at 3% volume concentration for different models. Einstein model is used for spherical type of nanoparticles with very less volume concentration. Pak and Cho and Brinkman models are having similar viscosity where as Gherasim and Wang models are having higher viscosity of 30% and 23% compared to the other models.

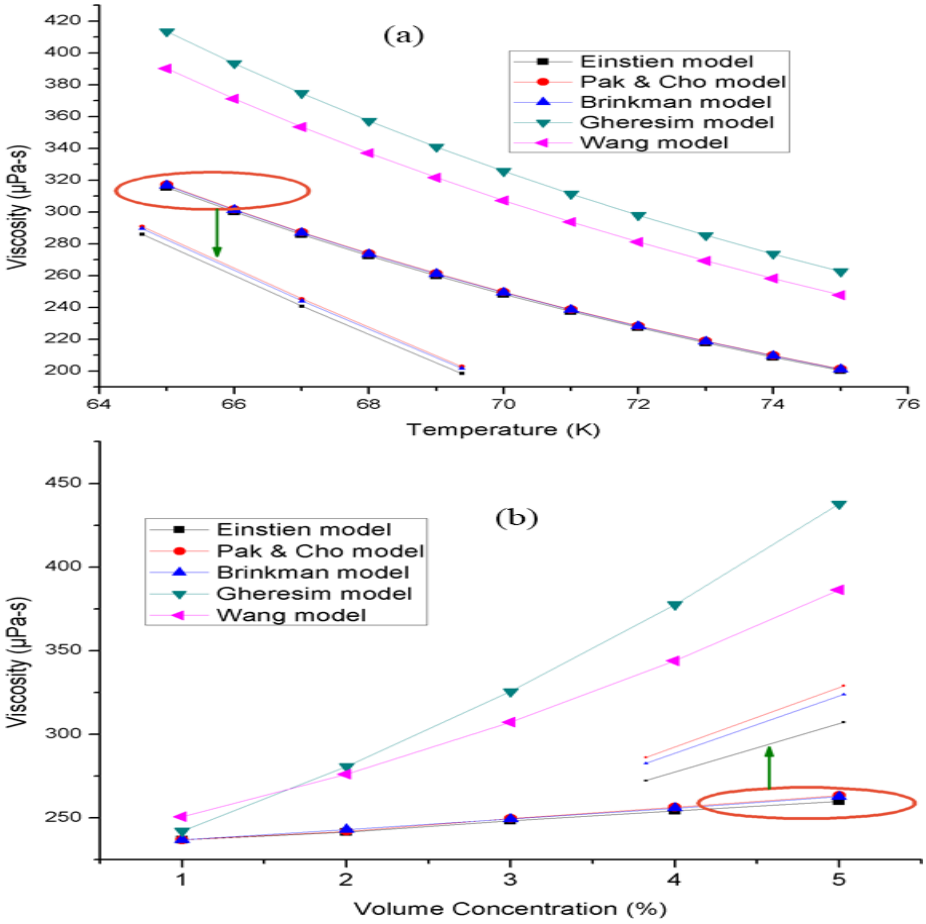

Figure 5-36: (a)Variation of Viscosity with respect to temperature for different models at 3% volume concentration (b)Variation of Viscosity with respect to volume concentration for different models at 70K

Figure 5-36 (b) shows the variation of Viscosity as a function of volume concentration at 70K temperature for different models. It is observed that Gheresim model is having higher viscosity followed by Wang model. Further, viscosity in other models is increasing slightly compared to Wang and Gheresim. From the figure, it shows the similar trend of increasing the viscosity of the liquid nitrogen with increase in nanoparticle dispersion.

5.8 Summary

A comprehensive thermohydraulic analysis is done to understand the feasibility of various coolants to be used in SMES including nanofluids. It is found that the heat transfer and cooling capacity is increased with the increase in the concentration of nanoparticles in the coolant. Further, feasibility of cooling of SMES using supercritical fluids is also investigated in the present work. It is observed that the pumping power is reduced with the use of supercritical fluid and heat transfer has been enhanced.

6 Conclusions and Future Scope

Superconducting magnetic energy storage (SMES) is one such system, which stores direct electrical energy with high specific power density, infinite discharge and charge cycles. Further, it discharges the electrical power within mill seconds with energy conversion efficiency of above 95%. The SMES utilizes three fundamental principles such as zero resistivity of the superconductor corresponds to zero resistive losses, diamagnetism corresponds to magnetic field repulsion and direct energy storage in a magnetic field. AC loss calculations and stability analysis are crucial in improving the efficiency of the SMES that encountered during the normal operation.

From the experimental investigation, mechanical characterization of different composite samples is predicted with and without cryogenic treatment for Superconducting Magnetic Energy Storage applications. Further, Thermohydraulic analysis was carried to investigate the pumping power required for circulating the SCN and the possible cooling capacity that can be achieved for cooling the HTS SMES. Furthermore, different nanoparticles such as Al_2O_3, TiO_2, SiO_2, SiC, and CuO are dispersed in the cryogenic coolant (LO_X) with different volume concentrations ranging from 1 % to 5 % at temperature ranging from 55 K to 90 K at 2 bar pressure. Results were calculated for effective density, thermal conductivity, viscosity and specific heat of nano cryogenic fluids. Later, the CuO nanoparticles dispersed in Liquid Nitrogen (LN_2) is studied to analyze the thermophysical properties of nanocryogenic coolant for SMES. From the analyses the following conclusions are drawn,

- ✓ When no external fields are present, the maximum *y*-component of magnetic flux density found to be 5 mT. However, with the increase in external magnetic field, the maximum is 11 mT.
- ✓ Time dependent AC losses are more predominantly affected by transport current densities than the applied magnetic fields.
- ✓ It can be concluded that the time dependent problems can be well dealt with Computational Electro Dynamics (CED) using FEM, even though the finite difference approach is pronounced.
- ✓ The composite samples when treated cryogenically show better strength against the brittle failure. It is observed that the Double Layer Carbon Fiber, the peak load

capacity for flexural testing various from 25.38 to 34.01kg for untreated and three hour treated fiber respectively.

- ✓ The cryogenically treated Double Layer Carbon Fiber has an increment of 34% in peak load capacity. The Hybrid Composite with Carbon Kevlar Fiber has a peak load capacity for flexural testing various from 24.14 to 25.67 kg for untreated and three hours treated. There is an increase about 6% in peak load capacity.
- ✓ The Single Layer Kevlar Fabric has peak load capacity for tensile testing various from 198 to 233.5 kg for untreated and immediate 1 hour treated fiber respectively. There is an increase about 18% in peak load capacity.
- ✓ However, in case of Double Layer Kevlar Fabric, the peak load capacity for tensile testing various from 297.9 to 337.5 kg/mm^2 for untreated and immediate 1 hour treated fiber respectively. There is an increase about 13% in peak load capacity.
- ✓ In case of Carbon Kevlar Fiber, the peak load capacity for tensile testing various from 300.3 to 353.7 kg/mm^2 for untreated and immediate 1 hour treated fiber respectively. There is an increase about 18% in peak load capacity.
- ✓ Hence it is concluded that composites treated with cryogenics shows the better mechanical properties compared with cryogenically untreated composites.
- ✓ Thus cryogenically treated Double Layer Carbon and Kevlar Composites are better for SMES applications due to higher Flexural and Tensile properties.
- ✓ SCN is having the lesser temperatures between the inlet and outlet of the corrugated pipe. Hence, it can be used as cryogenic coolant for long mandrel windings in the central channel cooling of HTS SMES.
- ✓ SCN has a highest specific heat compared with the LN2, greater cooling capacity and requires lesser pumping power.
- ✓ The hydraulic characteristics such as pumping power, friction factor are increases with the increase in the flow rate and heat loads at inlet temperature of 77 K.
- ✓ The thermal characteristics such as temperature difference, cooling capacity and Nusselt number are increases with the increase in the flow rate and heat loads at inlet temperature of 77 K.

- ✓ Liquid Nitrogen can be used as cryogenic coolant for cooling the HTS SMES because of better thermohydraulic characteristics.
- ✓ Density of nanocryogenic coolants increases with increase in volume concentration of nano particles and decreases with increase in temperature.
- ✓ Viscosity of nanocryogenic coolant increases with increase in volume concentration of nanoparticles and decreases with increase in temperature.
- ✓ The specific heat of nano cryogenic coolant increases with increase of temperature where as it decreases with increases in volume concentration which can enhance heat transfer rate.
- ✓ Thermal conductivity of nano-fluids increases with increase in volumetric concentration of nanoparticle and decreases with increase in temperature.
- ✓ Hence, by the dispersion of 5% of TiO_2 in LO_X can enhance the heat transfer rate due to better thermophysical properties.
- ✓ Density of nanocryogenic coolant is increased with the dispersion of the nano particles and decreasing with increase in temperature.
- ✓ Further, Specific heat is decreasing with increase in nano particle dispersion and increases with temperature.
- ✓ Thermal conductivity is decreasing with the increase in the temperature and increases with increase in the volume concentration for all models. Hamilton and Crosser model having higher and compared to other models.
- ✓ Viscosity is increasing with the increasing in volume concentration and decreasing with increase in temperature. Gherasim and Wang models are having higher viscosity of 30% and 23% compared to the other models.
- ✓ Hence, CuO with 5% dispersion in LN_2 is better compared to LN_2 in SMES application.

Future Scope

- ✓ The applicability of CED to irregular geometries of superconductors is still to be investigated. A comparison between the computational errors arising out of finite difference approach and FEM approach using CED is still sought.

- ✓ In future, the effect of corrugation pitch and depth on pressure drop and heat transfer, for different corrugation domains needs further to be studied for developing an efficient cooling system for HTS SMES.

- ✓ The transient analysis of HTS SMES in operation must be studied in detail for understanding the challenges in real time operation.

- ✓ Superconducting Magnetic Energy Storage (SMES) system attached to HTS power cables would impose fluctuation in current carrying capacity of HTS cables. Hence, the coolant which has to be circulated must be sufficient enough to take care of these fluctuations. Such studies help the users in designing reliable transmission systems

7 References

[1] P. Seidel, *Applied Superconducitivity, Handbook on Devices and Applications*. 2015.

[2] W. Yuan and M. Zhang, "Superconducting Magnetic Energy Storage (SMES) Systems," in *Handbook of Clean Energy Systems*, 2015, pp. 1–16.

[3] S. Nomura *et al.*, "Experimental results of a 7-T force-balanced helical coil for large-scale SMES," *IEEE Trans. Appl. Supercond.*, vol. 18, no. 2, pp. 701–704, 2008.

[4] T. Mito *et al.*, "Development of 1 MJ Conduction-Cooled LTS Pulse Coil for UPS-SMES," *IEEE Trans. Appl. Supercond.*, vol. 17, no. 2, pp. 1973–1976, 2007.

[5] H. Hayashi *et al.*, "Test results of power system control by experimental SMES," *IEEE Trans. Appl. Supercond.*, vol. 16, no. 2, pp. 598–601, 2006.

[6] S. Nagaya *et al.*, "Development and performance results of 5 MVA SMES for bridging instantaneous voltage dips," *IEEE Trans. Appl. Supercond.*, vol. 14, no. 2, pp. 699–704, 2004.

[7] S. Nagaya *et al.*, "Field test results of the 5 MVA SMES system for bridging instantaneous voltage dips," *IEEE Trans. Appl. Supercond.*, vol. 16, no. 2, pp. 632–635, 2006.

[8] A. Morandi *et al.*, "Design, manufacturing and preliminary tests of a conduction cooled 200 kJ Nb-Ti μSMES," *IEEE Trans. Appl. Supercond.*, vol. 18, no. 2, pp. 697–700, 2016.

[9] L. Ottonello *et al.*, "The largest Italian SMES," *IEEE Trans. Appl. Supercond.*, vol. 16, no. 2, pp. 602–607, 2006.

[10] X. Jiang, X. Zhu, Z. Cheng, X. Ren, and Y. He, "A 150 kVA/0.3 MJ SMES Voltage Sag Compensation System," *IEEE Trans. Appl. Supercond.*, vol. 15, no. 2, pp. 1903–1906, 2005.

[11] Q. Wang *et al.*, "Development of Large Scale Superconducting Magnet With Very Small Stray Magnetic Field for 2 MJ SMES," *IEEE Trans. Appl. Supercond.*, vol. 20, no. 3, pp. 1352–1355, 2010.

[12] X. Zhou, X. Y. Chen, and J. X. Jin, “Development of SMES technology and its applications in power grid,” *2011 Int. Conf. Appl. Supercond. Electromagn. Devices, ASEMD 2011*, pp. 260–269, 2011.

[13] J. D. Rogers *et al.*, “30-MJ superconducting magnetic energy storage system for electric utility transmission stabilization,” *IEEE Trans. Magn.*, vol. MAG-15, no. 1, pp. 820–823, 1979.

[14] C. A. Luongo, T. Baldwin, P. Ribeiro, S. Member, and C. M. Weber, “A 100 MJ SMES Demonstration at FSU-CAPS,” *IEEE Trans. Appl. Supercond.*, vol. 13, no. 2, pp. 1800–1805, 2003.

[15] H. J. Kim *et al.*, “3 MJ/750 kVA SMES System for Improving Power Quality,” *IEEE Trans. Appl. Supercond.*, vol. 16, no. 2, pp. 574–577, 2006.

[16] K. Shikimachi *et al.*, “Development of MVA Class HTS SMES System for Bridging Instantaneous Voltage Dips,” *IEEE Trans. Appl. Supercond.*, vol. 15, no. 2, pp. 1931–1934, 2005.

[17] P. Tixador *et al.*, “First Tests of a 800 kJ HTS SMES,” *IEEE Trans. Appl. Supercond.*, vol. 18, no. 2, pp. 774–778, 2008.

[18] K. Koyanagi *et al.*, “Design of a high energy-density SMES coil with Bi-2212 Cables,” *IEEE Trans. Appl. Supercond.*, vol. 16, no. 2, pp. 586–589, 2006.

[19] Q. Wang, S. Song, Y. Lei, and Y. Dai, “Design and fabrication of a conduction-cooled high temperature superconducting magnet for 10 kJ superconducting magnetic energy storage system,” *IEEE Trans. Appiled Supercond.*, vol. 16, no. 2, pp. 570–573, 2006.

[20] Q. Wang *et al.*, “A 30 kJ Bi2223 high temperature superconducting magnet for SMES with solid-nitrogen protection,” *IEEE Trans. Appl. Supercond.*, vol. 18, no. 2, pp. 754–757, 2008.

[21] J. Shi *et al.*, “Development of a conduction-cooled HTS SMES,” *IEEE Trans. Appl. Supercond.*, vol. 17, no. 3, pp. 3846–3851, 2007.

[22] S. Dai *et al.*, “Design of a 1 MJ/0.5 MVA HTS Magnet for SMES,” *IEEE Trans. Appl. Supercond.*, vol. 17, no. 2, pp. 1977–1980, 2007.

[23] W. S. Kim *et al.*, “Design of HTS magnets for a 600 kJ SMES,” *IEEE Trans. Appl. Supercond.*, vol. 16, no. 2, pp. 620–623, 2006.

[24] H. K. Yeom *et al.*, “An Experimental Study of the Conduction Cooling System for the 600 kJ HTS SMES,” *IEEE Trans. Appiled Supercond.*, vol. 18, no. 2, pp. 741–744, 2008.

[25] J. H. Choi, H. G. Cheon, J. W. Choi, H. J. Kim, K. C. Seong, and S. H. Kim, “A study on insulation characteristics according to cooling methods of the HTS SMES,” *Phys. C Supercond. its Appl.*, vol. 470, no. 3, pp. 1703–1706, 2010.

[26] R. Kreutz *et al.*, “Design of a 150 kJ High- T c SMES (HSMES) for a 20 kVA Uninterruptible Power Supply System,” *IEEE Trans. Appl. Supercond.*, vol. 13, no. 2, pp. 1860–1862, 2003.

[27] J. Kozak, S. Kozak, T. Janowski, and M. Majka, “Design and performance results of first polish SMES,” *IEEE Trans. Appl. Supercond.*, vol. 19, no. 3, pp. 1981–1984, 2009.

[28] J. Kozak, M. Majka, S. Kozak, and T. Janowski, “Performance of SMES system with HTS magnet,” *IEEE Trans. Appl. Supercond.*, vol. 20, no. 3, pp. 1348–1351, 2010.

[29] C. J. Hawley and S. A. Gower, “Design and preliminary results of a prototype HTS SMES device,” *IEEE Trans. Appl. Supercond.*, vol. 15, no. 2 PART II, pp. 1899–1902, 2005.

[30] H. Ueda, A. Ishiyama, K. Shikimachi, N. Hirano, and S. Nagaya, “Stability and protection of coils wound with YBCO bundle conductor,” *IEEE Trans. Appl. Supercond.*, vol. 20, no. 3, pp. 1320–1323, 2010.

[31] V. S. Vulusala G and S. Madichetty, “Application of superconducting magnetic energy storage in electrical power and energy systems: a review,” *Int. J. ENERGY Res.*, vol. 42, no. 2, pp. 358–368, 2017.

[32] Y. Horiuchi, Y. Yamasaki, T. Ezaki, and T. Imayoshi, “Solenoid type shielding coil systems for a small scale SMES,” *IEEE Trans. Appl. Supercond.*, vol. 18, no. 2, pp. 709–712, 2008.

[33] T. Ezaki, Y. Horiuchi, T. Hatanaka, M. Joko, S. Setoguchi, and H. Hayashi,

"Toroidal-type shielding coil systems for the power system control SMES," *IEEE Trans. Appl. Supercond.*, vol. 14, no. 2, pp. 746–749, 2004.

[34] B. Vincent, P. Tixador, T. Lecrevisse, J. M. Rey, X. Chaud, and Y. Miyoshi, "HTS magnets: Opportunities and issues for SMES," *IEEE Trans. Appl. Supercond.*, vol. 23, no. 3, p. 5700805, 2013.

[35] 0. Vincent-Viry, A. Mailfert, and D. Trassart, "New SMES Coil Configurations," *IEEE Trans. Appiled Supercond.*, vol. 11, no. I, pp. 1916–1919, 2001.

[36] D. Lieurance, F. Kimball, C. Rix, and C. Luongo, "Design and Cost Studies for Small Scale Superconducting Magnetic Energy Storage (SMES) Systems," *IEEE Trans. Appl. Supercond.*, vol. 5, no. 2, pp. 350–353, 1995.

[37] Y. Oga, S. Noguchi, and M. Tsuda, "Comparison of optimal configuration of SMES magnet wound with MgB 2 and YBCO conductors," *IEEE Trans. Appl. Supercond.*, vol. 23, no. 3, pp. 0–3, 2013.

[38] T. Shintomi, "APPLICATIONS OF HIGH-Tc SUPERCONDUCTORS TO SUPERCONDUCTING MAGNETIC ENERGY STORAGE (SMES)," in *HighTemperature Superconductivity 2*, 2004, pp. 213–222.

[39] K. C. Seong, H. J. Kim, S. H. Kim, S. J. Park, M. H. Woo, and S. Y. Hahn, "Research of a 600 kJ HTS-SMES system," *Phys. C*, vol. 465, pp. 1240–1246, 2007.

[40] a.-R. Kim *et al.*, "Operational Characteristic of the High Quality Power Conditioner With SMES," *Appl. Supercond. IEEE Trans.*, vol. 18, no. 2, pp. 705–708, 2008.

[41] S. Kim, K. Sim, H. Kim, J. Bae, E. Lee, and K. Seong, "Thermal characteristics of conduction cooled 600 kJ HTS SMES system," *Cryogenics (Guildf).*, vol. 49, no. 6, pp. 294–298, 2009.

[42] A. Kim *et al.*, "Operating Characteristic Analysis of HTS SMES for Frequency Stabilization of Dispersed Power Generation System," vol. 20, no. 3, pp. 1334–1338, 2010.

[43] W. Yao, L. Jiang, J. Fang, J. Wen, S. Cheng, and Q. H. Wu, "Adaptive power oscillation damping controller of superconducting magnetic energy storage device for interarea oscillations in power system," *Int. J. Electr. Power Energy Syst.*, vol.

78, pp. 555–562, Jun. 2016.

[44] Y. Saichi, D. Miyagi, and M. Tsuda, “A Suitable Design Method of SMES Coil for Reducing Superconducting Wire Usage Considering Maximum Magnetic Flux Density,” *IEEE Trans. Appl. Supercond.*, vol. 24, no. 3, pp. 1–5, 2014.

[45] S. Lee *et al.*, “Design of HTS Toroidal Magnets for a 5 MJ SMES,” *IEEE Trans. Appl. Supercond.*, vol. 22, no. 3, pp. 5700904–5700904, 2012.

[46] M. Park *et al.*, “Conceptual Design of HTS Magnet for a 5 MJ Class SMES,” vol. 18, no. 2, pp. 750–753, 2008.

[47] W. Kim, S. Kwak, J. Lee, K. Choi, H. Jung, and K. Seong, “Design of HTS Magnets for a 600 kJ SMES,” vol. 16, no. 2, pp. 620–623, 2006.

[48] S. Noguchi, a Ishiyama, S. Akita, H. Kasahara, Y. Tatsuta, and S. Kouso, “An optimal configuration design method for HTS-SMES coils,” *Ieee_J_Asc*, vol. 15, no. 2, pp. 1927–1930, 2005.

[49] H. Hayashi, K. Tsutsumi, K. Funaki, M. Iwakuma, and K. Tasaki, “Design study of a 1 GJ class HTS-SMES (1) Conceptual design of a magnet system,” vol. 360, pp. 1327–1331, 2001.

[50] K. Tasaki *et al.*, “Design study of a 3.6 MJ HTS-SMES: Compact magnet design,” *Phys. C Supercond. its Appl.*, vol. 357–360, pp. 1332–1335, 2001.

[51] K. Venkataratnam, V. V. Rao, K. N. V. S. Rao, and A. A. Kumar, “Optimum design of superconducting magnet coil for a micro SMES unit,” *IEEE Trans. Appl. Supercond.*, vol. 9, no. 2 PART 1, pp. 350–353, 1999.

[52] M. Qiu, S. Rao, J. Zhu, S. Fu, and Z. Li, “Energy Storage Characteristics of MJ-Class Toroidal HTS- SMES Considering Maximum Value of Perpendicular Magnetic Field,” *Energy Procedia*, vol. 105, pp. 4179–4184, 2017.

[53] J. Zhu, H. Zhang, W. Yuan, M. Zhang, and X. Lai, “Design and cost estimation of superconducting magnetic energy storage (SMES) systems for power grids,” 2013.

[54] S. Kwak *et al.*, “The Optimal Design of 600 kJ SMES Magnet Based on Stress and Magnetic Field Analysis,” vol. 18, no. 2, pp. 713–716, 2008.

[55] Y. Xu *et al.*, “A Study on the Design and Comparison of 1 - 100 MJ Class SMES

Magnet with Different Coil Configurations," vol. 8223, no. c, 2017.

[56] J. H. Bae, S. H. Kim, H. J. Kim, M. H. Sohn, K. C. Seong, and H. M. Kim, "Design , fabrication and evaluation of a conduction cooled HTS magnet for SMES," *Phys. C Supercond. its Appl.*, vol. 469, no. 15–20, pp. 1794–1798, 2009.

[57] X. Chen and J. Jin, "Design and Optimization of HTS Magnets for SMES Applications," pp. 26–29, 2009.

[58] S. Kwak *et al.*, "Design of HTS Magnets for a 2 . 5 MJ SMES," vol. 19, no. 3, pp. 1985–1988, 2009.

[59] E. S. Otabe, M. Kiuchi, T. Matsushita, K. Fujino, K. Ohmatsu, and B. Ni, "Fabrication of a working Bi-2223 superconducting magnet cooled by liquid nitrogen," *Cryogenics (Guildf).*, vol. 49, no. 6, pp. 267–270, 2009.

[60] J. Zhao, Y. Li, and Y. Gao, "3D simulation of AC loss in a twisted multi-filamentary superconducting wire," *Cryogenics (Guildf).*, vol. 84, pp. 60–68, 2017.

[61] M. Erdogan, "Calculation of AC loss in two-layer superconducting cable with equal currents in the layers," *Phys. C Supercond. its Appl.*, vol. 531, pp. 20–24, 2016.

[62] Y. D. Agassi, "AC losses in superconductors with a power-law constitutive relation," *Phys. C Supercond. its Appl.*, vol. 517, pp. 41–48, 2015.

[63] Y. Xu *et al.*, "Distribution of AC loss in a HTS magnet for SMES with different operating conditions," vol. 494, pp. 213–216, 2013.

[64] E. S. Otabe, S. Komatsu, V. S. Vyatkin, M. Kiuchi, T. Kawahara, and S. Yamaguchi, "Numerical estimation of AC loss in superconductors with ripple current," *Phys. C Supercond. its Appl.*, vol. 494, pp. 173–176, 2013.

[65] N. Amemiya *et al.*, "Ac loss analyses of superconducting power transmission cables considering their three-dimensional geometries," *Phys. C Supercond. its Appl.*, vol. 484, pp. 148–152, 2013.

[66] Y. Zhao, J. Fang, W. Zhang, J. Zhao, and L. Sheng, "Comparison between measured and numerically calculated AC losses in second-generation high temperature superconductor pancake coils," *Phys. C Supercond. its Appl.*, vol. 471, no. 21–22, pp. 1003–1006, 2011.

[67] Z. Hong and T. A. Coombs, “Numerical Modelling of AC Loss in Coated Conductors by Finite Element Software Using H Formulation,” *J Supercond NovMagn*, vol. 23, pp. 1551–1562, 2010.

[68] K. Kajikawa, K. Funaki, K. Shikimachi, N. Hirano, and S. Nagaya, “Numerical and theoretical evaluations of AC losses for single and infinite numbers of superconductor strips with direct and alternating transport currents in external AC magnetic field,” *Phys. C Supercond. its Appl.*, vol. 470, no. 20, pp. 1321–1324, 2010.

[69] M. Park *et al.*, “Analysis of Eddy Current Loss in Conducting Cooling Plate for 600 kJ SMES,” pp. 1744–1747, 2007.

[70] S. S. Yammanur, K. M. Shaik, R. K. Gadekula, A. Kumar, and R. S. Dondapati, “Feasibility study on dispersion of nano particles in liquid oxygen (LOX) as nano cryogenic coolant to be used in superconducting magnetic energy storage (SMES),” *Int. J. Mech. Eng. Technol.*, vol. 8, no. 7, pp. 1573–1582, 2017.

[71] R. K. Gadekula, V. R. Uppada, A. Kumar, and R. S. Dondapati, “Feasibility study on nano cryogenic coolant to be used in futuristic high temperature superconducting (HTS) cables,” *Int. J. Mech. Eng. Technol.*, vol. 8, no. 7, pp. 1590–1598, 2017.

[72] P. Anand, R. K. Gadekula, U. V. Ramana, and R. S. Dondapati, “Effect of Diameter of Nanoparticles on the thermophysical properties of LN2 based Cryocoolants,” *Mater. Today Proc.*, vol. 5, no. 14, pp. 28279–28287, 2018.

[73] R. Tadepalli *et al.*, “Characterization of Thermophysical properties of Al2O3, TiO2, SiO2, SiC and CuO Nano Particles at Cryogenic Temperatures,” *Mater. Today Proc.*, vol. 5, no. 14, pp. 28454–28461, 2018.

[74] A. Taflove and S. C. Hagness, “Computational Electrodynamics: The Finite-difference Time-domain Method,” 2005.

[75] A. M. Campbell, “An Introduction to Numerical Methods in Superconductors,” *J Supercond NovMagn*, vol. 24, pp. 27–33, 2011.

[76] Z. Hong, L. Ye, M. Majoros, A. M. Campbell, and T. A. Coombs, “Numerical Estimation of AC Loss in MgB2 Wires in Self-field Condition,” *J. Supercond. Nov. Magn.*, vol. 21, no. 3, pp. 205–211, 2008.

[77] S. Kim, K. Sim, J. Cho, H. M. Jang, and M. Park, “AC loss analysis of HTS power cable with RABiTS coated conductor,” *IEEE Trans. Appl. Supercond.*, vol. 20, no. 3, pp. 2130–2133, 2010.

[78] G. Wang, K. Gu, Z. Huang, and P. Ding, “Improving the wear resistance of as-sprayed WC coating by deep cryogenic treatment,” *Mater. Lett.*, vol. 185, pp. 363–365, Dec. 2016.

[79] A. Idayan, A. Gnanavelbabu, and K. Rajkumar, “Influence of Deep Cryogenic Treatment on the Mechanical Properties of AISI 440C Bearing Steel,” *Procedia Eng.*, vol. 97, pp. 1683–1691, 2014.

[80] A. Akhbarizadeh, A. Shafyei, and M. A. Golozar, “Effects of cryogenic treatment on wear behavior of D6 tool steel,” *Mater. Des.*, vol. 30, no. 8, pp. 3259–3264, 2009.

[81] Y. Zhang *et al.*, “Modification of tensile, wear and interfacial properties of Kevlar fibers under cryogenic treatment,” *Compos. Part B Eng.*, vol. 99, pp. 358–365, Aug. 2016.

[82] A. Bensely *et al.*, “Fatigue behaviour and fracture mechanism of cryogenically treated En 353 steel,” *Mater. Des.*, vol. 30, no. 8, pp. 2955–2962, Sep. 2009.

[83] F. Xu *et al.*, “Modification of tensile, wear and interfacial properties of Kevlar fibers under cryogenic treatment,” *Compos. Part B Eng.*, vol. 116, pp. 398–405, May 2017.

[84] Y. Shao *et al.*, “Influence of cryogenic treatment on mechanical and interfacial properties of carbon nanotube fiber/bisphenol-F epoxy composite,” *Compos. Part B Eng.*, vol. 125, pp. 195–202, Sep. 2017.

[85] M. Araghchi, H. Mansouri, R. Vafaei, and Y. Guo, “A novel cryogenic treatment for reduction of residual stresses in 2024 aluminum alloy,” *Mater. Sci. Eng. A*, vol. 689, pp. 48–52, Mar. 2017.

[86] B. Podgornik, I. Paulin, B. Zajec, S. Jacobson, and V. Leskovšek, “Deep cryogenic treatment of tool steels,” *J. Mater. Process. Technol.*, vol. 229, pp. 398–406, 2016.

[87] G. Jia, C. Liubiao, G. Kaixuan, and W. Junjie, “A Cryogenic Treatment System for Treating Large Rolls,” *Phys. Procedia*, vol. 67, pp. 367–372, 2015.

[88] R. Ou, H. Zhao, S. Sui, Y. Song, and Q. Wang, “Reinforcing effects of Kevlar fiber on the mechanical properties of wood-flour/high-density-polyethylene composites,” *Compos. Part A Appl. Sci. Manuf.*, vol. 41, no. 9, pp. 1272–1278, 2010.

[89] F. J. da Silva, S. D. Franco, Á. R. Machado, E. O. Ezugwu, and A. M. Souza, “Performance of cryogenically treated HSS tools,” *Wear*, vol. 261, no. 5–6, pp. 674–685, 2006.

[90] H. Ghasemi Nanesa and M. Jahazi, “Alternative phase transformation path in cryogenically treated AISI D2 tool steel,” *Mater. Sci. Eng. A*, vol. 634, pp. 32–36, May 2015.

[91] S. Harish, A. Bensely, D. Mohan Lal, A. Rajadurai, and G. B. Lenkey, “Microstructural study of cryogenically treated En 31 bearing steel,” *J. Mater. Process. Technol.*, vol. 209, no. 7, pp. 3351–3357, 2009.

[92] S. Zhirafar, A. Rezaeian, and M. Pugh, “Effect of cryogenic treatment on the mechanical properties of 4340 steel,” *J. Mater. Process. Technol.*, vol. 186, no. 1–3, pp. 298–303, May 2007.

[93] N. B. Dhokey, J. Dandawate, H. Gangurde, and A. Harle, “Metallurgical investigation of cryogenically cracked M35 tool steel,” *Eng. Fail. Anal.*, vol. 21, pp. 52–58, 2012.

[94] H. CHI, D. MA, Q. YONG, L. WU, Z. ZHANG, and Y. WANG, “Effect of Cryogenic Treatment on Properties of Cr8-Type Cold Work Die Steel,” *J. Iron Steel Res. Int.*, vol. 17, no. 6, pp. 43–59, Jun. 2010.

[95] M. Koneshlou, K. Meshinchi Asl, and F. Khomamizadeh, “Effect of cryogenic treatment on microstructure, mechanical and wear behaviors of AISI H13 hot work tool steel,” *Cryogenics (Guildf).*, vol. 51, no. 1, pp. 55–61, Jan. 2011.

[96] J. Hemanth, “Tribological behavior of cryogenically treated B4Cp/Al–12% Si composites,” *Wear*, vol. 258, no. 11–12, pp. 1732–1744, Jun. 2005.

[97] C. XIE, J. HUANG, Y. TANG, and L. GU, “Effects of deep cryogenic treatment on microstructure and properties of WC–11Co cemented carbides with various carbon contents,” *Trans. Nonferrous Met. Soc. China*, vol. 25, no. 9, pp. 3023–3028, Sep. 2015.

[98] M. Lebioda, J. Rymaszewski, and E. Korzeniewska, “Simulation of thermal processes in superconducting pancake coils cooled by GM cryocooler,” *J. Phys. Conf. Ser.*, vol. 494, no. 1, 2014.

[99] E. W. Lemmon, M. L. Huber, and M. O. Mclinden, “NIST Reference Fluid Thermodynamic and Transport Properties,” *version7.0, beta, USA, p30*, 2010.

[100] E. W. Lemmon, M. L. Huber, and M. O. Mclinden, *NIST Reference Fluid Thermodynamic and Transport Properties — REFPROP*. 2013.

[101] R. S. Dondapati and V. V Rao, “Pressure Drop and Heat Transfer Analysis of Long Length Internally Cooled HTS Cables,” *IEEE Trans. Appl. Supercond.*, vol. 23, no. 3, pp. 2–5, 2013.

[102] A. Einstein, “EINE NEUE BESTIMMUNG DER MOLEKüLDIMENSIONEN,” *Ann. Phys.*, vol. 324.2, pp. 289–306, 1905.

[103] R. S. Dondapati and V. V. Rao, “Entropy generation minimization (EGM) to optimize mass flow rate in dual channel cable-in-conduit conductors (CICCs) used for fusion grade magnets,” *Fusion Eng. Des.*, vol. 89, no. 6, pp. 837–846, Jun. 2014.

[104] R. K. Gadekula and R. S. Dondapati, “Entropy Generation Minimization (EGM) in High Temperature Superconducting (HTS) cables for Optimization of Thermohydraulic Performance,” *Phys. C Supercond. its Appl.*, vol. 566, p. 1353541, 2019.

[105] R. S. Dondapati and V. V Rao, “Parametric studies on entropy generation rate in dual channel cable-in-conduit conductors (CICCs) with supercritical helium (SHe) using computational fluid dynamics,” *Fusion Eng. Des.*, vol. 142, pp. 63–69, 2019.

[106] *ANSYS-Fluent Theory Guide*. Canonsburg, PA: Ansys Inc, 2013.

[107] H. K. Versteeg and W. Malalasekera, *An Introduction to Computational Fluid Dynamics*, 2nd ed. Pearson Education, 2007.

[108] M. J. S. De Lemos and R. A. Silva, “Turbulent flow over a layer of a highly permeable medium simulated with a diffusion-jump model for the interface,” *Int. J. Heat Mass Transf.*, vol. 49, no. 3–4, pp. 546–556, 2006.

[109] R. S. Dondapati and V. V Rao, “Pressure Drop and Heat Transfer Analysis of Long

Length Internally Cooled HTS Cables," *IEEE Trans. Appl. Supercond.*, vol. 23, no. 3, pp. 1–5, 2013.

[110] Y. Ivanov, H. Watanabe, M. Hamabe, T. Kawahara, J. Sun, and S. Yamaguchi, "Design Study of LN2 Circulation in a Long SC Power Transmission Lines," *Phys. Procedia*, vol. 36, pp. 1372–1377, 2012.

PUBLICATIONS FROM PRESENT WORK

S.No	AUTHORS	TITLE /CHAPTER	JOURNAL /BOOK /CONFERENCE	VOLUME /EDITION	YEAR
1	Gaurav Vyas, Raja Sekhar Dondapati	AC losses in the development of superconducting magnetic energy storage devices	JOURNAL OF ENERGY STORAGE	27	2019
2	Gaurav Vyas, Raja Sekhar Dondapati	Investigation on the structural behavior of superconducting magnetic energy storage (SMES) devices	JOURNAL OF ENERGY STORAGE	28	2020
3	Gaurav Vyas, Raja Sekhar Dondapati	Superconducting Magnetic Energy Storage (SMES)	HIGH TEMPERATURE SUPERCONDUCTING DEVICES FOR ENERGY APPLICATIONS	1st	2020
4	Gaurav Vyas, Raja Sekhar Dondapati	Feasibility of Super Critical Hydrogen for cooling Superconducting Magnetic Energy Storage (SMES) Devices	SASM-2021 (IEEE XPLORE CONFERENCE PROCEEDINGS)	Accepted	2021
5	Gaurav Vyas, Raja Sekhar Dondapati	A Critical Review on AC Losses in HTS tapes used for Superconducting Magnetic Energy Storage (SMES) Devices	CIMS 2021 (IEEE XPLORE CONFERENCE PROCEEDINGS)	Accepted	2021